⑫

DNA-TR-87-1

NUMERICAL SIMULATION OF NEAR-SURFACE ENVIRONMENTS AND PARTICULATE CLOUDS GENERATED BY LARGE-AREA FIRES

S. Marcus.
S. Krueger
M. Rosenblatt
California Research and Technology, Inc.
20943 Devonshire Street
Chatsworth, CA 91311-2377

DTIC
ELECTE
DEC 0 4 1987
S   D
D

24 August 1987

Technical Report

AD-A188 375

Prepared for
    Director
    Defense Nuclear Agency
    Washington, DC 20305-1000

87 1 1

DISTRIBUTION LIST UPDATE

This mailer is provided to enable DNA to maintain current distribution lists for reports. We would appreciate your providing the requested information.

☐   Add the individual listed to your distribution list.

☐   Delete the cited organization/individual.

☐   Change of address.

NAME: _____

ORGANIZATION: _____

OLD ADDRESS	**CURRENT ADDRESS**
_____	_____
_____	_____
_____	_____

TELEPHONE NUMBER: (____) _____

SUBJECT AREA(s) OF INTEREST:

_____	_____
_____	_____
_____	_____

DNA OR OTHER GOVERNMENT CONTRACT NUMBER: _____

CERTIFICATION OF NEED-TO-KNOW BY GOVERNMENT SPONSOR (if other than DNA):

SPONSORING ORGANIZATION: _____

CONTRACTING OFFICER OR REPRESENTATIVE: _____

SIGNATURE: _____

Director
Defense Nuclear Agency
ATTN: ███ TITL
Washington, DC 20305-1000

AD-A188 375

REPORT DOCUMENTATION PAGE

1a. REPORT SECURITY CLASSIFICATION UNCLASSIFIED		1b. RESTRICTIVE MARKINGS			
2a. SECURITY CLASSIFICATION AUTHORITY N/A since Unclassified		3. DISTRIBUTION/AVAILABILITY OF REPORT Approved for public release; distribution is unlimited.			
2b. DECLASSIFICATION/DOWNGRADING SCHEDULE N/A since Unclassified					
4. PERFORMING ORGANIZATION REPORT NUMBER(S) CRT 3880F		5. MONITORING ORGANIZATION REPORT NUMBER(S) DNA-TR-87-1			
6a. NAME OF PERFORMING ORGANIZATION California Research and Technology, Inc.	6b. OFFICE SYMBOL (If applicable)	7a. NAME OF MONITORING ORGANIZATION Director Defense Nuclear Agency			
6c. ADDRESS (City, State, and ZIP Code) 20943 Devonshire Street Chatsworth, California 91311-2377		7b. ADDRESS (City, State, and ZIP Code) Washington, DC 20305-1000			
8a. NAME OF FUNDING/SPONSORING ORGANIZATION	8b. OFFICE SYMBOL (If applicable) SPTD/Flohr	9. PROCUREMENT INSTRUMENT IDENTIFICATION NUMBER DNA 001-83-C-0017 DNA 001-85-C-0193			
8c. ADDRESS (City, State, and ZIP Code)		10. SOURCE OF FUNDING NUMBERS			

PROGRAM ELEMENT NO. 62715H 62715H	PROJECT NO. RG G54CMXG	TASK NO. RR R	WORK UNIT ACCESSION NO. DH008821

11. TITLE (Include Security Classification)
NUMERICAL SIMULATION OF NEAR-SURFACE ENVIRONMENTS AND PARTICULATE CLOUDS GENERATED BY LARGE-AREA FIRES

12. PERSONAL AUTHOR(S) Marcus, S.L.; Krueger, S.K.; Rosenblatt, M.			
13a. TYPE OF REPORT Technical	13b. TIME COVERED FROM 821103 TO 861222	14. DATE OF REPORT (Year, Month, Day) 870824	15. PAGE COUNT 122

16. SUPPLEMENTARY NOTATION
This work was sponsored by the Defense Nuclear Agency under RDT&E RMC Code B3450834662 RG RR 00009 25904D and RDT&E RMSS Code B345084466 G54CMXGR00004 H2590D.

17.	COSATI CODES		18. SUBJECT TERMS (Continue on reverse if necessary and identify by block number)		
FIELD	GROUP	SUB-GROUP	Firestorm	DICE	Meteotron Swirl
18	3		Large Area Fires	Nuclear Fires	Turbulence
13	12		Fire Winds	Soot Clouds	Plumes

19. ABSTRACT (Continue on reverse if necessary and identify by block number)

The near-surface environments and lofted particulate clouds produced by large-area fires have been simulated with the axisymmetric DICE code. Studies with an inviscid version of the model showed that variations in the assumed area and burning rate of the fire have a strong effect on the maximum inflow winds, temperatures, and plume heights which develop. Using a multiphase version of the model, which predicts concentrations of soot, water vapor, liquid water, and ice, it was found that the particulate clouds generated by large-area fires show considerable vertical dispersion, and that latent heat released by condensing water vapor can significantly enhance cloud heights.

When the grid is changed from finely-zoned to coarsely-zoned, the effective "mixing" of the combustion heating over a greater depth generates cooler maximum temperatures, causing the plume to shift from oscillatory (overshooting) behavior to

20. DISTRIBUTION/AVAILABILITY OF ABSTRACT ☐ UNCLASSIFIED/UNLIMITED ☒ SAME AS RPT ☐ DTIC USERS	21. ABSTRACT SECURITY CLASSIFICATION UNCLASSIFIED	
22a. NAME OF RESPONSIBLE INDIVIDUAL Sandra E. Young	22b. TELEPHONE (Include Area Code) (202) 325-7042	22c. OFFICE SYMBOL DNA/CSTI

DD FORM 1473, 84 MAR   83 APR edition may be used until exhausted.
All other editions are obsolete.

SECURITY CLASSIFICATION OF THIS PAGE
UNCLASSIFIED

19. ABSTRACT (Continued)

a steady-state regime. When the mixing is explicitly accounted for by introducing parameterized turbulence, steady-state behavior results for the finely-zoned cases as well. The turbulent version of the model was validated by successfully calculating the stabilization height of an experimental plume generated at the Meteotron research facility in France.

Using an extended version of DICE which includes a tangential velocity component, an initial swirl velocity of 10 m/sec at the edge of a 10 km radius fire was found to "spin up" to swirl velocities in excess of 200 m/sec in the inflow layer near the axis of the fire. Plume heights for this case, which allowed no interaction of swirl with turbulence, were about 3 km lower than a corresponding non-rotating case. In order to accurately estimate the effects of swirl on turbulence, predictive equations for the full set of turbulent fluxes should be included in the model.

Accesion For

NTIS CRA&I
DTIC TAB
Unannounced
Justification

A-1
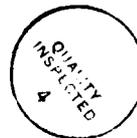
CONVERSION TABLE

Conversion factors for U.S. Customary to metric (SI) units of measurement

MULTIPLY ──────────► BY ──────────► TO GET

TO GET ◄────────── BY ◄────────── DIVIDE

angstrom	1.000 000 X E -10	meters (m)
atmosphere (normal)	1 013 25 X E +2	kilo pascal (kPa)
bar	1 000 000 X E +2	kilo pascal (kPa)
barn	1 000 000 X E -28	meter^2 (m^2)
British thermal unit (thermochemical)	1.054 350 X E +3	joule (J)
calorie (thermochemical)	4.184 000	joule (J)
cal (thermochemical)/cm^2	4 184 000 X E -2	mega joule/m^2 (MJ/m^2)
curie	3 700 000 X E +1	*giga becquerel (GBq)
degree (angle)	1 745 329 X E -2	radian (rad)
degree Fahrenheit	$t_k = (t°f + 459 67)/1.8$	degree kelvin (K)
electron volt	1.602 19 X E -19	joule (J)
erg	1.000 000 X E -7	joule (J)
erg/second	1.000 000 X E -7	watt (W)
foot	3.048 000 X E -1	meter (m)
foot-pound-force	1.355 818	joule (J)
gallon (U S liquid)	3 785 412 X E -3	meter^3 (m^3)
inch	2 540 000 X E -2	meter (m)
jerk	1 000 000 X E +9	joule (J)
joule/kilogram (J/kg) (radiation dose absorbed)	1.000 000	Gray (Gy)
kilotons	4 183	terajoules
kip (1000 lbf)	4 448 222 X E +3	newton (N)
kip/inch^2 (ksi)	6 894 757 X E +3	kilo pascal (kPa)
ktap	1 000 000 X E +2	newton-second/m^2 (N-s/m^2)
micron	1 000 000 X E -6	meter (m)
mil	2 540 000 X E -5	meter (m)
mile (international)	1.609 344 X E +3	meter (m)
ounce	2 834 952 X E -2	kilogram (kg)
pound-force (lbs avoirdupois)	4 448 222	newton (N)
pound-force inch	1.129 848 X E -1	newton-meter (N·m)
pound-force/inch	1 751 268 X E +2	newton/meter (N/m)
pound-force/foot^2	4.788 026 X E -2	kilo pascal (kPa)
pound-force/inch^2 (psi)	6.894 757	kilo pascal (kPa)
pound-mass (lbm avoirdupois)	4 535 924 X E -1	kilogram (kg)
pound-mass-foot^2 (moment of inertia)	4.214 011 X E -2	kilogram-meter^2 (kg·m^2)
pound-mass/foot^3	1 601 846 X E +1	kilogram/meter^3 (kg/m^3)
rad (radiation dose absorbed)	1.000 000 X E -2	**Gray (Gy)
roentgen	2 579 760 X E -4	coulomb/kilogram (C/kg)
shake	1 000 000 X E -8	second (s)
slug	1.459 390 X E +1	kilogram (kg)
torr (mm Hg, 0° C)	1.333 22 X E -1	kilo pascal (kPa)

*The becquerel (Bq) is the SI unit of radioactivity, 1 Bq = 1 event/s
**The Gray (Gy) is the SI unit of absorbed radiation.

TABLE OF CONTENTS

LIST OF ILLUSTRATIONS

LIST OF ILLUSTRATIONS (concluded)

LIST OF TABLES

SECTION 1

INTRODUCTION AND SUMMARY

1.1 BACKGROUND.

During the Second World War, both sides quickly discovered that fire, rather than blast, was the most efficient means of damaging large-area targets such as cities. In the latter stages of the strategic air offensive against Germany, for example, approximately 70% of the total tonnage of bombs dropped were incendiaries [1]. In certain instances where a large number of incendiaries were successfully dropped within a relatively small area, the resulting fires merged into one, termed a firestorm. Firestorms are characterized by the nearly complete burning of combustibles over a limited area, rather than partial combustion over a wide front. They generate severe surface effects due to high temperatures and winds, and are associated with the lofting of soot and debris to extreme altitudes.

A nuclear airburst occurring below an altitude of 100,000 feet delivers approximately 35% of its energy yield in the form of electromagnetic radiation at infrared and visible wavelengths [2]. Since the incendiary effect of this radiation is concentrated within a compact area, nuclear bursts could serve as efficient mechanisms for initiating firestorms. While the burning radii for the fires following the Hiroshima and Nagasaki attacks were of order 1 km and those for the largest firestorms occurring in the European theater ranged up to 3 km, the expected burn radius for a nominal 1-Mt airburst is 10 km. Due to the unprecedented size of the postulated fires and the limitations of simplified analytical plume models, numerical simulations are necessary to provide reliable estimates of the near-surface environments and particulate clouds generated by mass fires following a nuclear airburst.

1

1.2 APPROACH.

In this study, several simulations were made with the DICE code in order to investigate the dependence of the predicted firestorm environments on a variety of physical and computational factors. DICE is an axisymmetric two-dimensional numerical model based on the compressible flow equations [3]. The grid spacing can vary both horizontally and vertically, with each cell representing an average over an annular region (see Fig. 1). The model predicts the flow of air obeying the AFWL equation of state, and can include solid, liquid, or gaseous contaminants (e.g., soot and water species), which exchange heat and momentum with the air. The process of combustion is modeled by adding heat at a prescribed rate to the lowest layer of computational cells over the burning area. The initial atmospheric temperature profile was taken from the U.S. Standard Atmosphere, with the tropopause located at an altitude of 11 km (see Fig. 2).

Section 2 contains a brief overview of the model. In Section 3, an inviscid version of the model is used to investigate the effects of variations in the computational zone size, burning rate, burning area, and multi-phase physics. In Section 4 a simplified turbulence model is introduced, and the influence of turbulence on the temperatures and stabilization heights of thermal plumes is discussed. Section 5 describes the validation of the model by the successful simulation of a test fire conducted at the Meteotron research facility in France. In Section 6 the question of swirl is addressed, and it is shown that significant rotational velocities can be generated by large-area fires.

2

Multiphase DICE Code Numerical Simulation Approach

AXIS

ALTITUDE, Z

Z = 0 IS
GROUND
SURFACE

RADIUS, R → R_b

EACH COMPUTATIONAL
CELL CONTAINS:

1. Air variables (P, ρ, e, $\vec{u}$)

2. Solid/liquid/vapor variables
   for additional groups
   $(\rho, e, \vec{u})_\ell$ $\ell = 1, 9$

   • soot and larger debris
     by size
   • water/ice by size/shape

   • water vapor

BURNING IS SIMULATED BY ADDING ENERGY AT A
SPECIFIED RATE TO CELLS ALONG THE GROUND
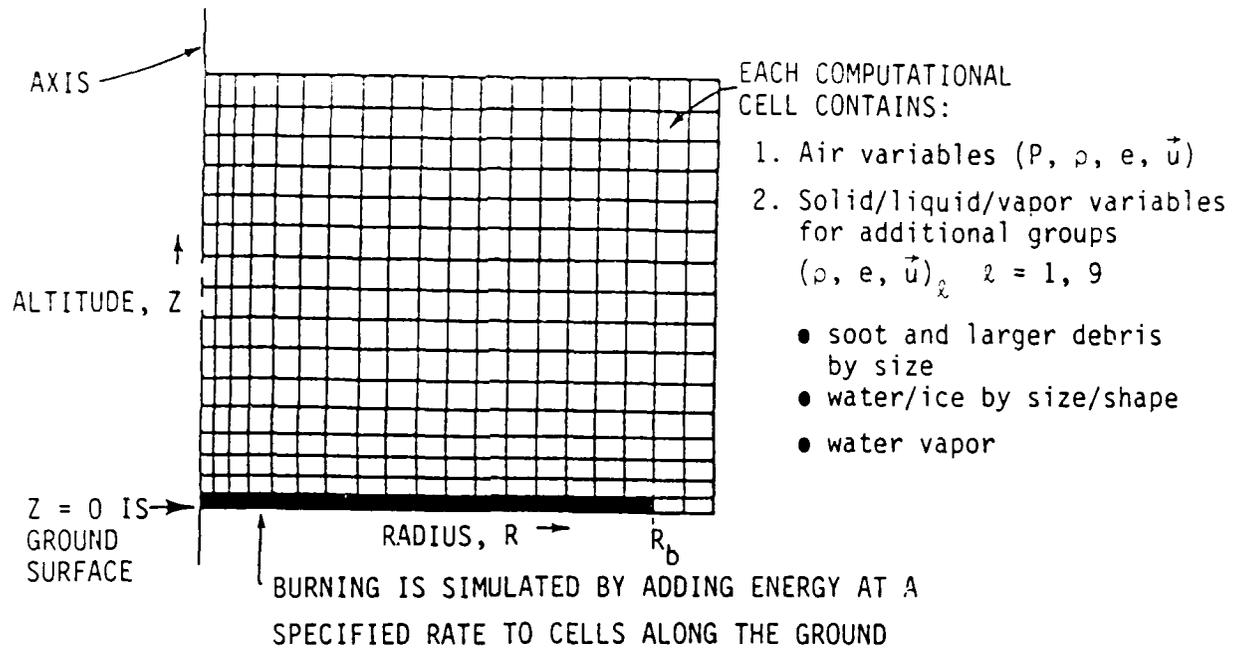
• *AXISYMMETRIC GEOMETRY*

TOP VIEW OF A
BURNING CELL

AXIS
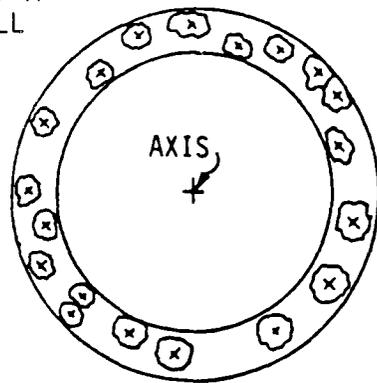
COMBUSTION PRODUCTS/ENERGY RELEASED FROM
FIRES ON/NEAR GROUND SURFACE ARE AVERAGED
OVER CELL VOLUME.

Figure 1.   Schematic illustration of DICE grid and cell geometry.

3
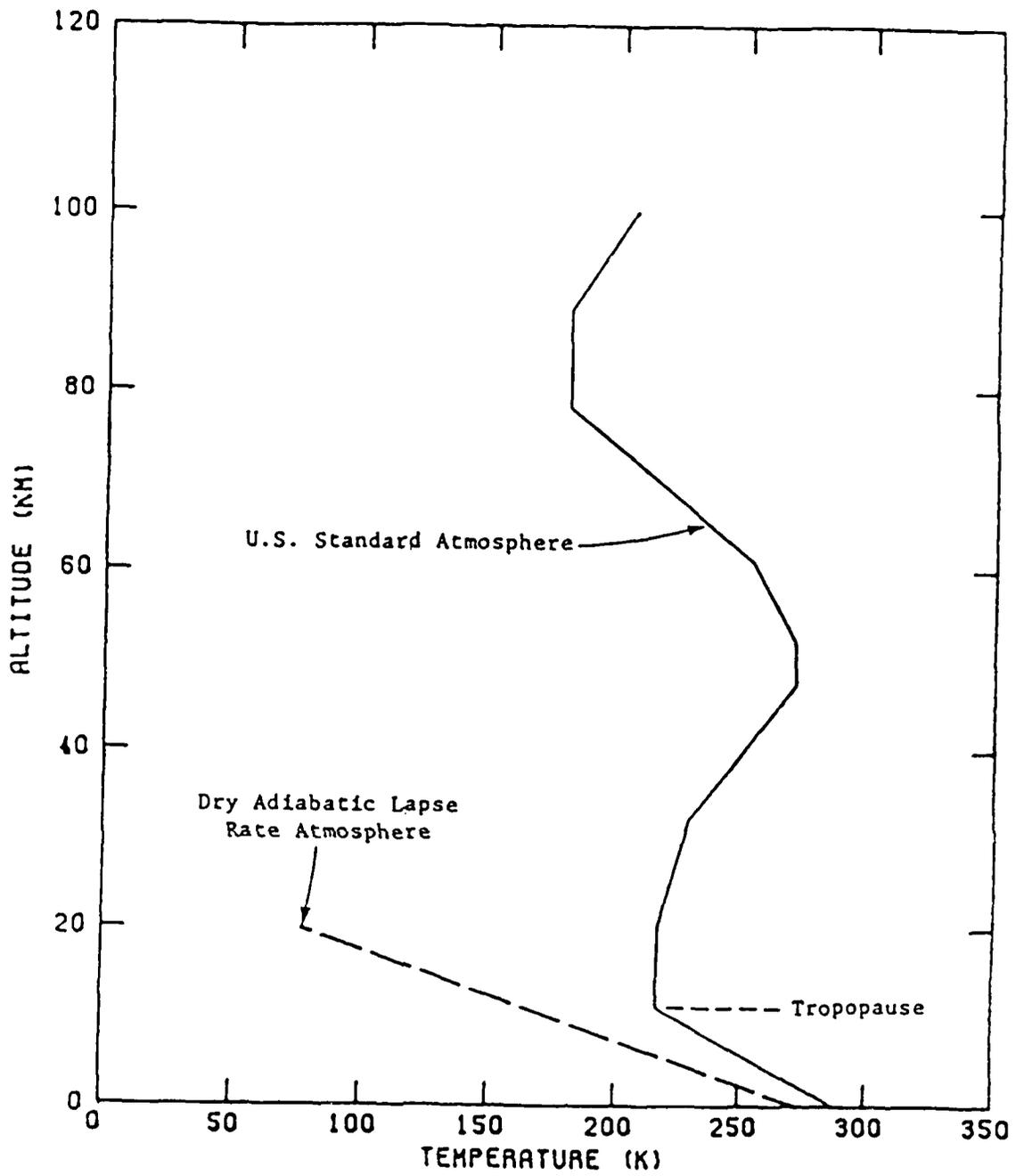
Figure 2. Vertical temperature profile comparison for a U.S. standard atmosphere and a dry adiabatic lapse rate atmosphere.

4

1.3 SUMMARY.

Inviscid Cases

An inviscid version of the model was used to study the effects of variations in the burn rate, burn area, computational zone size, and multi-phase physics on the predicted firestorm environments (see Table 1). Two different time-dependent burning rates were used (see Fig. 3): a "fast" scenario in which the maximum burn rate of 250 kw/m^2 (representative of firestorms) was maintained for 30 minutes, and a "slow" scenario in which the maximum burn rate of 62.5 kw/m^2 (representative of group fires) was maintained for 120 minutes.

The main conclusions drawn from the inviscid cases were as follows:

(1) When the lower layer (where the combustion heating is added) is given a depth of only 100 m and the "fast" burning scenario is used (Cases 301 and 502), temperatures in excess of 1000°K are generated (see Fig. 4, which shows a time history of the maximum temperature for Case 502). The large buoyancy which results causes intense, jet-like plumes to rise along the axis to altitudes in excess of 40 km, where they become over-dense and fall back downwards. This tendency of the plumes to overshoot their stabilization heights leads to solutions which are quasi-periodic (see Fig. 4; see also Figs. 5a-b, which show time histories of the inflow velocities at various locations in the lower layers of Cases 301 and 502), and causes the formation of two distinct regions of lofted soot (see Figs. 6a-b, which show the positions reached after one hour by massless tracers released every five minutes from within the burning area of Cases 301 and 502), one in the stratosphere near the axis, and another extending radially outwards near the altitude of the tropopause.

5

Table 1. Inviscid firestorm simulation cases.

CASE	BURN RATE	BURN RADIUS (KM)	MINIMUM ΔZ (km)	MINIMUM Δr (km)	SOOT	WATER VAPOR (% of mass burned)
301	fast	10	0.1	0.33	0	0
502	fast	10	0.1	0.67	0	0
504	slow	10	0.1	0.67	0	0
601	fast	10	1.0	1.0	0	0
603	fast	10	1.0	1.0	5	50
604	slow	10	1.0	1.0	5	50
605	fast	30	1.0	1.0	5	50
606	fast	3	1.0	1.0	5	50
608	fast	10	1.0	1.0	5	50 + ambient
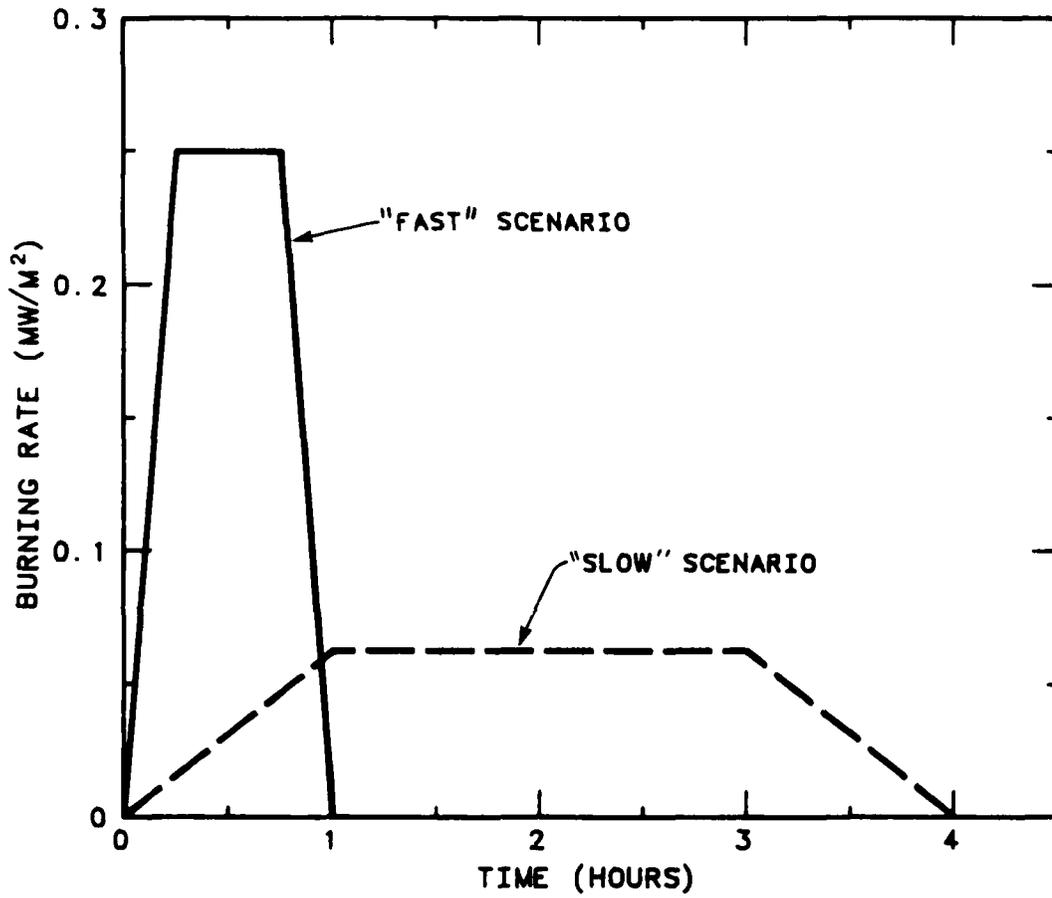
Figure 3. Time dependence of burning rates used in firestorm simulations.
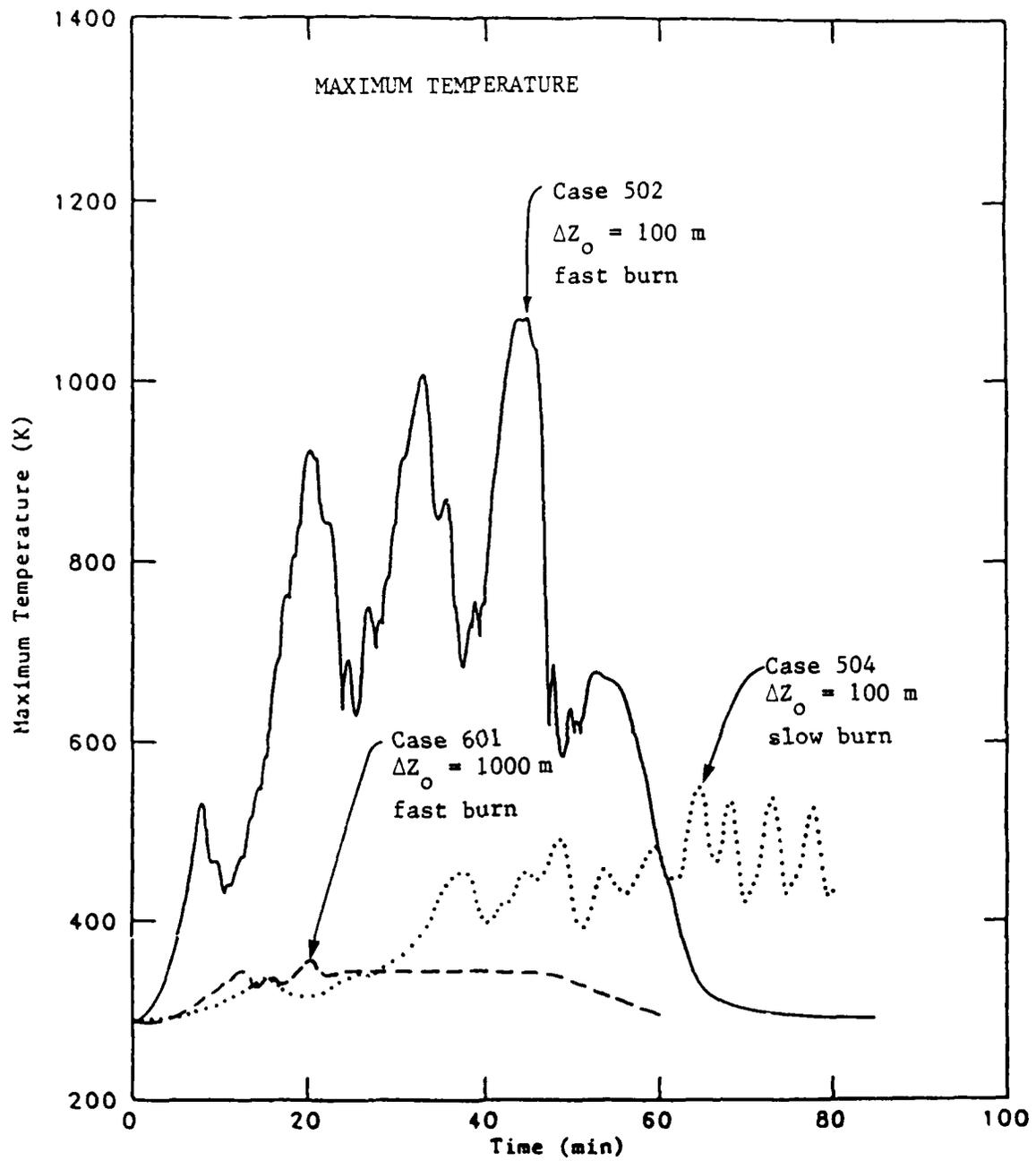
Figure 4. Time histories of maximum temperatures for Cases 502, 504, and 601.

8

Figure 5b. Radial velocities in lowest layer of computational cells at various radial distances for Case 502.

Figure 5a. Radial velocities in lowest layer of computational cells at various radial distances for Case 301.

Figure 5d. Maximum inward velocity vs. time near the ground for Cases 502 and 504.

Figure 5c. Radial velocities in lowest layer of computational cells at various radial distances for Case 504.

(2) When the lower layer is given a depth of 1 km (the 600-series in Table 1), the combustion heating is effectively "mixed" over the lowest 1 km of the domain, leading to much cooler temperatures (see the plot in Fig. 4 of the maximum temperatures for Case 601, which differed from Case 502 only in the changed zoning). The reduced buoyancy lessens the tendency of the plume to overshoot, and it approaches a steady-state with a maximum altitude of about 18 km by 30 minutes into the run (see Figs. 7a-b, which show velocity vector plots of Case 601 at 30 and 45 minutes). As a result, the upper cloud of soot tracers which developed in Cases 301 and 502 does not appear in the tracer plot for Case 601 (see Fig. 6d), although the lower tracer cloud extending outwards along the tropopause is still present.

(3) Additional information is gained by using the multiphase capabilities of the model to predict concentrations of soot, water vapor, liquid water, and ice within the grid. For Cases 603-608 in Table 1, 5% of the fuel burned is converted to soot, and 50% to water vapor; Cases 603-606 neglect ambient water vapor, while Case 608 assumes an initial relative humidity which varies linearly from 60% at the surface to zero at an altitude of 30 km. Case 603, using the same parameters as the single-phase Case 601, predicts a soot concentration field at one hour (see Fig. 8) which resembles the tracer cloud from Case 601 (see Fig. 6d), but also shows that the highest soot concentrations are located near the axis, and that considerable vertical dispersion occurs within the cloud. The ice/water cloud also has a maximum concentration on the axis, and it is likely that latent heat released by the condensing water vapor in this region accounts or for the secondary maxima shown by the particulate clouds near the axis in the stratosphere. When ambient moisture is included in the calculation, however, the effects of latent heating can be much larger; Fig. 9 shows that for Case 608, which had a moderately humid initial atmosphere but was otherwise identical to Case 603, the plume exceeds an altitude of 30 km by 30 minutes.

11

Figure 6b. Tracer positions at 60 minutes for Case 502.

Figure 6a. Tracer positions at 60 minutes for Case 301.

12

Top figure (Figure 6d):

INITIALIZATION TIMES

0	0 MINUTES
1	5 MINUTES
2	10 MINUTES
3	15 MINUTES
4	20 MINUTES
5	25 MINUTES
6	30 MINUTES
7	35 MINUTES
8	40 MINUTES
9	45 MINUTES
A	50 MINUTES
B	55 MINUTES
C	60 MINUTES

Radius (km)

Figure 6d. Tracer positions at 60 minutes for Case 601.

Bottom figure (Figure 6c):

INITIALIZATION TIMES

0	0 MINUTES
1	5 MINUTES
2	10 MINUTES
3	15 MINUTES
4	20 MINUTES
5	25 MINUTES
6	30 MINUTES
7	35 MINUTES
8	40 MINUTES
9	45 MINUTES
A	50 MINUTES
B	55 MINUTES
C	60 MINUTES
D	65 MINUTES
E	70 MINUTES
F	75 MINUTES
G	80 MINUTES
H	85 MINUTES
I	90 MINUTES
J	95 MINUTES
K	100 MINUTES
L	105 MINUTES
M	115 MINUTES
N	120 MINUTES

Radius (km)

Figure 6c. Tracer positions at 120 minutes for Case 504.

13

Figure 7b. Velocity vector plot for Case 601 at 45 minutes.

Figure 7a. Velocity vector plot for Case 601 at 30 minutes.

14

SOOT AND ICE/WATER CONCENTRATIONS (mgm/m^3)

BASELINE BURNING MODEL (CASE 603)

$\dot{q}_b = 0.25\ MJ/m^2/s$

$R_b = 10\ km$

$t = 1$ hour
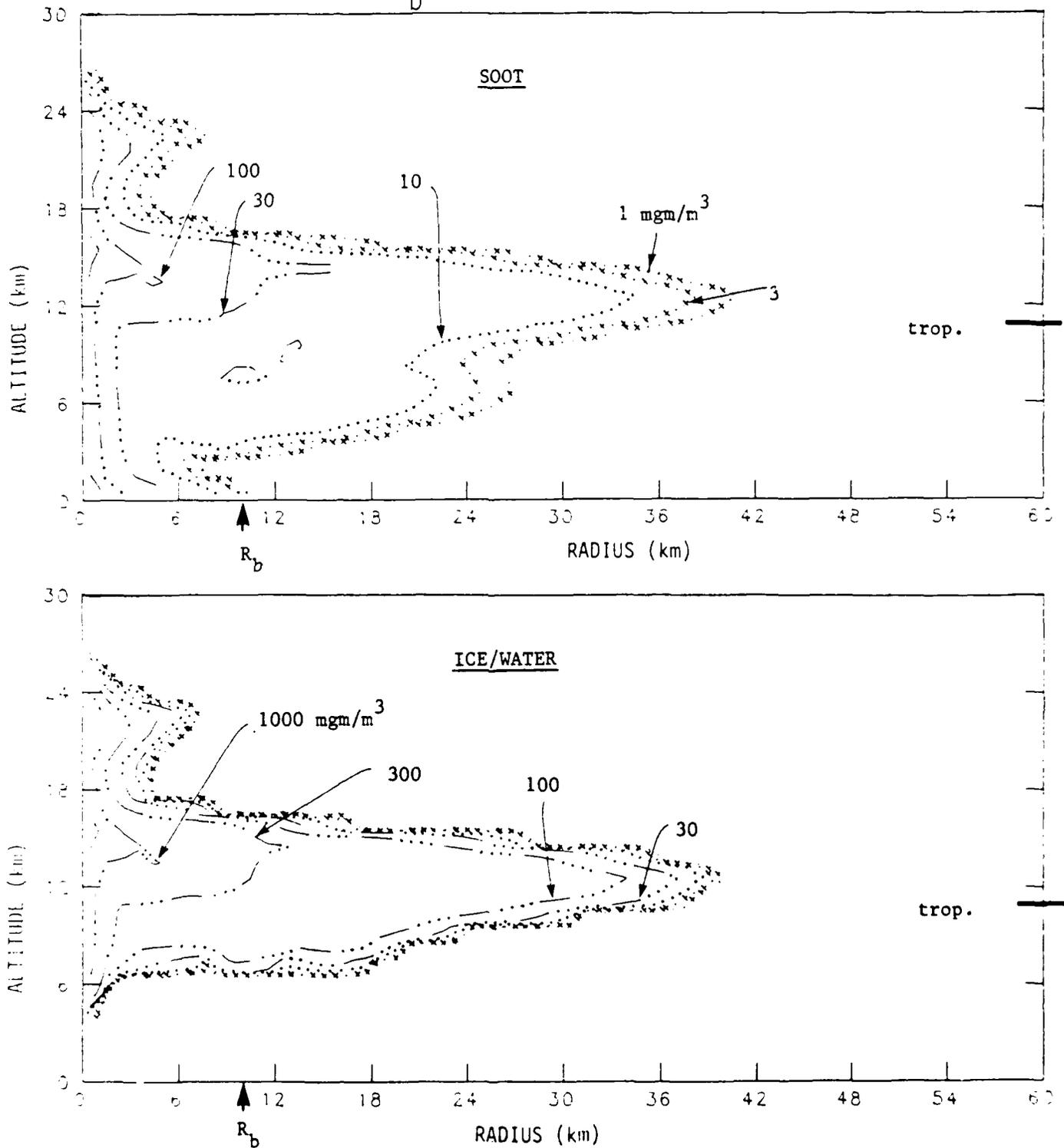
Figure 8. Particulate clouds for Case 603 at 1 hour.

15
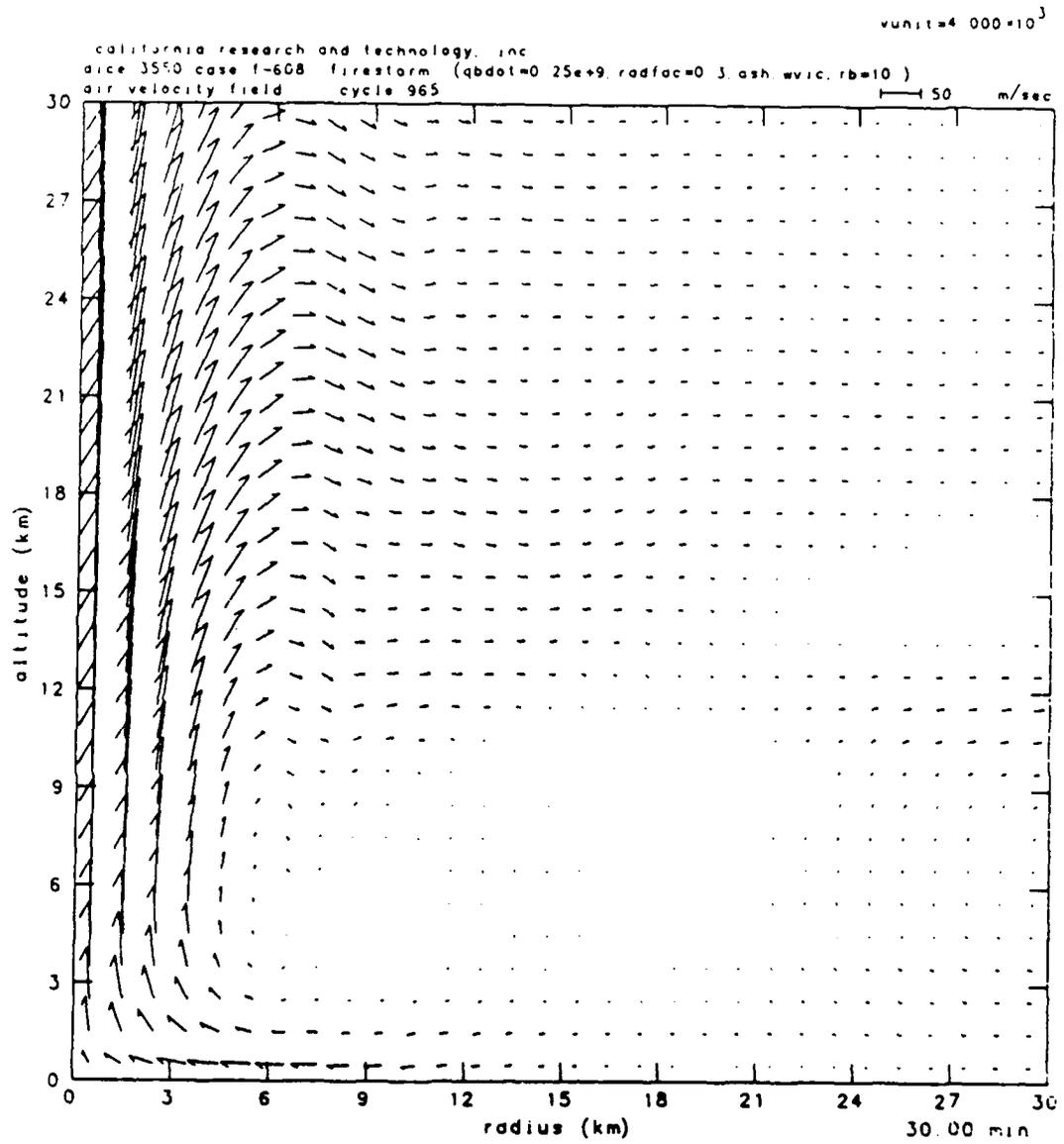
Figure 9. Velocity vector plot for Case 608 at 30 minutes. (Includes ambient atmospheric humidity).

(4) When the burning rate for a 10-km radius fire is changed
from the "fast" scenario (Case 502) to the "slow" scenario
(Case 504), peak temperatures drop from about 1000°K to 500°K
(see Fig. 4), and inflow speeds in the lower layer are reduced by
about a factor of two (compare Figs. 5b-c). Fig. 6c shows that
the lower cloud in Case 504 stabilizes at about half the altitude
of the lower cloud in Case 502 (5 km vs 10 km) and spreads
outwards at about half the rate (reaching a radial distance of
30 km at 2 hours vs 1 hour), while the height of the upper cloud
is reduced from 25 km to 15 km. Similar results are obtained
from a comparison of the multi-phase Cases 603 ("fast" burn) and
604 ("slow" burn), with the level of the upper concentration
maximum descending from 22 km to 12 km when the burn rate is
reduced, and the lower maximum descending from 12 km to 5 km
(compare Figs. 8 and 10).

(5) For a fixed burning rate, the stabilization height of the
soot cloud depends strongly on the size of the fire. The soot
cloud for Case 606, which uses parameters characteristic of the
largest World War II firestorms ("fast" burn rate and 3-km burn
radius), had a maximum altitude of 14 km and was confined largely
to the troposphere (see Fig. 11). For Case 603, which used the
"fast" burning scenario and a radius of 10 km (considered the
nominal burn radius for a 1-MT airburst), maximum soot
concentrations occur in the stratosphere, and the cloud top
extends to an altitude of 26 km (see Fig. 8). When the fire
radius is increased to 30 km with the same burn rate, the plume
exceeds an altitude of 40 km by 45 minutes (see Fig. 12a).

For the inviscid cases which used the "fast" burning
scenario and a dry atmosphere, two types of solution were
obtained, depending on the amount of mixing which is allowed to
occur in the boundary layer. When the combustion heating is
confined to a layer 0.1 km thick, high temperatures result,
leading to overshooting plumes and a quasi-periodic solution;
when the combustion heating is "mixed" over a lower layer depth

17

SOOT AND ICE/WATER CONCENTRATIONS (mgm/m^3)

REDUCED BURNING RATE MODEL (CASE 604)

$\dot{q}_b = 0.0625$ $MJ/m^2/s$, $R_b = 10$ km

t = 4 hours
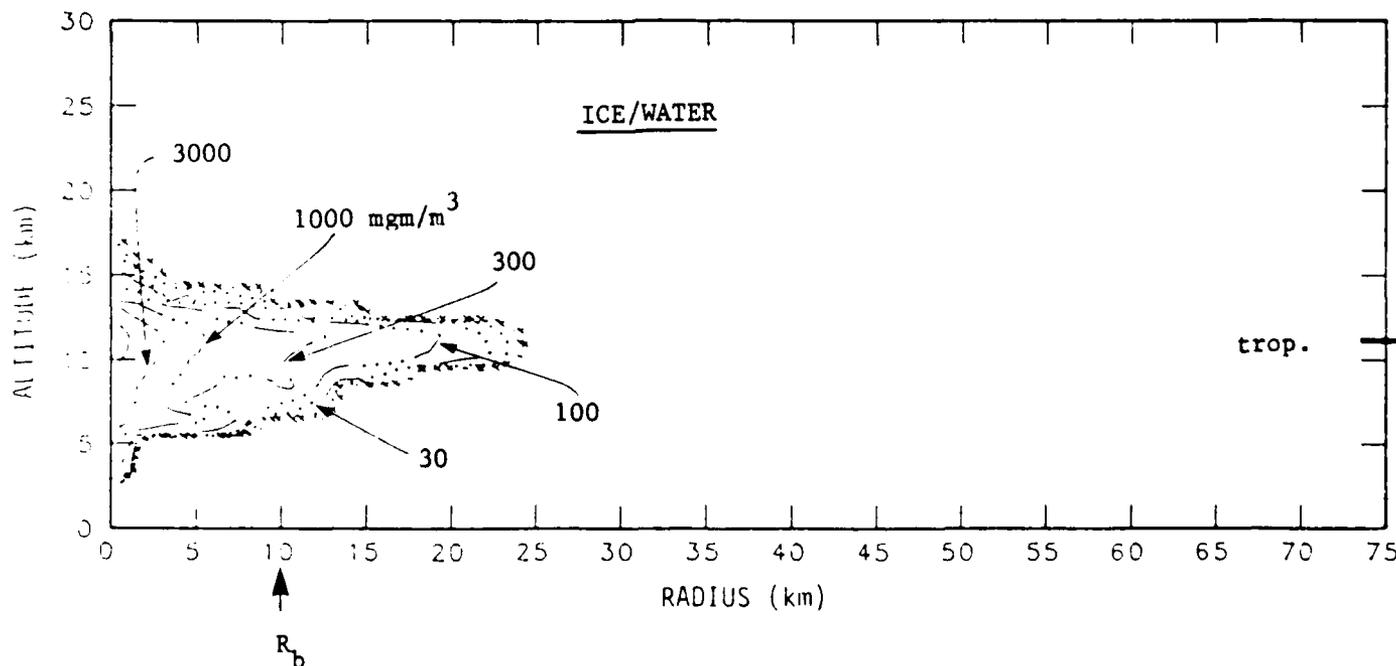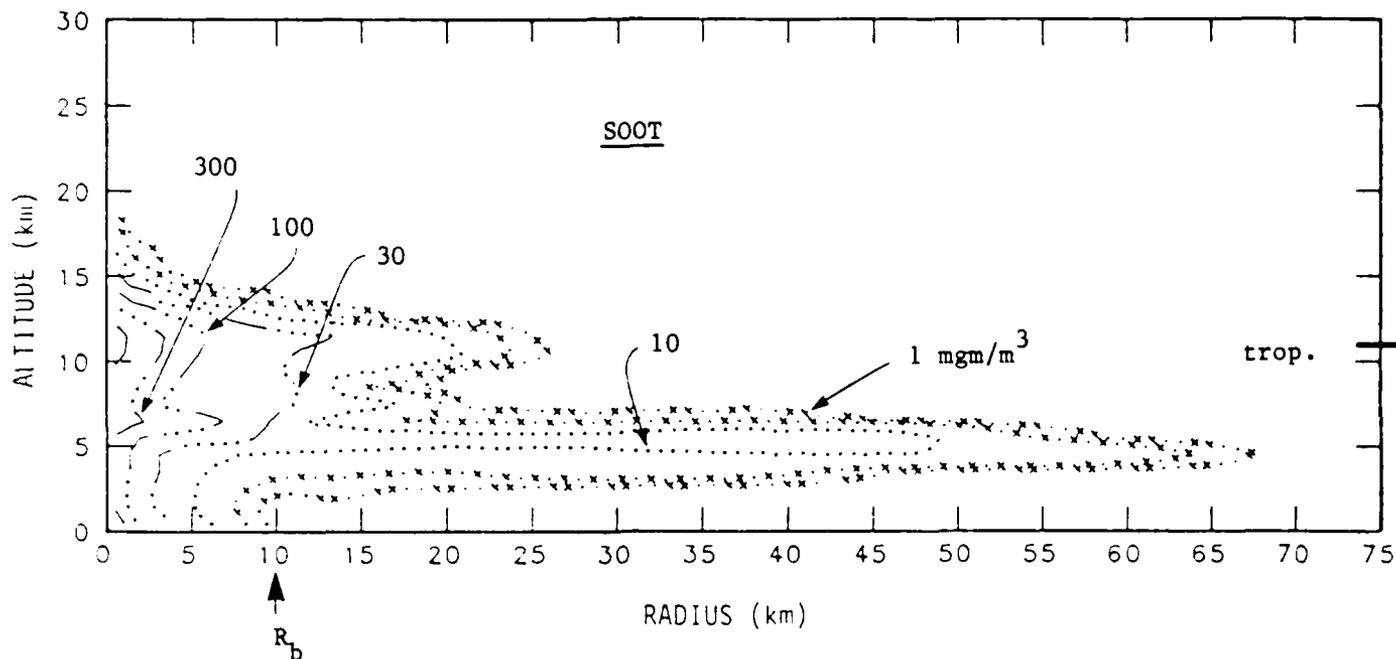
Figure 10. Particulate clouds for Case 604 at 4 hours.

18

SOOT AND ICE/WATER CONCENTRATIONS (mgm/m^3)
R$_b$ = 3 km RADIUS BURN (CASE 606)
$\dot{q}_b$ = 0.25 MJ/m^2/s   t = 1 hour
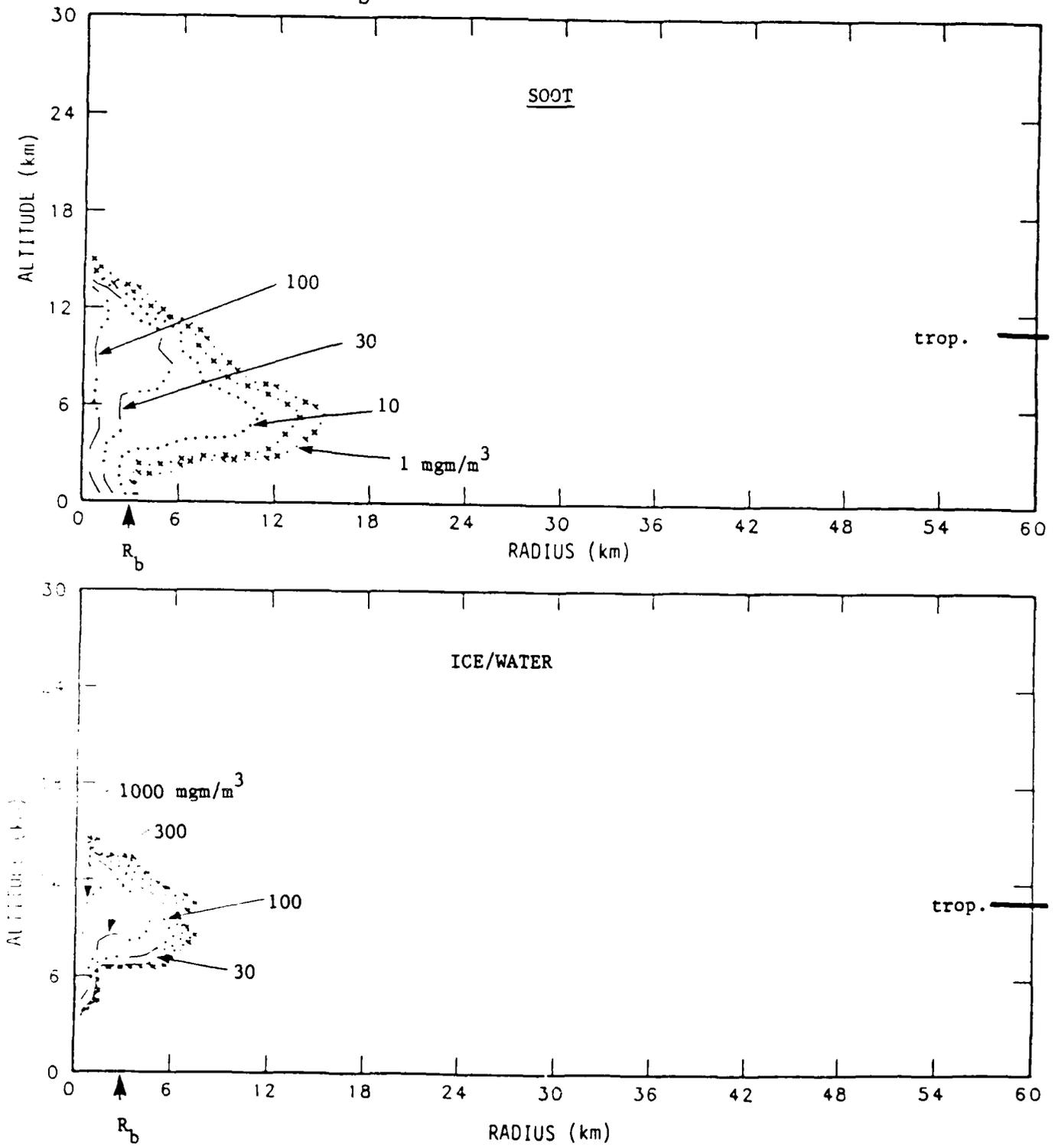
Figure 11. Particulate clouds for Case 606 at 1 hour.

19

VELOCITY FIELD PLOTS FOR CASE 605
(R_b = 30 km, $\dot{q}$ = 0.25 MJ/m^2/sec, 15 minutes to max rate)
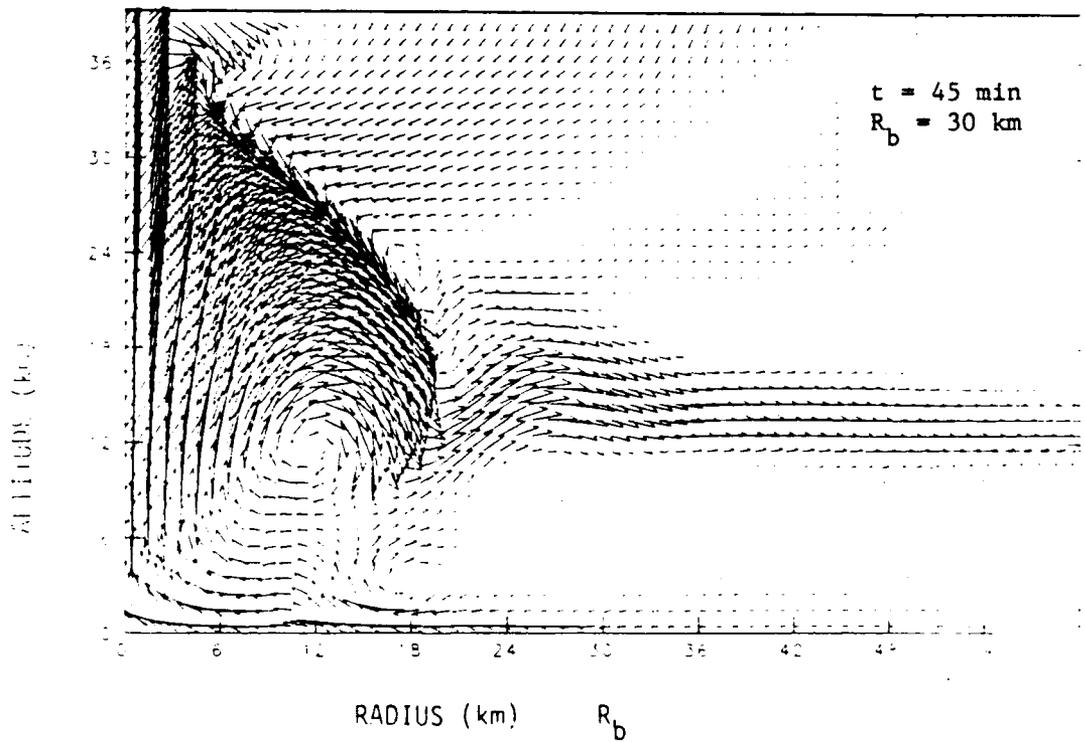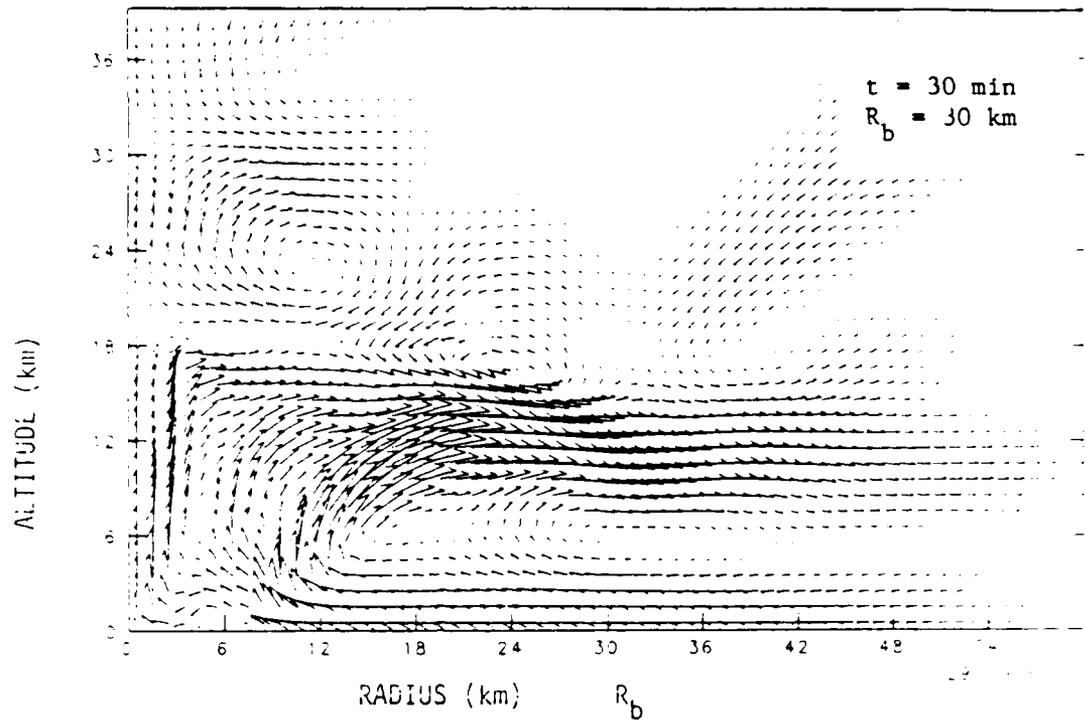
Figure 12a. Velocity field plots for Case 605 at 30 and 45 minutes.

SOOT AND ICE/WATER CONCENTRATIONS (mgm/m³)

R_b = 30 km RADIUS BURN (CASE 605)

$$\dot{q}_b = 0.25 \text{ MJ/m}^2/\text{s}$$

t = 30 minutes
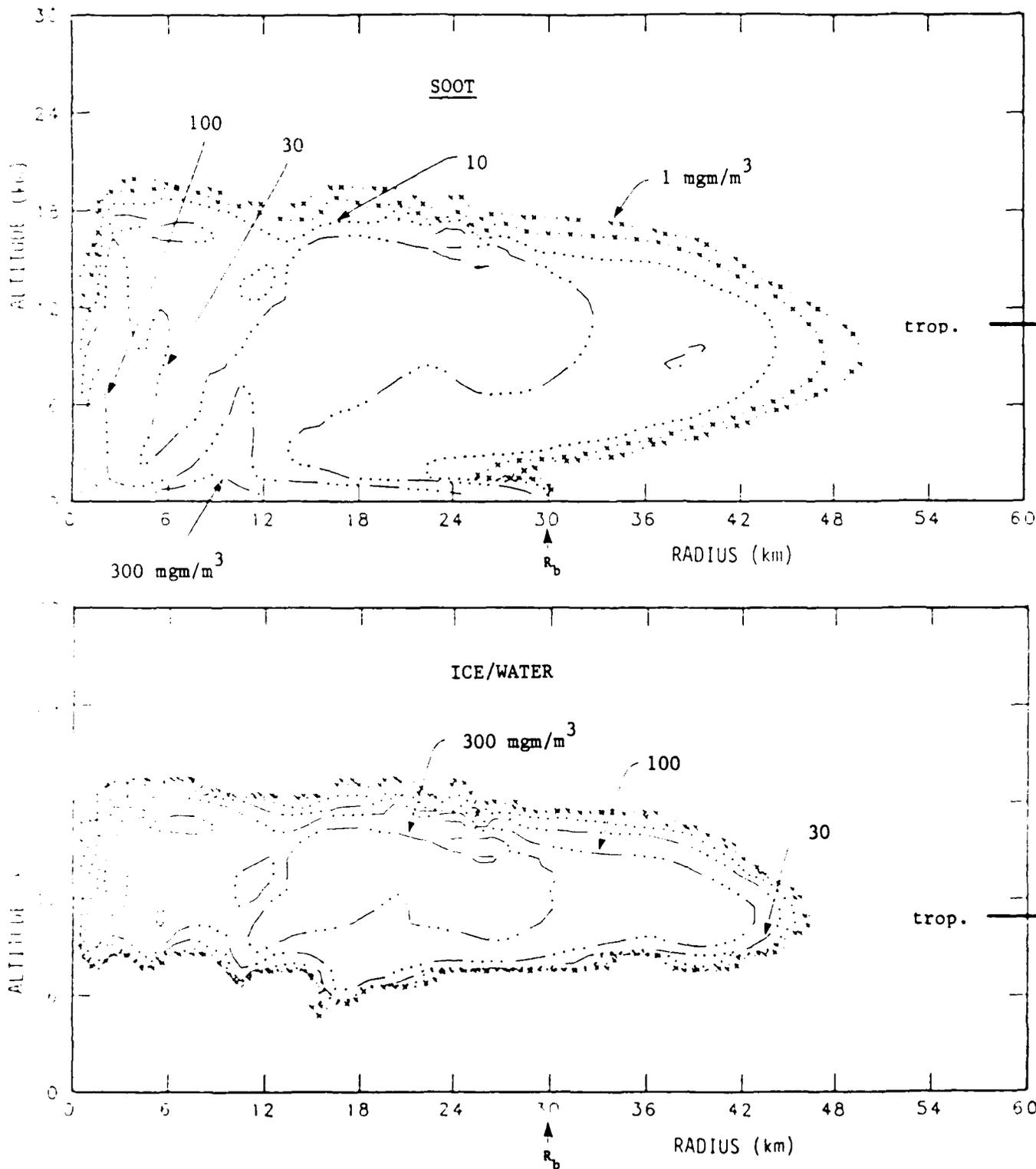
Figure 12b. Particulate clouds for Case 605 at 30 minutes.

21

of 1.0 km, however, cooler temperatures and less energetic plumes lead to solutions which approach a steady state during the constant heating phase.

Although in general we do not expect periodic solutions from non-periodic heat sources, the fires which we are simulating are of unprecedented size (with a typical width more than twice the e-folding depth of the atmosphere), and the oscillatory behavior which was obtained may have a physical basis. Mixing evidently plays a key role in the dynamics of the plumes, however, and in order to resolve this question, a more systematic treatment of its effects in the model is needed.

Turbulent Cases

To this end, a simplified turbulence sub-model has been developed and incorporated into the code. The turbulent transports of heat and momentum are modeled according to

$$\overline{U_i' U_j'} = \frac{q^2}{3} \delta_{ij} - q \ell_1 S_{ij} \qquad (1)$$

and

$$\overline{U_i' \theta'} = - q \ell_2 \frac{\partial \overline{\theta}}{\partial x_i} , \qquad (2)$$

where

$$S_{ij} \equiv \frac{\partial \overline{U_i}}{\partial x_j} + \frac{\partial \overline{U_j}}{\partial x_i} , \qquad (3)$$

θ is the potential temperature, q is the r.m.s. turbulent velocity, overbars denote ensemble means, primes denote turbulent variations, and ℓ_1, ℓ_2, and Λ_1 (used below) are turbulent length scales. Assuming a local balance between shear production, buoyant production, and dissipation, the above expressions may be inserted into the turbulent kinetic energy equation to give a diagnostic relation for q:

$$q^2 = \Lambda_1 \ell_1 \left[S_{ij} \; S_{ij} - \frac{\ell_2}{\ell_1} \frac{g_i}{\theta_o} \frac{\partial \overline{\theta}}{\partial x_i} \right] , \qquad (4)$$

where g_i is the acceleration of gravity and θ_o is a reference temperature.

We let $\ell_1 = A_1 \ell$, $\ell_2 = A_2 \ell$, and $\Lambda_1 = B_1 \ell$, where ℓ is a master turbulent length scale, and A_1, A_2, and B_1 are constants known from measurements. To specify the master turbulent length scale, we first identify a natural length scale in the flow, and then determine the relationship between the natural and turbulent length scales. In the inflow layer the height above the surface is a natural length scale, and we can use Blackadar's [4] formula for the turbulent length scale

$$\ell = \ell_\infty \frac{\kappa z}{\kappa z + \ell_\infty} , \qquad (5)$$

where κ is von Karmen's constant and z is the height. For large values of z the turbulent length scale asymptotically approaches ℓ_∞, which is a prescribed constant for each case.

In order to investigate the effects of parameterized turbulence on the solutions, Cases 702 and 705 were run with the same grid and burning rate as Case 502 (see Table 2), using the turbulence sub-model with asymptotic mixing lengths of 100 m and 25 m, respectively. The main conclusions drawn from these two cases were:

(1) The maximum temperatures which developed (see Fig. 13) were intermediate between those occurring in the finely zoned inviscid Case 502 and the coarsely zoned inviscid Case 601 (see Fig. 4). Case 705, which had the smaller mixing length of the two turbulent cases, experienced less turbulent mixing in the inflow layer and therefore had higher maximum temperatures than Case 702.

Table 2. Turbulent firestorm simulation cases.

CASE	BURN RATE	BURN RADIUS (km)	MINIMUM ΔZ (km)	ℓ_∞ (m)	SWIRL
702	fast	10	0.1	100	no
705	fast	10	0.1	25	no
841	fast	10	0.1	100	yes
846	fast	10	0.1	$100 \longrightarrow 25$	no
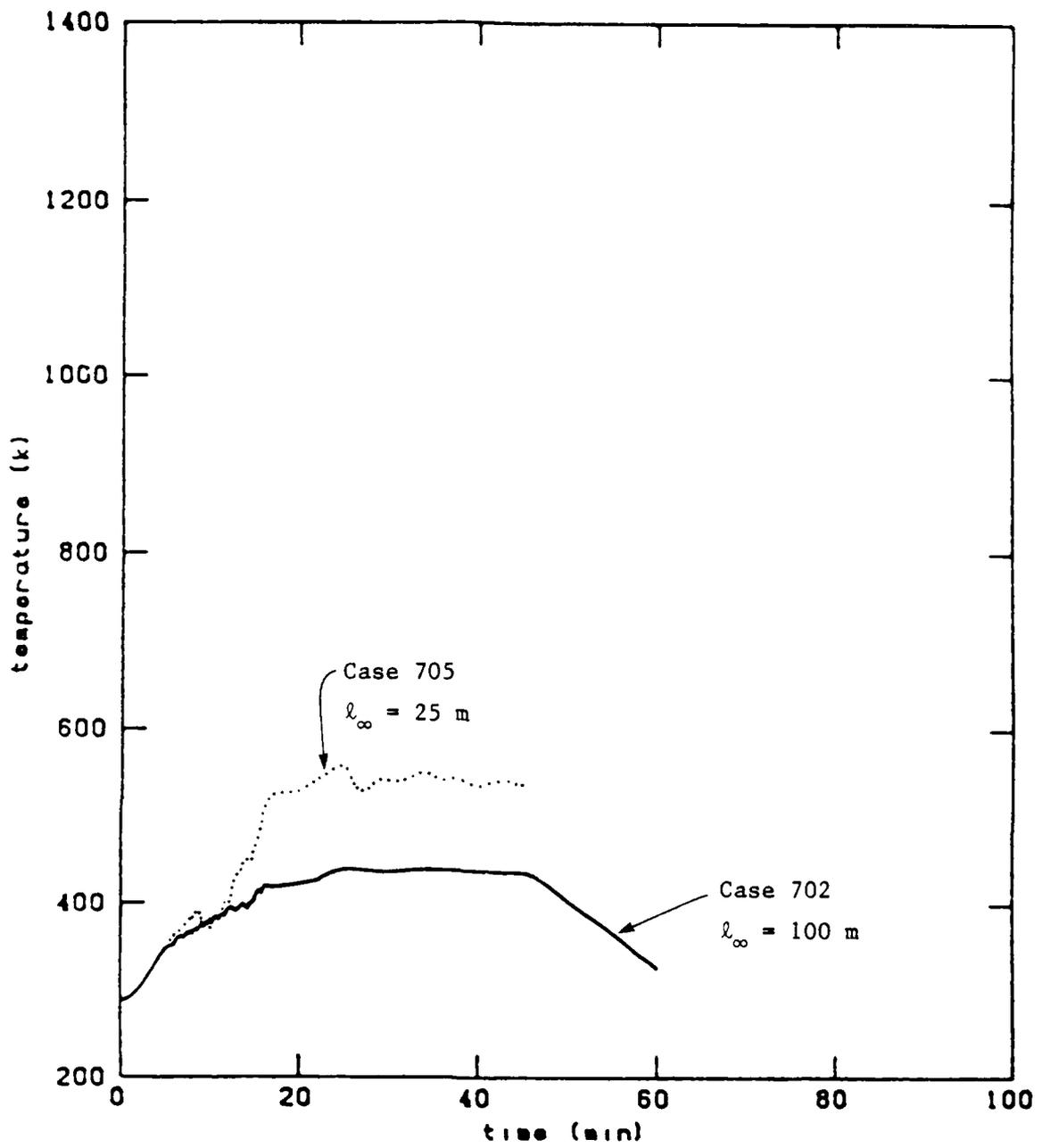
Figure 13. Time histories of maximum temperature for Cases 702 and 705.

(2) The plume heights for the two turbulent cases (see
Figs. 14a-d) were also intermediate between those for the
inviscid Cases 502 (40 km, not shown) and 601 (18 km, see
Fig. 7). The plume for Case 705, which had higher temperatures
and therefore greater buoyancy, reached a height of over 30 km,
while 702's plume reached a maximum height of about 24 km; the
soot tracer clouds for Case 705 were also about 3 km higher than
the corresponding clouds for Case 702 at 45 minutes (see
Fig. 15). Although both plumes showed considerable overshoot,
leading to the formation of two distinct clouds of the tracers
released at late times (note that the tracers in Fig. 15 are
numbered sequentially according to time-of-release), both of the
turbulent cases reached a quasi-steady state by 30 minutes
(compare Figs. 14c-d).

These results show that the dynamics of the plumes, and in
particular their stabilization heights, are sensitive to the
value of ℓ_∞ which is chosen. Based on a formulation due to
Yamada and Mellor [5], it can be shown that ℓ_∞ should have a
value between 1/10 and 1/7 of the boundary layer depth, and this
fact can be used to calibrate the value of the asymptotic mixing
length to be used for a given problem.

Approximate boundary layer depths for four of the cases are
shown in the column labeled Δ in the table appearing in Fig. 16.
These boundary layer depths were estimated by taking the height of
the 25°K overtemperature isotherm at 5 km radius at 30 minutes.
We picked this height because this is (approximately) equal to the
cell depth in Case 601. Since 601 has no turbulent mixing between
the cells, the cell depth is the same as the mixed or "turbulent"
layer depth when the flow is horizontal. This is the case for 601
(see Fig. 7). For Cases 705 and 702, the values of ℓ_∞/Δ are 1/24
and 1/8, respectively. ℓ_∞/Δ would have to be smaller than 1/24
for Case 502 and greater than 1/8 for Case 601 to produce the
"observed" boundary layer depths.
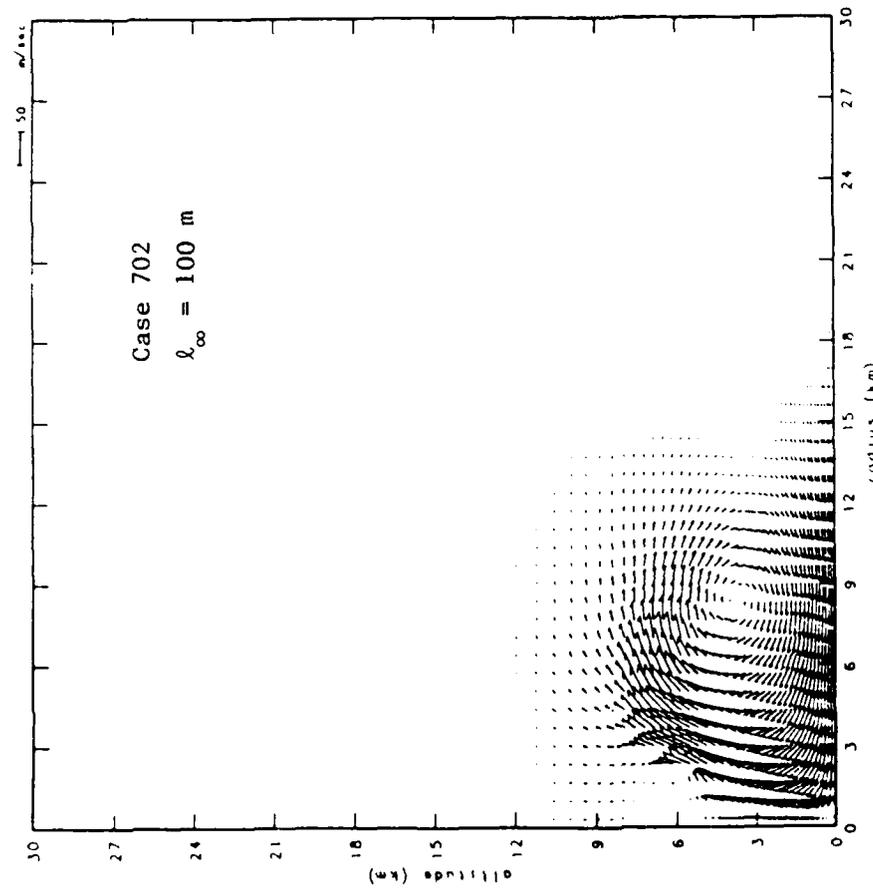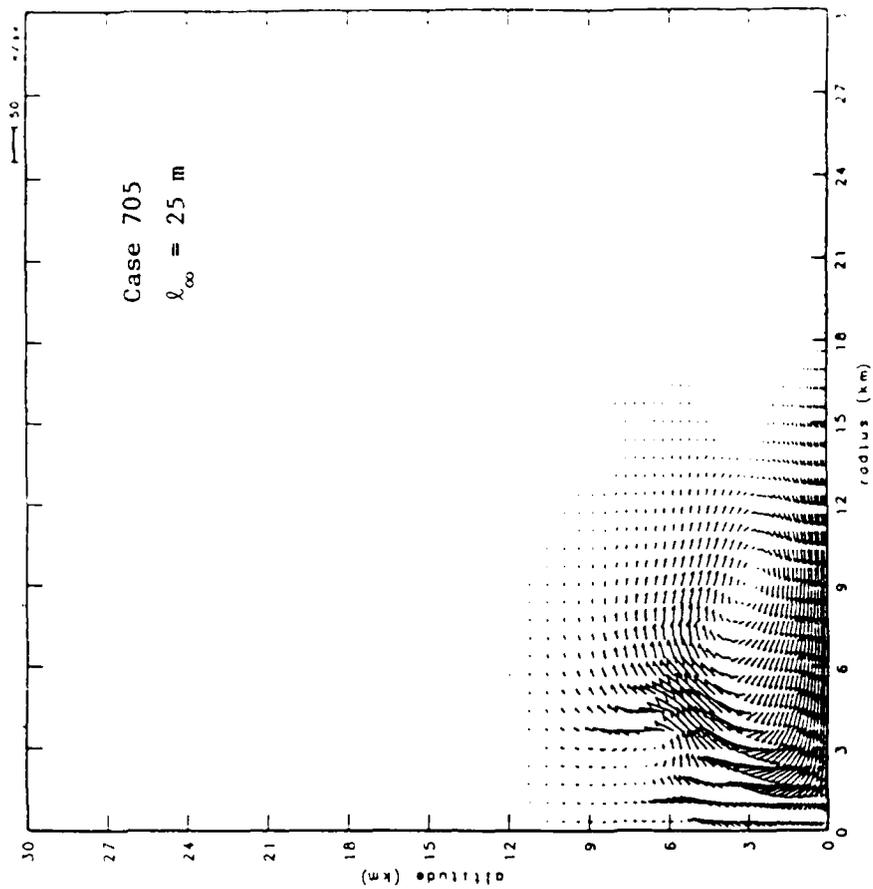
Figure 14a. Velocity vector plots for Cases 702 and 705 at 15 minutes.

27
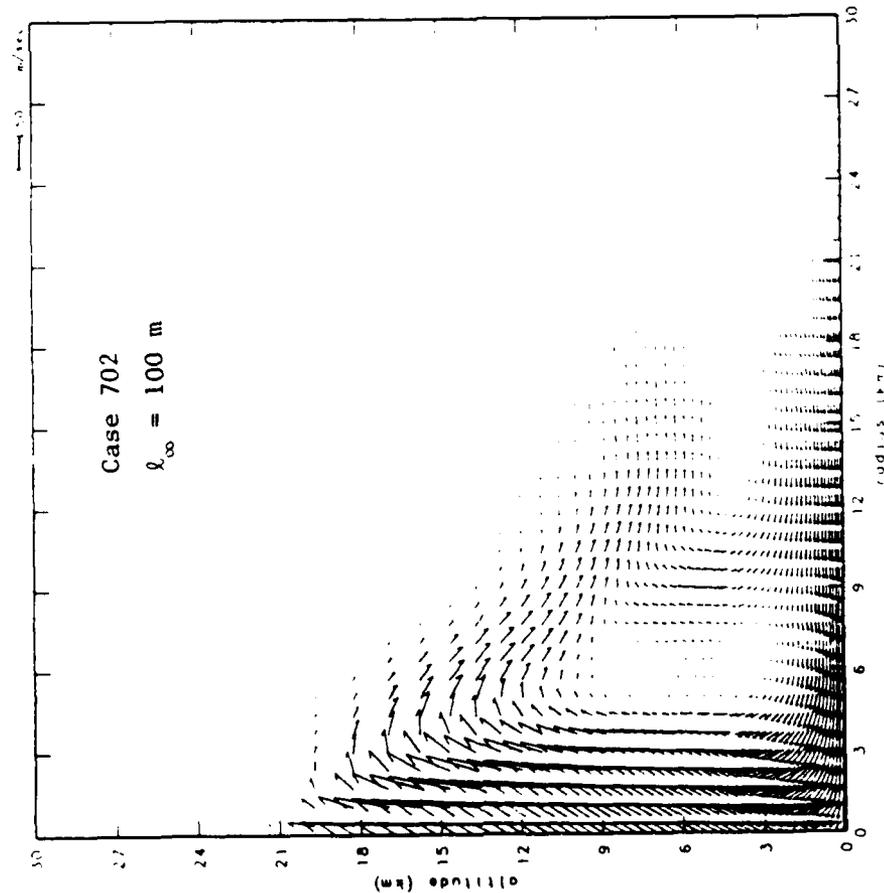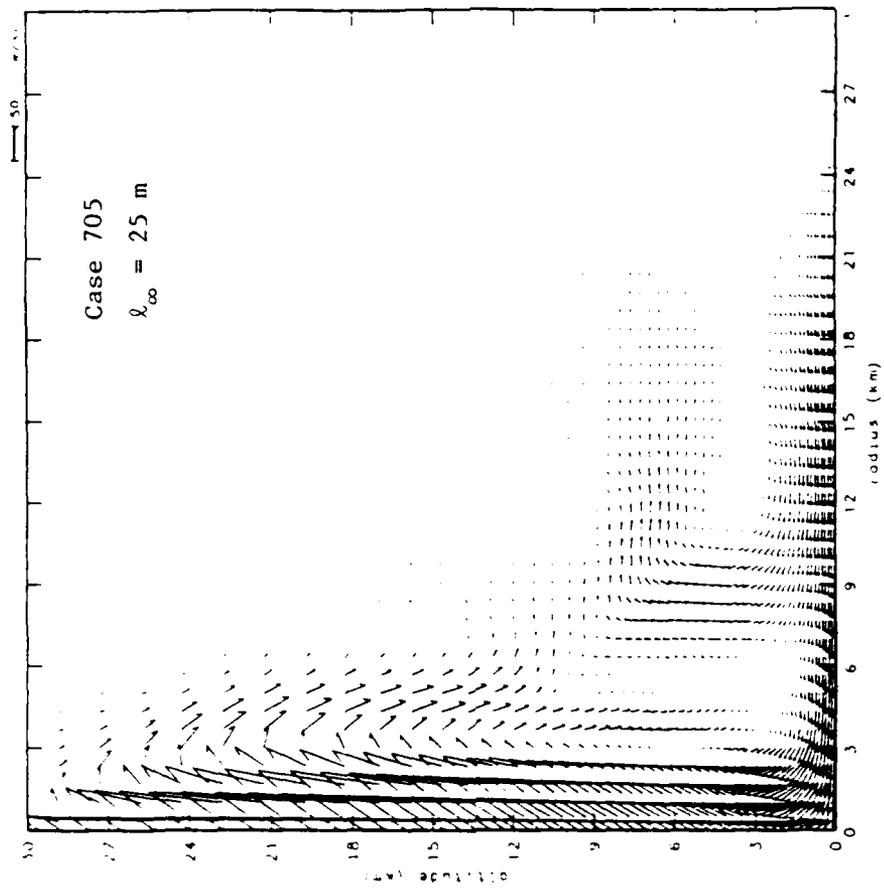
Figure 14b. Velocity vector plots for Cases 702 and 705 at 20 minutes.

28
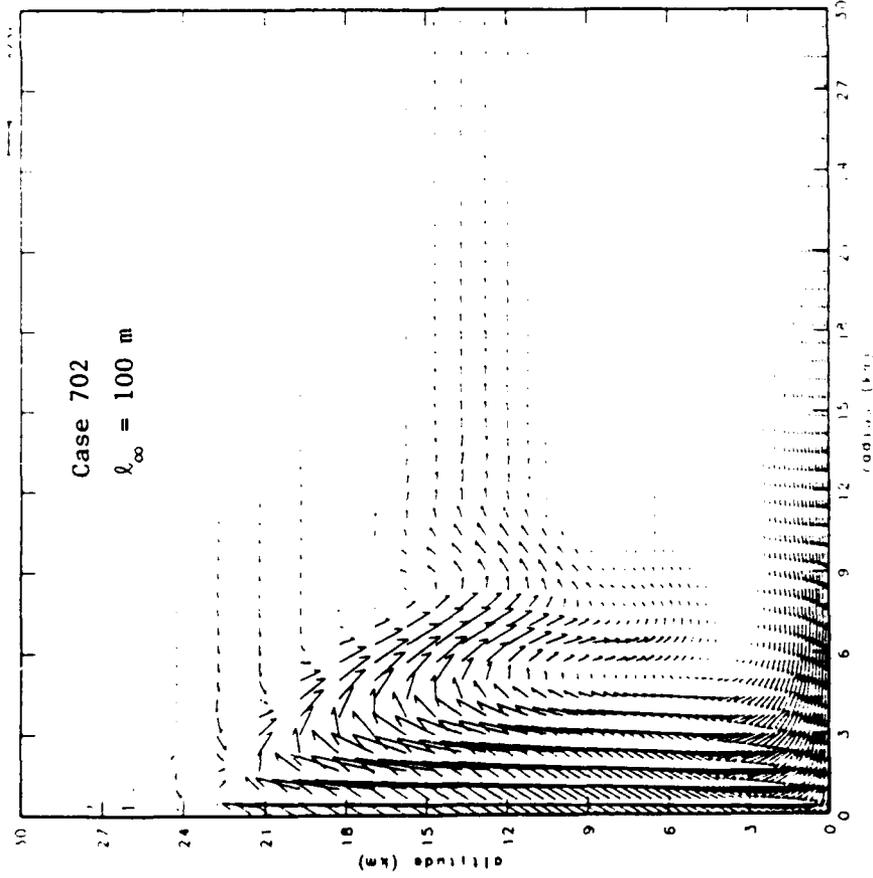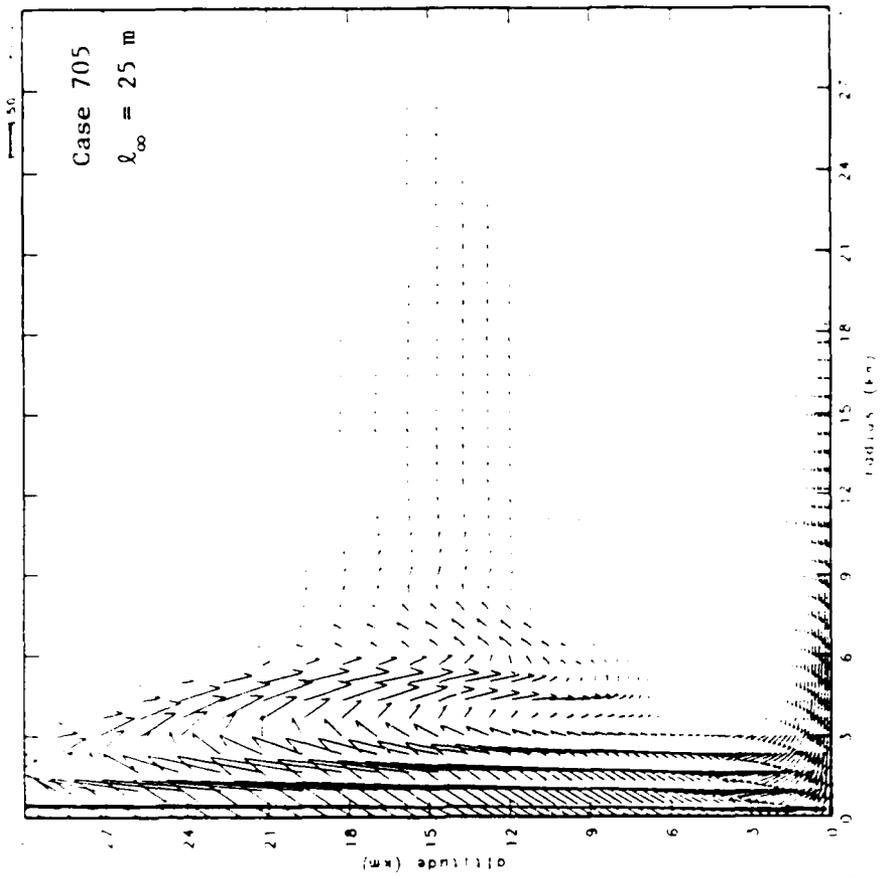
Figure 14c. Velocity vector plots for Cases 702 and 705 at 30 minutes.

Case 705

$\ell_\infty = 25$ m

Case 702

$\ell_\infty = 100$ m
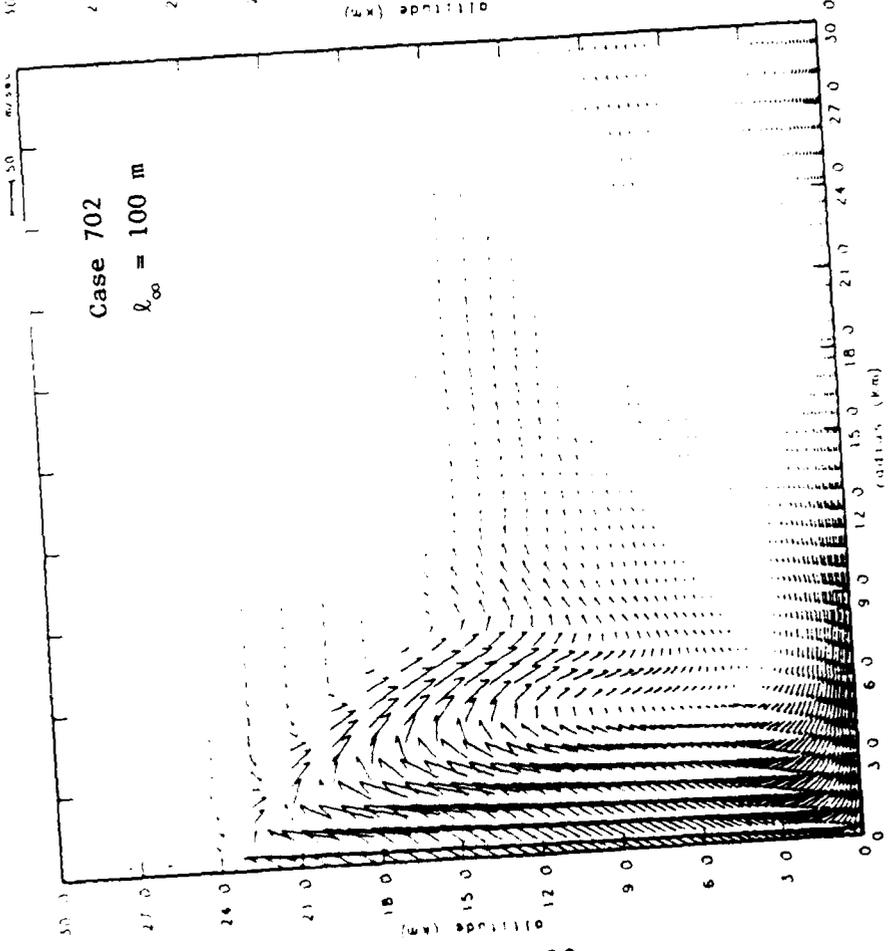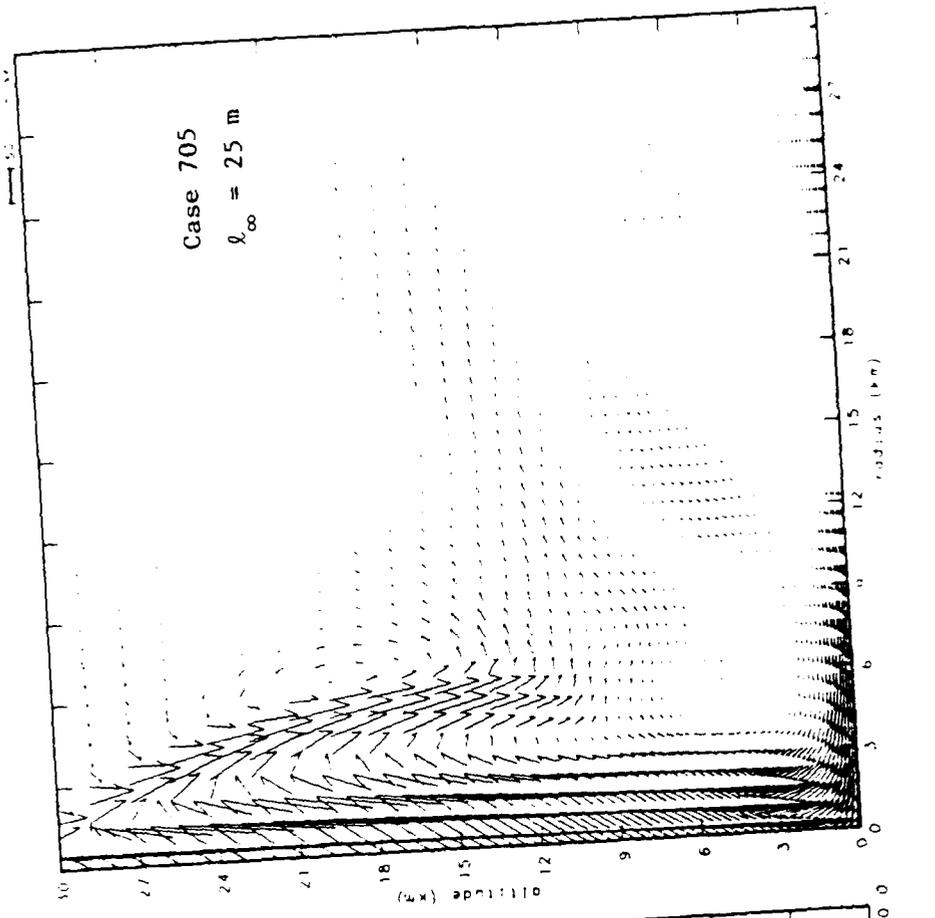
Figure 14d. Velocity vector plots for Cases 702 and 705 at 45 minutes.

30
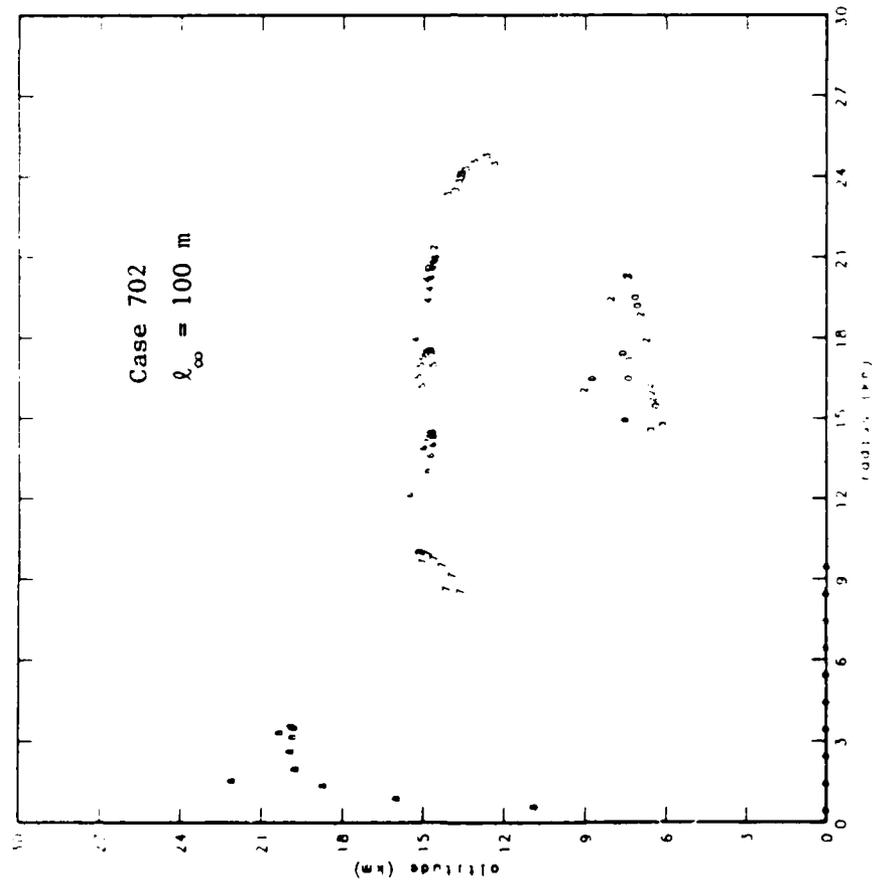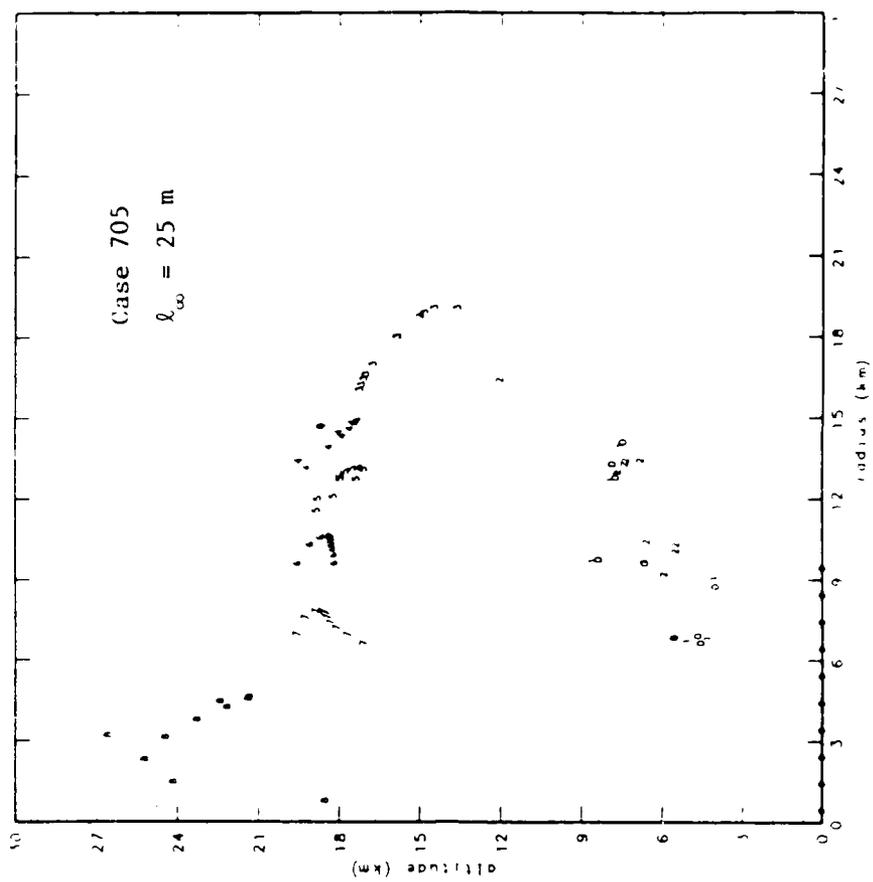
Figure 15. Tracer particles at 45 minutes for Cases 702 and 705.

31

WHICH TURBULENCE FORMULATION IS BEST?

For boundary layers we can use

$$\ell_\infty = 2\lambda \; \frac{\int_0^\infty qz \; dz}{\int_0^\infty q \, dz}$$

where $\lambda \approx 0.1$
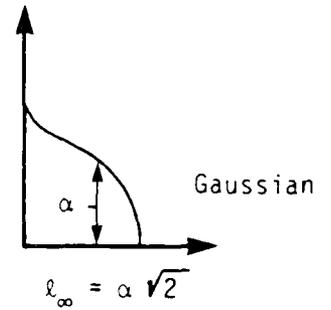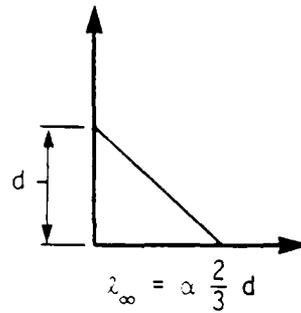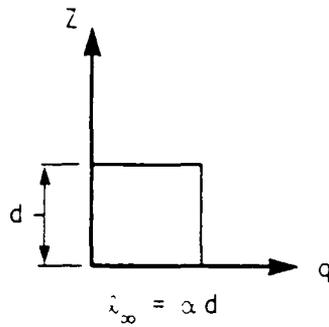
Case	$\pm Z_0$	ℓ_∞	Δ	0.1Δ	ℓ_∞/Δ	Max T'
502	100 m	–	300 m	30 m	–	600 - 1000 K
705	100	25	600	60	1/24	550
702	100	100	800	80	1/8	440
601	1000	–	1100	110	–	350

* Δ is height of +25 K T' contour at 5 km radius.

Figure 16. Relationship of turbulent mixing length to boundary layer depth.

32

Since Case 702 had a value of ℓ_∞/Δ which lies between 1/10 and 1/7, it would appear to be the most realistic of the simulations discussed so far. The table in Fig. 16 shows that the boundary layer depth for this case (800 m) was closer to that for Case 601 (1100 m) than to Case 502 (300 m); the plume for Case 702, which approached a steady state at moderate altitude, also resembles Case 601's plume (compare the left-hand plots in Figs. 14c-d with Figs. 7a-b). These comparisons show that the effects of parameterized turbulence in a finely-zoned grid are similar to the enhanced mixing which results from the use of a coarse grid, and indicate that of the inviscid cases, the 600-series was probably the more realistic.

The Meteotron Simulation

In order to validate our model and methodology, the DICE code was used to simulate a 600-megawatt test fire conducted at the Meteotron research facility in France on October 23, 1973 [6]. The Meteotron fire was produced by the array of oil burners shown in Fig. 17, which was simulated in our model by a uniform heat source of intensity 150 kW/m^2 and radius 36 m. The initial atmospheric temperature profile at the time of the burn, shown in Fig. 18, was characterized by a sharp inversion at an altitude of approximately 650 m.

For the large-area fires we have been discussing the radius of the burning area is larger than the e-folding depth of the atmosphere, and the aspect ratio (height to width) of the resulting plumes is of order unity. The radius of the Meteotron fire, however, is much smaller than atmospheric length scales, and consequently we expect the aspect ratio of the resulting plume to be much greater than for the firestorm cases. In this situation turbulent entrainment into the region of the plume column has a greater effect on the buoyancy than entrainment in the inflow layer. We therefore took the natural length scale for the Meteotron plume to be 72 m, the width of the burning region,

33

RADIUS = 36 m

48 BURNERS ——— 49 BURNERS

OIL DELIVERY PIPES

NORTH

10 m
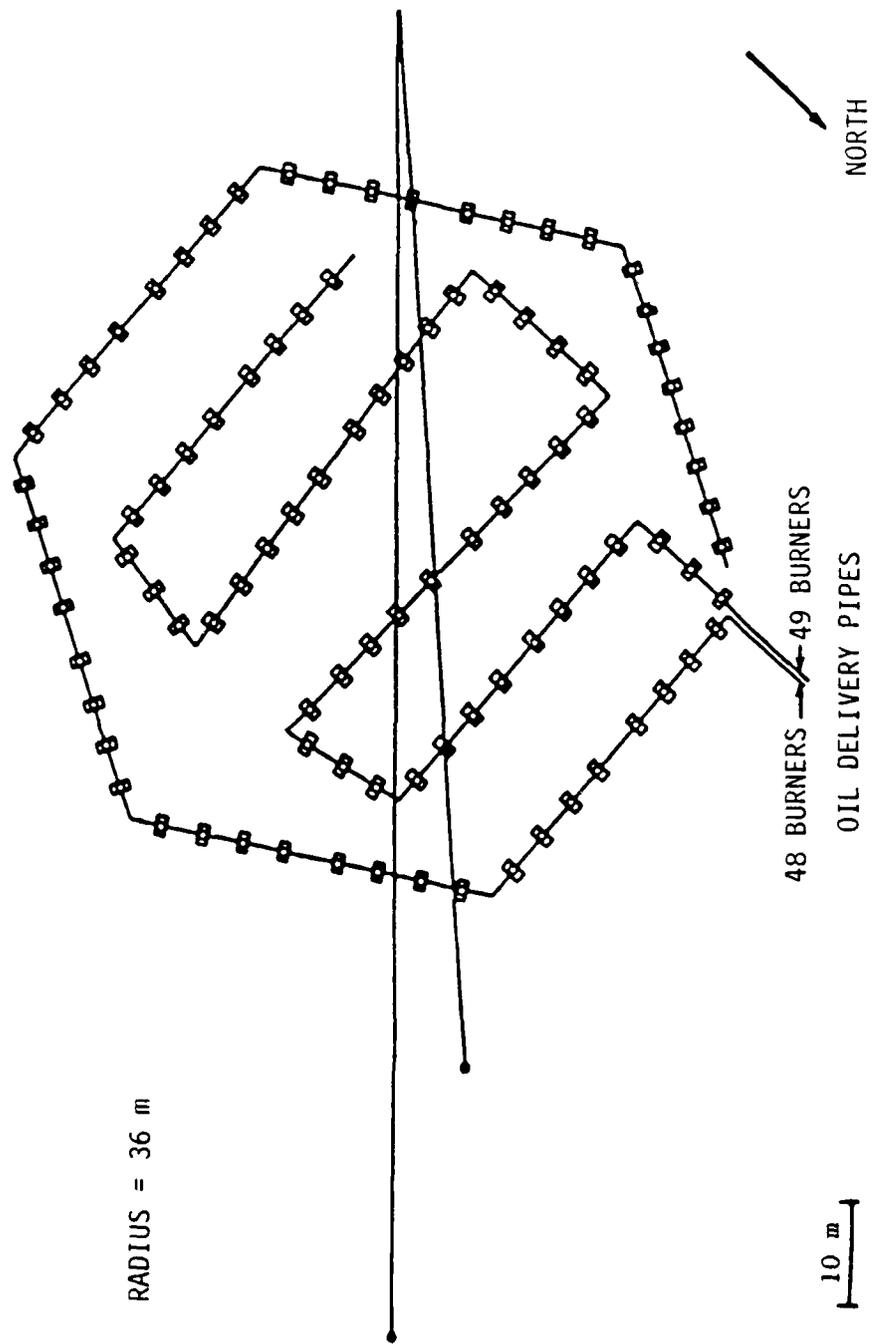
Figure 17. The Meteotron burner array.
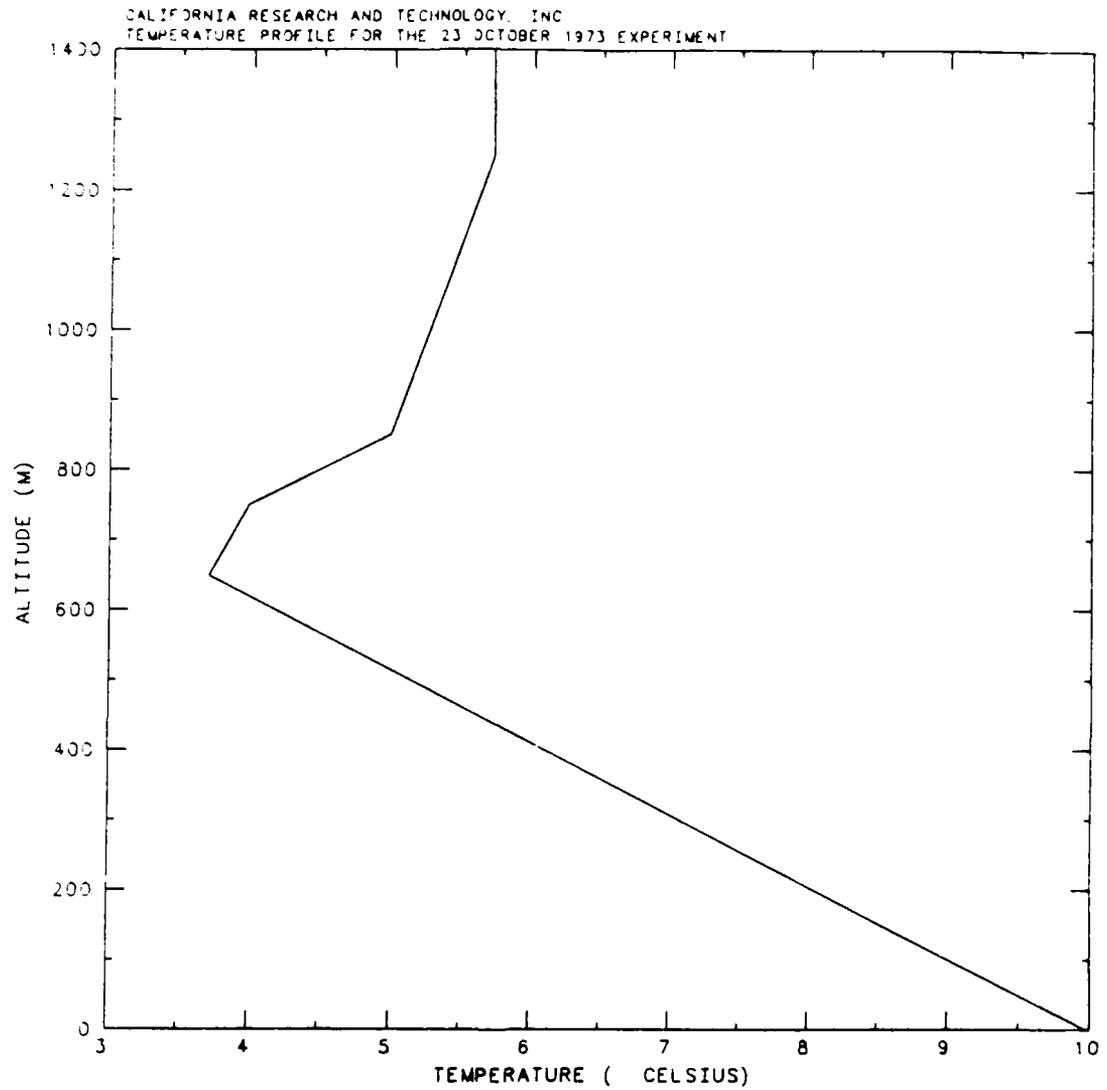
Figure 18. Atmospheric temperature profile for the Meteotron experiment.

and the asymptotic length scale l_∞ was taken to be 8 m, a value which lies between 1/10 and 1/7 of the natural length scale.

Comparisons between the simulated and experimental Meteotron plumes revealed the following points:

(1) During the course of the October 23 experiment, the burners were run for 10 minutes, with a "plume steady state resulting after 5 minutes; no further increase of the top plume was visible" [6]. For comparison, the development of the model plume can be most quickly visualized in Fig. 19, which shows the heights reached by tracers released at one minute intervals from the computational cell nearest to the center of the fire. From this figure it is evident that the model plume reached its maximum altitude between five and six minutes into the run, in agreement with the experiment.

(2) The top plume altitude for the experiment was reported to be 1260 meters, while the maximum altitude of the plume axis was given as 1050 meters [6]; the difference between these two heights is due to the inclination of the axis of the experimental plume to the vertical, and may be regarded as a rough measure of "experimental error." The two reported heights have been plotted with solid horizontal lines in Fig. 19, where it can be seen that the model plume top height was well within the experimental range. Note that both the experimental and model plumes penetrated the inversion and rose a considerable distance into the overlying stable layer.

(3) Fig. 20 shows streamlines of the simulated steady-state flow field (velocity is parallel to the streamlines), with observations of the visible boundary of the experimental smoke plume indicated by black circles. While turbulent diffusion within the plume causes the smoke to spread laterally, horizontal inflow at the edges of the plume confines the smoke to the area of upward motion. The approximate agreement between the boundary

36
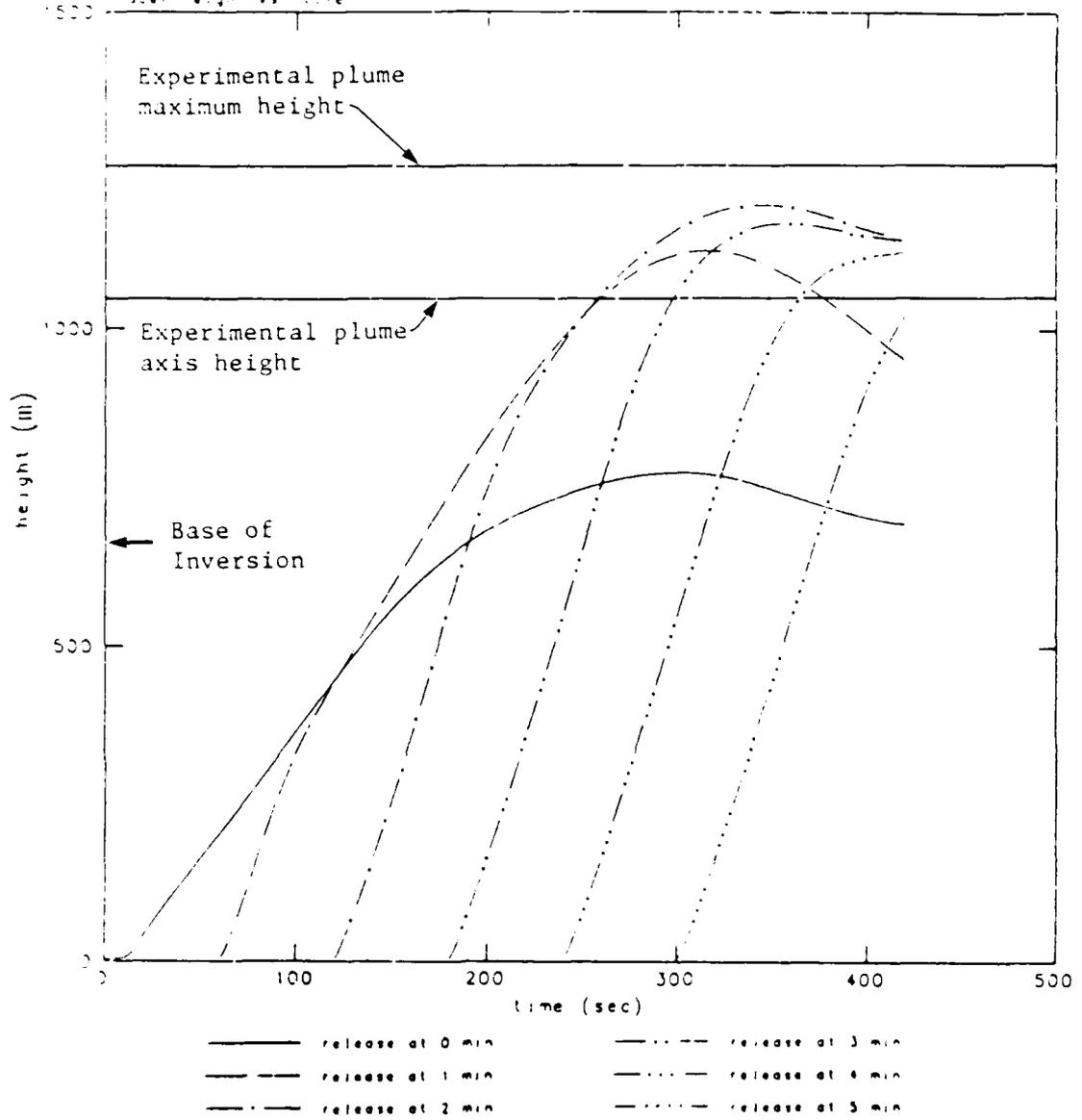
Figure 19. Height reached by tracers released from the computational cell nearest to the center of the fire for the Meteotron simulation. Solid horizontal lines show experimental plume top and plume axis heights.

37
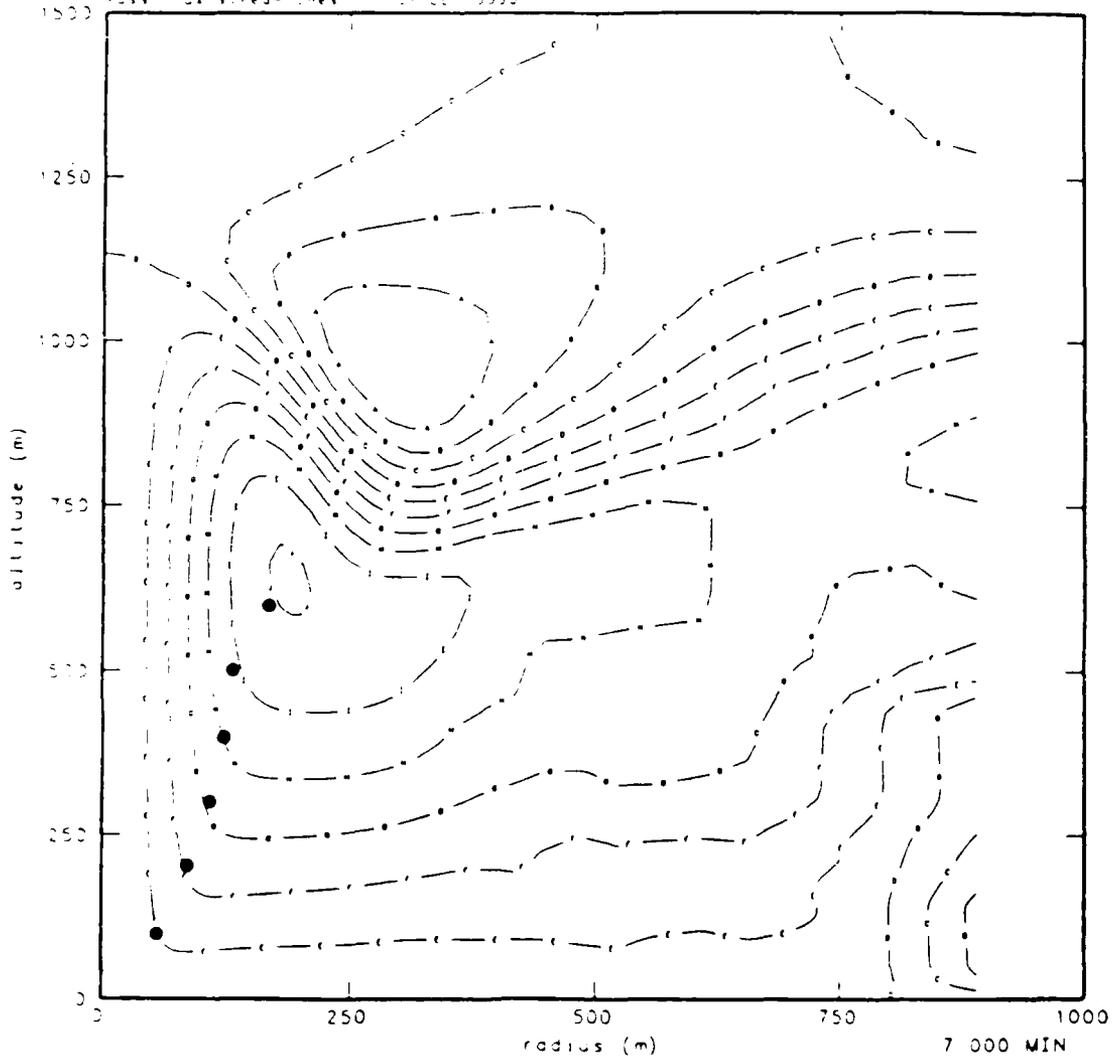
Figure 20.   Mass flux streamlines at 7 minutes for the Meteotron run.
Black circles show boundary of observed smoke plume.

of the observed smoke plume and the edge of the simulated inflow area indicates that the width of plume has been correctly predicted.

(4) The averaged plume over-temperature for eleven Meteotron experiments is shown as a function of height by the solid line in Fig. 21, and predicted over-temperatures for the October 23 simulation at one-half the observed plume radius are indicated by black squares. In view of the uncertainties involved in selecting a single representative plume temperature at each level, good agreement with the data is indicated.

These comparisons with the observed data show that the DICE simulation accurately reproduced the dynamics of the October 23 Meteotron burn. Due to the difference in aspect ratios, physical quantities (e.g., mixing lengths) cannot be scaled directly from this case to the firestorm cases. In spite of this difference, however, a consistent line of physical reasoning led to the selection of a turbulent length scale which enabled us to accurately calculate the stabilization height of the plume (see Fig. 19). Since this experiment involved the penetration of a thermal plume into an overlying stable layer, the success of the Meteotron simulation indicates that our model is capable of correctly simulating the penetration of a firestorm plume into the stable layers of the stratosphere.

The Effects of Swirl

Some investigators, citing anecdotal evidence from World War II, have maintained that rotating flow is an essential feature of the firestorm phenomenon (e.g., [7]). Others have disputed this, and have claimed that it is unlikely that large-area fires could generate significant rotational velocities [8]. In order to investigate this problem, the DICE code has been extended to include a tangential velocity component; axial
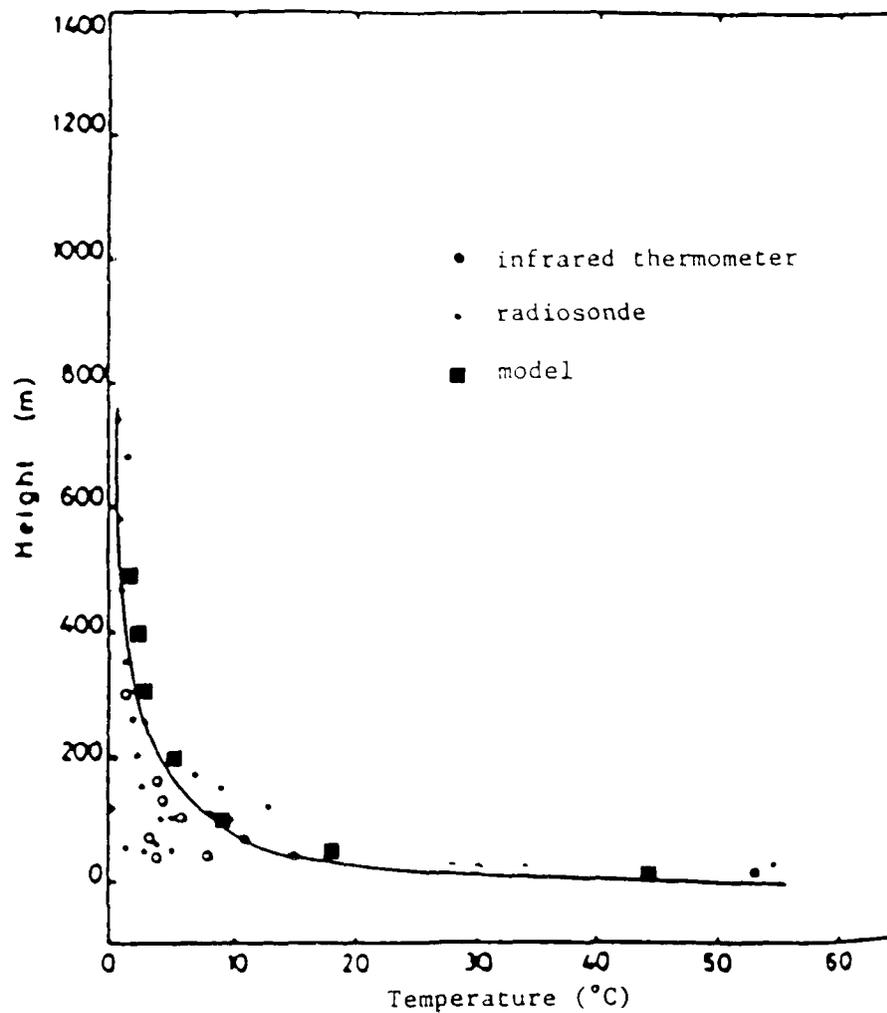
Figure 21. Solid line: Average plume over-temperatures
for 11 Meteotron experiments. Black squares:
Model over-temperatures calculated at one-half
the observed plume radius.

symmetry has been preserved, however, and all quantities are still functions of time, radius, and height only.

Case 841 was run with the extended version of the code, using the same parameters and turbulence sub-model as Case 702 (see Table 2). The initial swirl velocity distribution for this case was given by

$$w = 2\hat{w} \frac{\hat{x}}{1+\hat{x}^3} , \qquad (6)$$

where $\hat{x} = x / 10$ km, and $\hat{w}$ was taken to be 10 m/sec. The profile of the initial swirl velocity at the surface is shown in Fig. 22; in the free atmosphere, the initial swirl velocity decreases linearly with height from its surface value to zero near the tropopause.

The following conclusions were drawn from the swirl run:

(1) By the time the inflow layer is fully established at 30 minutes, maximum swirl velocities of over 200 m/sec are found in the lower layer near the axis (see Fig. 23c, which shows a contour plot of the swirl speed at 30 minutes into the run). These speeds are consistent with the conservation of angular momentum, since a ring of air with an initial tangential velocity of 10 m/sec at 10 km radius would "spin up" to a speed of about 300 m/sec at a radial distance of 0.33 km (where the innermost velocity gridpoint is located), provided no stresses are acting. While the model has no surface stresses, turbulent stresses from the overlying air limit the peak swirl speeds in the inflow layer to about 70% of the maximum possible value.

(2) Theoretical considerations lead us to believe that "in a nonrotating convective cell, the vertical velocity would overshoot its equilibrium altitude...in contrast, the swirling

41
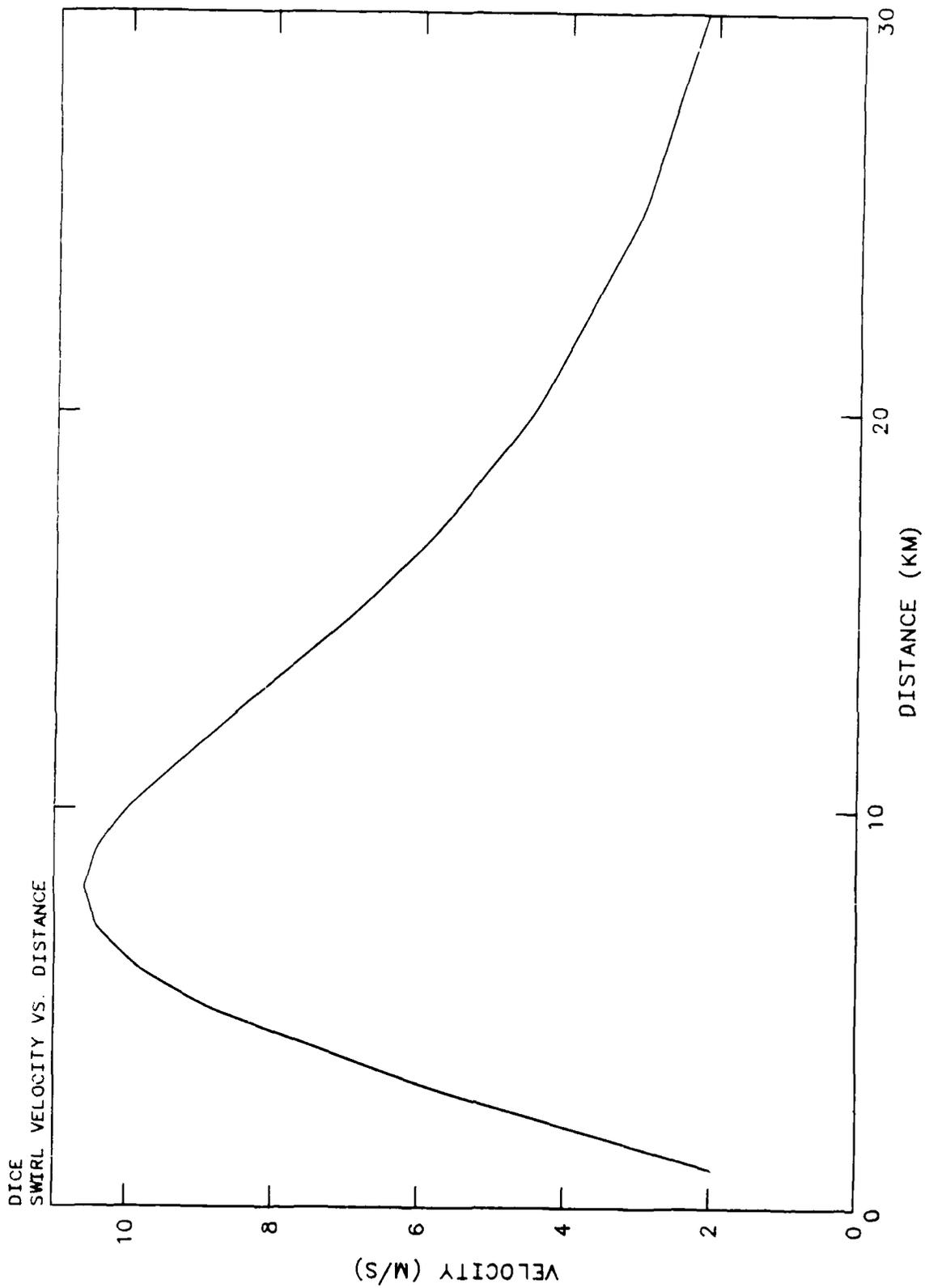
Figure 22. Initial prescribed swirl velocity at the surface for Case 841.

42
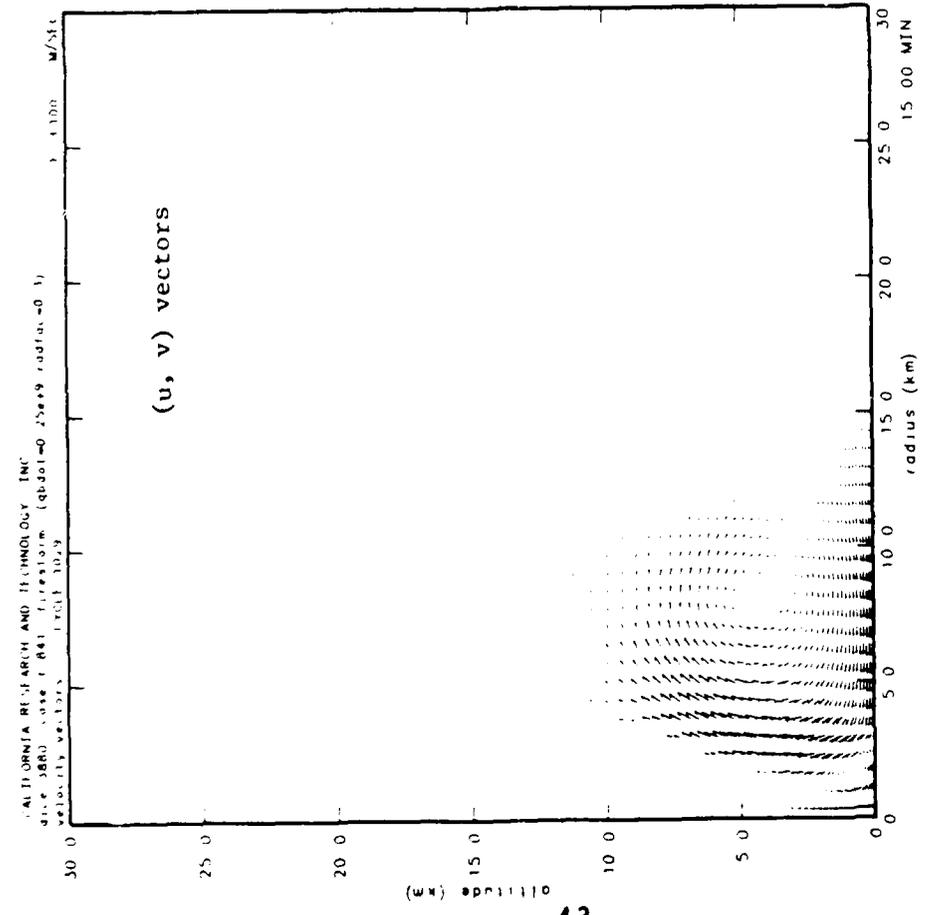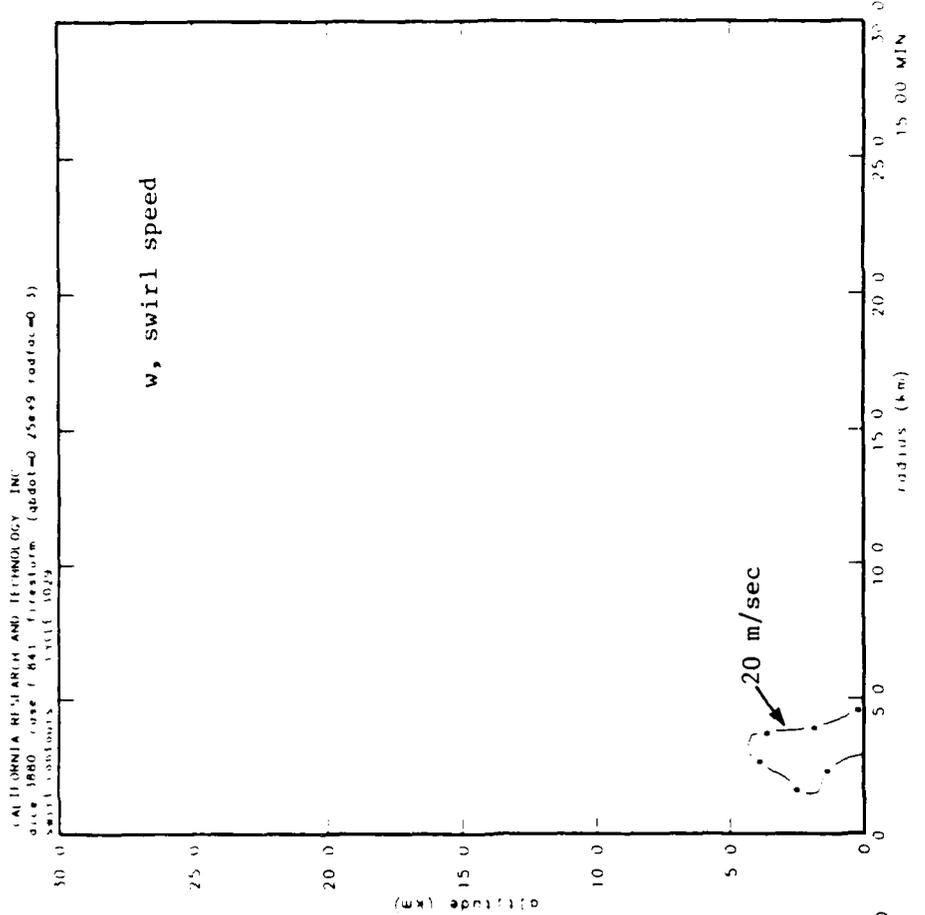
Figure 23a.   Non-swirl velocity vectors and contours of swirl
speed for Case 841 at 15 minutes.
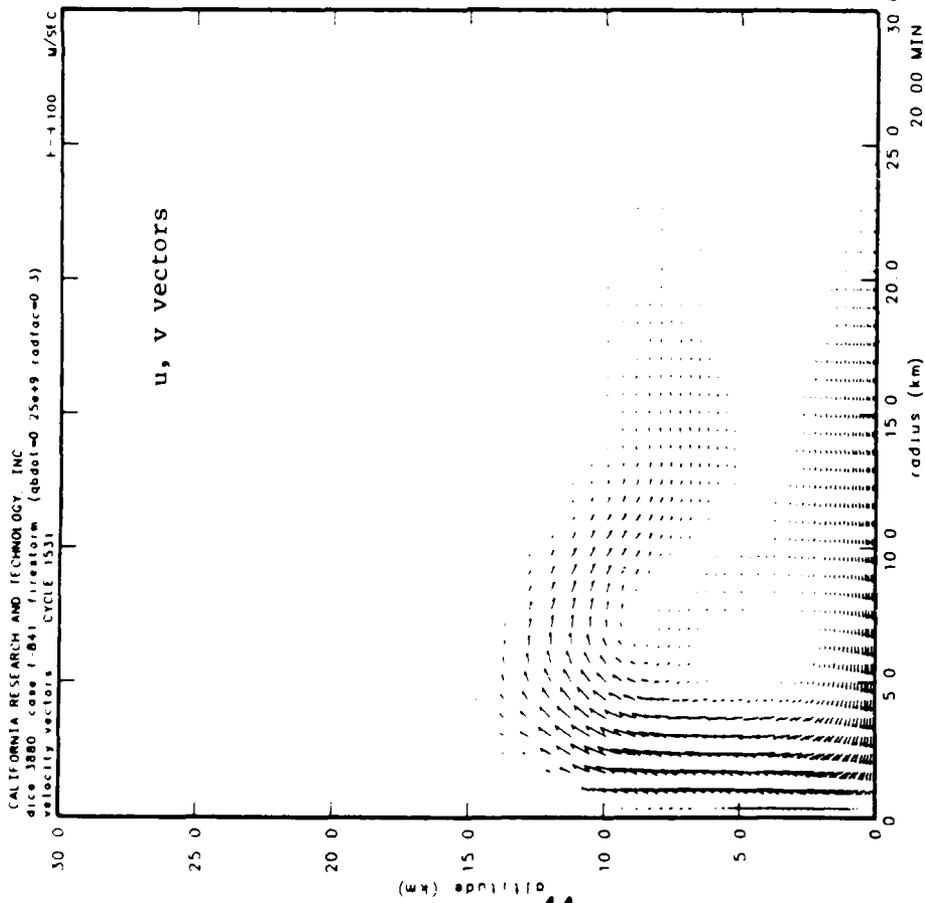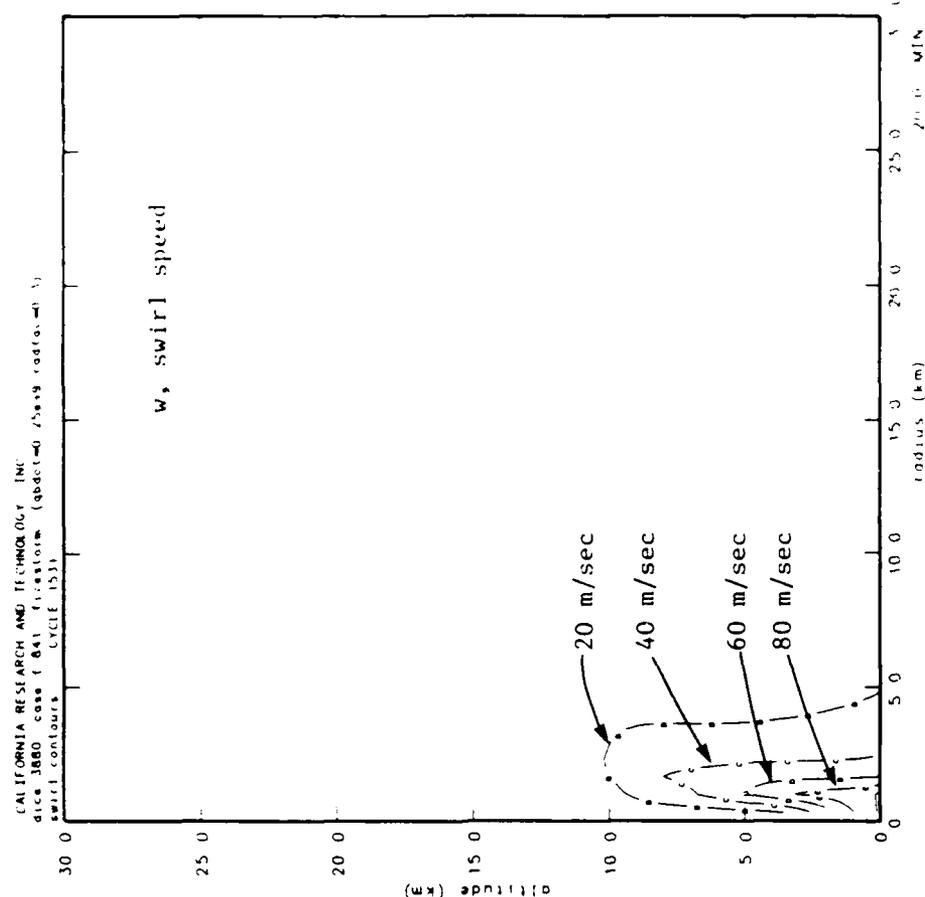
Figure 23b. Non-swirl velocity vectors and contours of swirl
speed for Case 841 at 20 minutes.
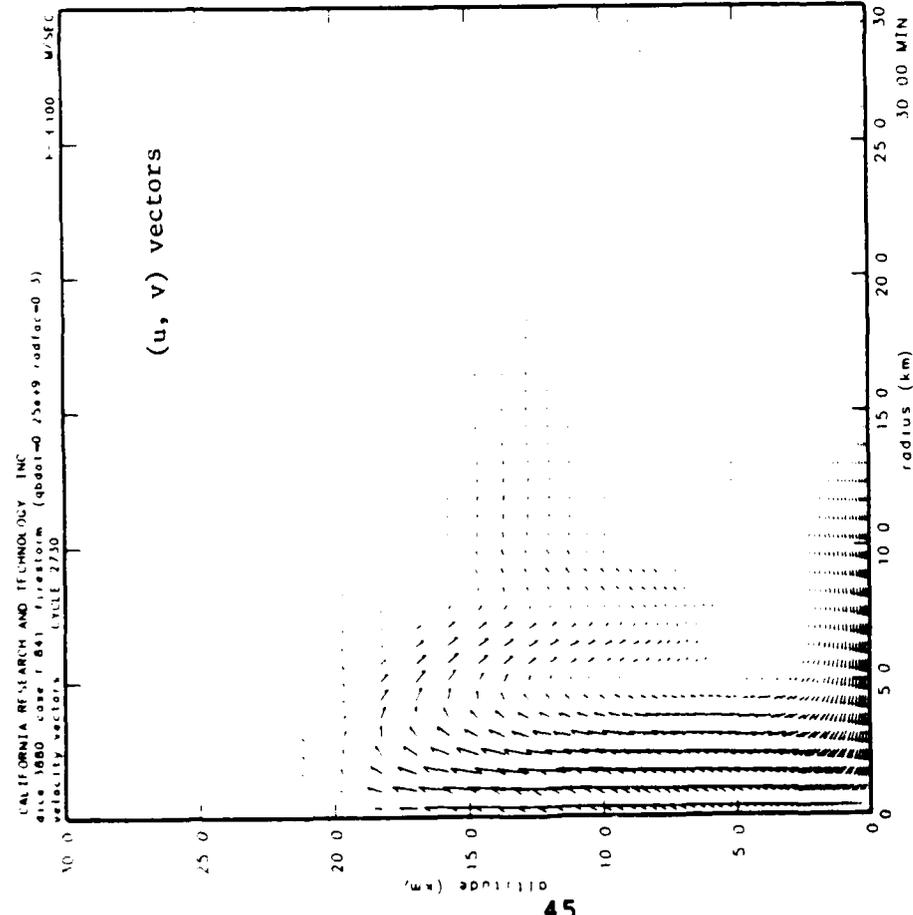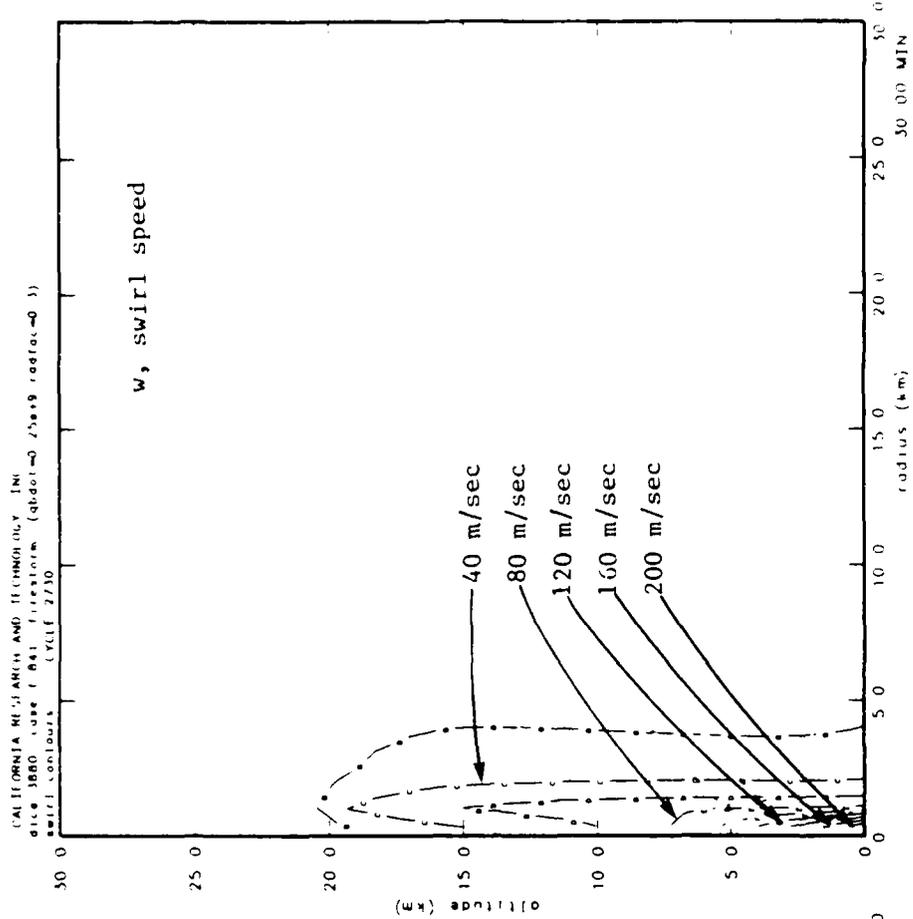
Figure 23c. Non-swirl velocity vectors and contours of swirl speed for Case 841 at 30 minutes.

45
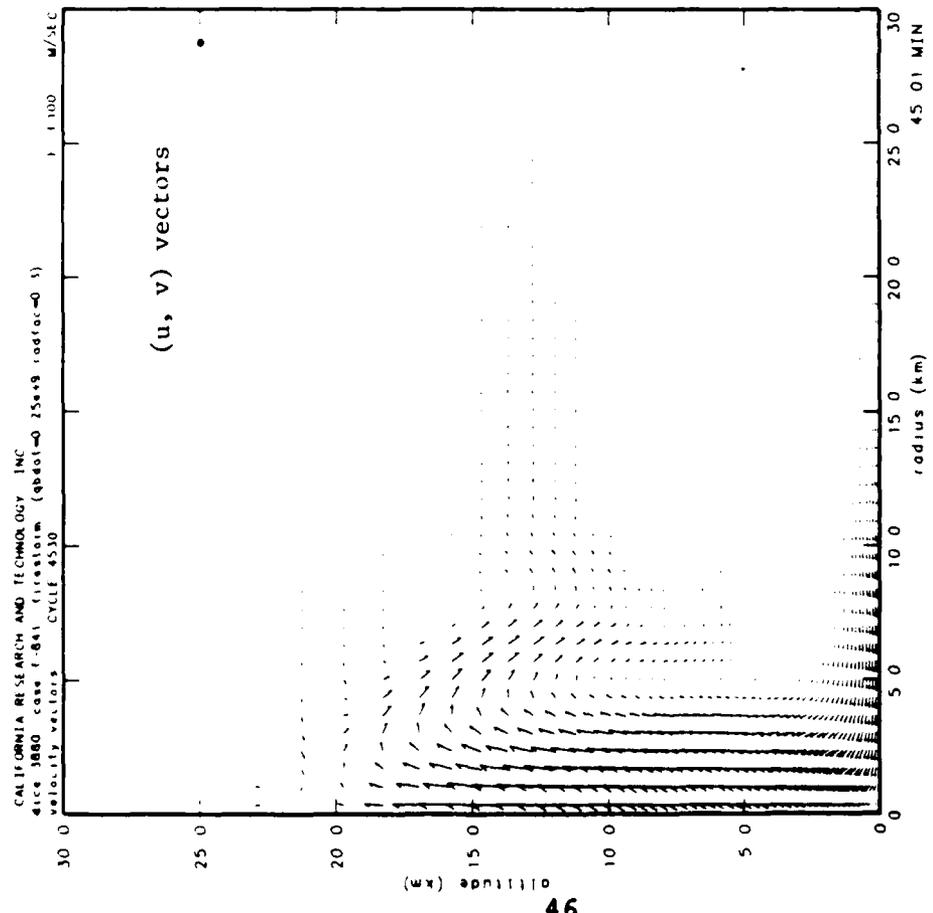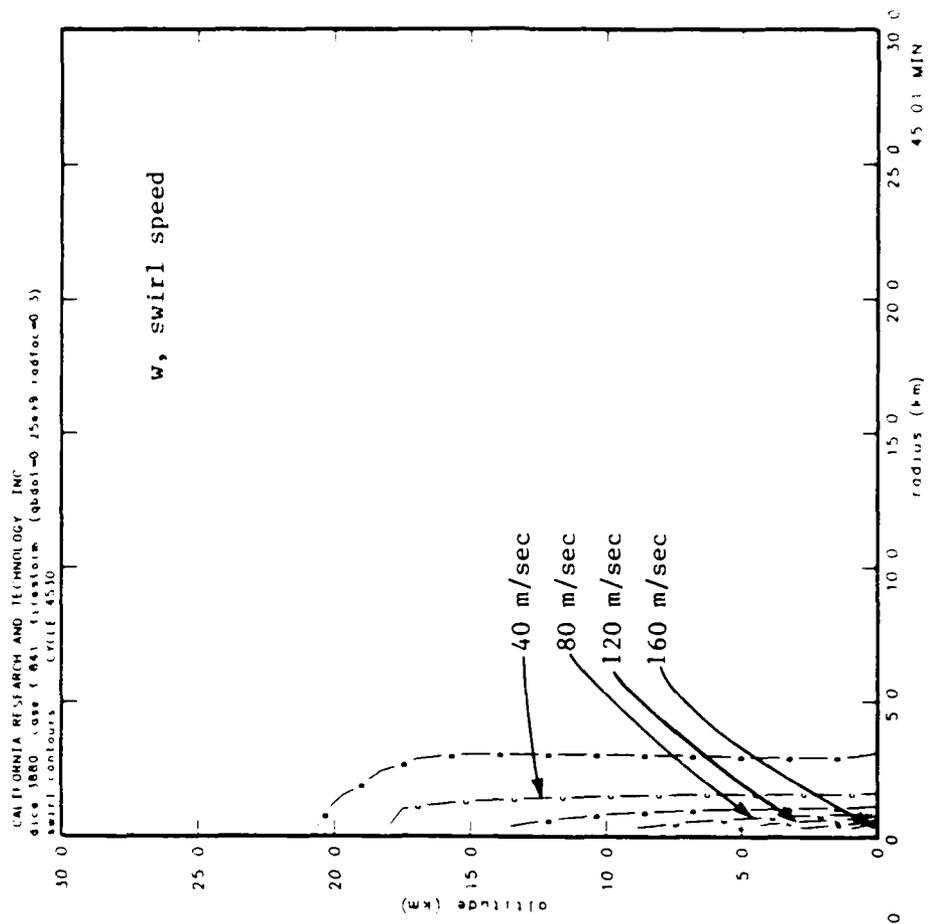
Figure 23d. Non-swirl velocity vectors and contours of swirl speed for Case 841 at 45 minutes.

updraft will have an adverse pressure gradient...which not only
blocks the overshoot, but almost certainly forces a downdraft
along the axis" ([9], p. 138). For our baseline non-rotating
case (702), the plume shows considerable overshoot by 20 minutes
(see Fig. 14b); for the rotating case (841), a plot of the non-
swirl velocity component at 20 minutes (see Fig. 23b) shows that
the rise of the plume has been substantially blocked, and that an
area of negative vertical velocity has indeed formed along the
axis. Although the swirling plume does penetrate into the
stratosphere at later times (see Figs. 23c-d), the plume heights
remain about 3 km lower than the corresponding heights for Case
702 (compare with Figs. 14c-d).

The results of Case 841 show that large rotational
velocities may develop in the interior of a 10-km radius fire,
given an initial ambient swirl of 10 m/sec at the fire edge, and
that the effect of the swirl is to delay plume rise and lower the
stabilization height somewhat. Interaction between the swirl
velocity field and the turbulence was not considered in this
case, however, and it is possible that the swirl may act to
suppress turbulence, as a stable density stratification does. As
was shown by the comparison between Cases 702 and 705 (see
Figure 14), this would tend to intensify the plume.

In one-dimensional problems where swirl is the only source
or sink of turbulent kinetic energy (TKE), a diagnostic equation
for the TKE may be derived in terms of the curvature Richardson
number R_c, which is a function of the swirl velocity
profile [10]. The effect of curvature on the turbulence is
indicated by the stability function $S_c(R_c)$, shown in Fig. 24.
For negative values of S_c the rate of destruction of TKE by the
swirl velocity field exceeds the rate of production, and the
turbulence is extinguished.
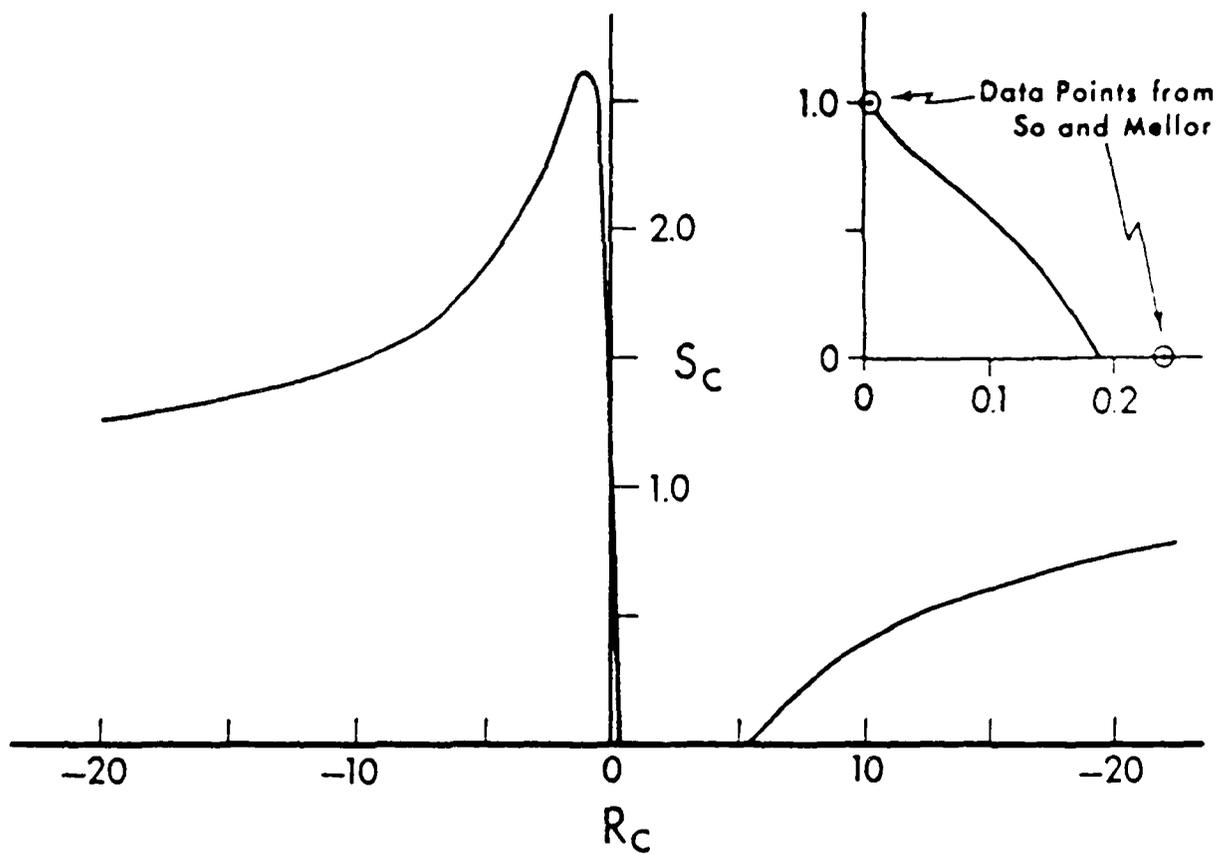
Figure 24. Dependence of the stability function on the
curvature Richardson number. Taken from [10].

In 3-dimensional cases where buoyancy and shear generate additional TKE, swirl may still exert a damping effect on the turbulence or extinguish it completely, depending on the relative magnitudes of the source and sink terms in the TKE budget equation. Unfortunately this equation is too complicated to be solved diagnostically for the TKE, and to adequately treat the general case, it becomes necessary to include separate predictive equations in the model for all of the components of the turbulent stress tensor, as well as for the turbulent heat fluxes.

A model developed by the Aeronautical Research Associates of Princeton, Inc. (ARAP) currently has this capability [9]. In a recent study of tornado dynamics, two versions of the ARAP code were used: one employed a diagnostic turbulence sub-model similar to that developed for the DICE code (which omits the effect of curvature on turbulence), and another used the fully predictive sub-model described above (which includes the effects of curvature on the turbulence). Non-dimensional plots of the turbulent eddy viscosity field produced by the diagnostic and predictive turbulence models are shown in Figs. 25a and 25b, respectively. Near the surface the turbulence profiles are similar, but at higher altitudes the predictive turbulence model produces much less eddy viscosity, indicating that rotational flow can have a damping effect on turbulence above the boundary layer.

While the DICE code is not yet capable of explicitly calculating the effects of swirl on turbulence, the likely effects can be mimicked by artificially reducing the turbulent mixing length (and hence the turbulence) in the region above the boundary layer. Case 846 was run with the same parameters as Case 702 (see Table 2), except that the turbulent mixing length was reduced from 100 m to 25 m between the altitudes of 0.5 km and 1.0 km (see Fig. 26). The velocity fields from Case 846 at 20 and 30 minutes are shown in Figs. 27a-b. A comparison with the corresponding plots for Case 702 (see Figs. 14b-c) shows that

49

Non-dimensional eddy viscosity: full turbulence model

Figure 25b. Eddy viscosity field produced in ARAP tornado simulation using full turbulence sub-model. Taken from Lewellan and Sheng (1980). Units are non-dimensional.

Non-dimensional eddy viscosity: simplified turbulence model

Figure 25a. Eddy viscosity field produced in ARAP tornado simulation using simplified turbulence sub-model. Taken from Lewellan and Sheng (1980). Units are non-dimensional.
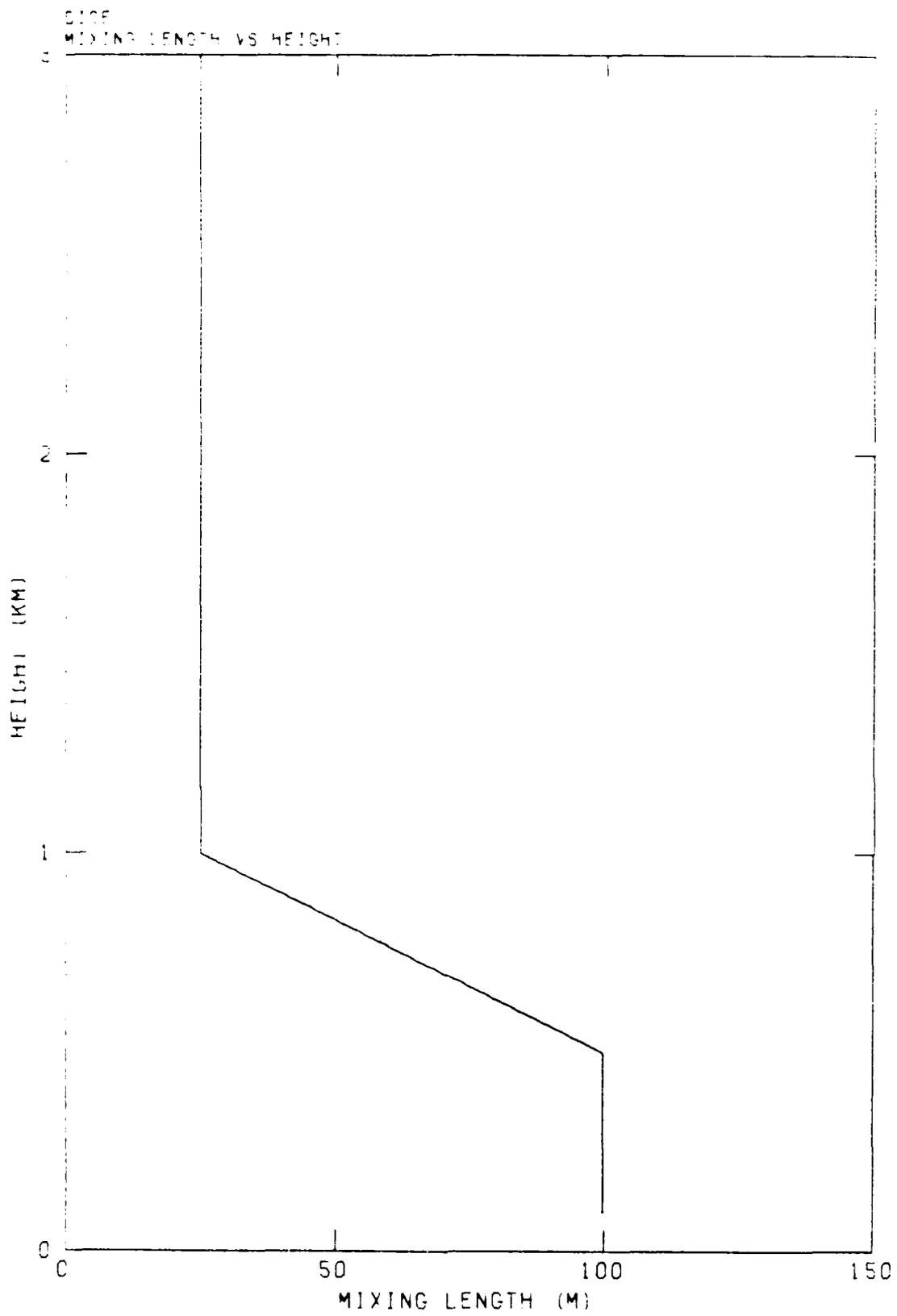
Figure 26. Specified value of ℓ_∞ for Case 846.

51
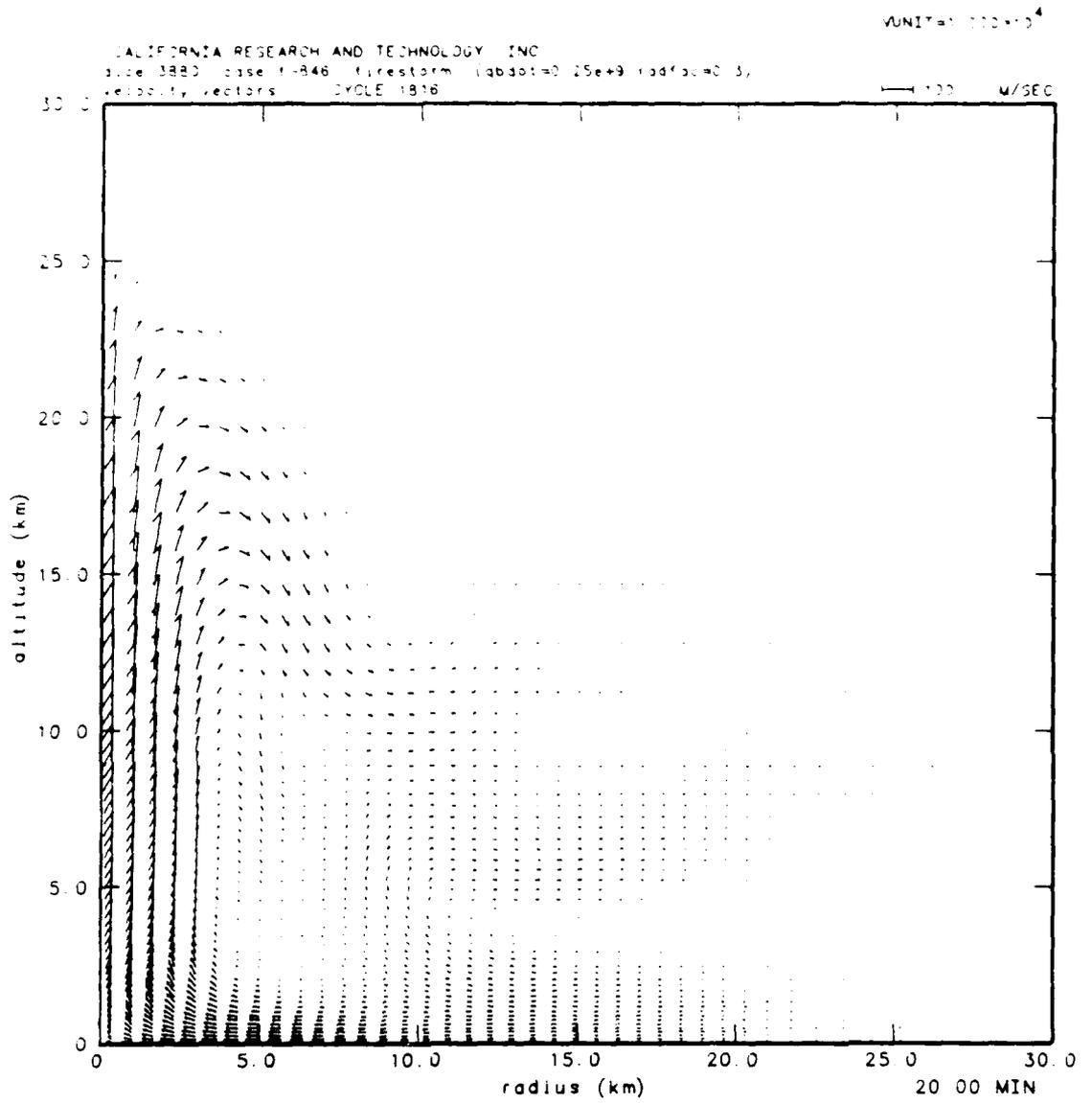
Figure 27a.   Velocity vector plot for Case 846 at 20 minutes.
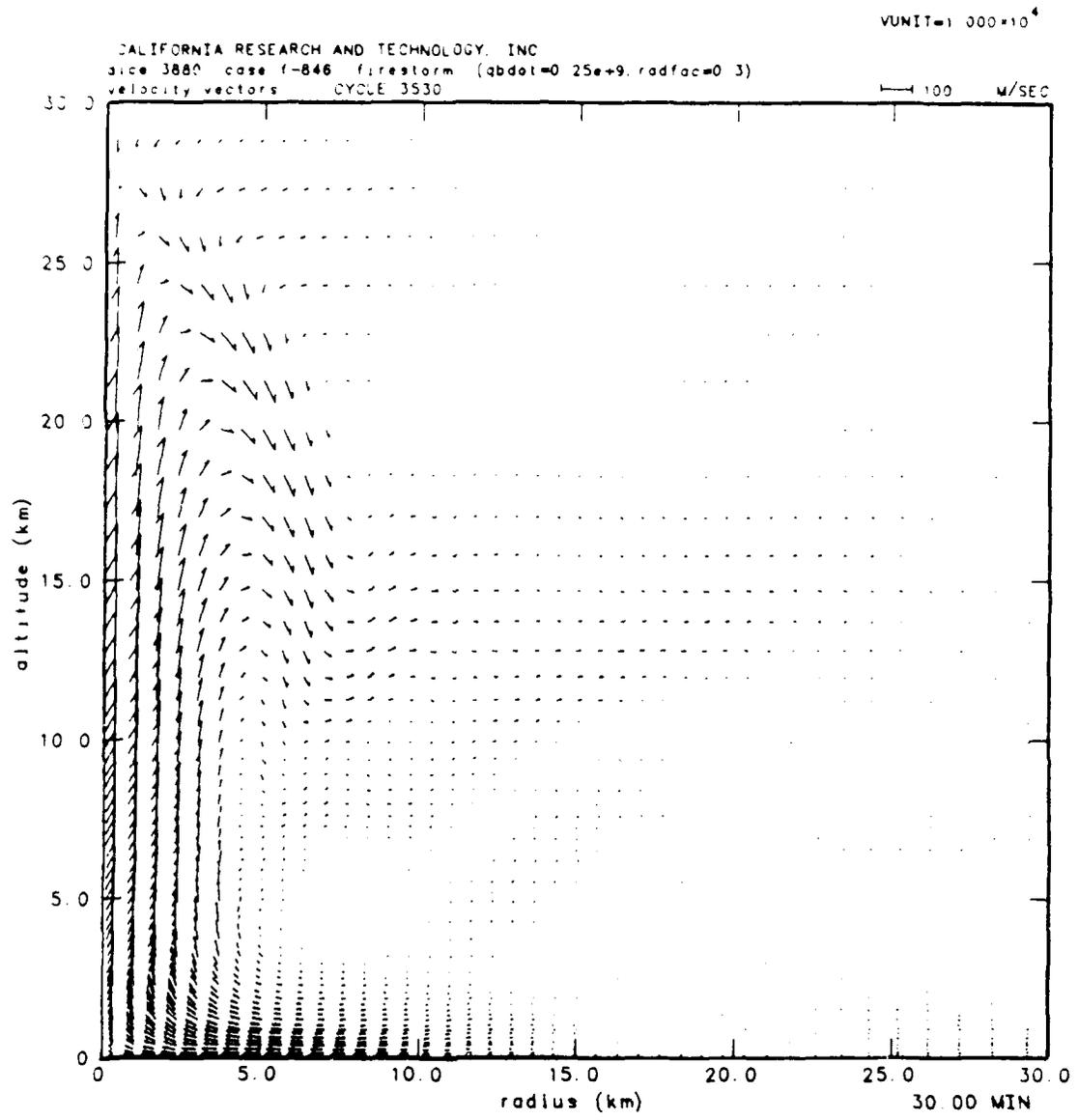
Figure 27b. Velocity vector plot for Case 846 at 30 minutes.

decreasing the mixing length near the top of the boundary layer
from its value in Case 702 (100 m) to the value it had in
Case 705 (25 m) causes the plume to rise by about 3 km,
comparable to the decrease in plume height caused in Case 841 by
swirl which does not interact with turbulence.

When the turbulent mixing length is changed from 100 m to
25 m throughout the entire domain, a much greater increase in the
plume height is obtained, as we saw in the comparison between
Cases 702 and 705 (see Fig. 14). This confirms our earlier
observation that turbulent entrainment within the boundary layer
is the dominant effect of turbulence in large-area fires, and
indicates that if swirl is to have a significant effect on plume
stabilization heights, it must do so by suppressing turbulence
within the boundary layer. Although present indications are that
this effect would be small, the definitive resolution of this
question awaits the modification of the DICE code to predict the
full set of turbulent fluxes, or the application of a model which
already has that capability (such as the ARAP code) to the
firestorm problem.

1.4 CONCLUSIONS AND RECOMMENDATIONS.

The main conclusions which were reached in the course of
this study are as follows:

* Mixing plays a dominant role in the dynamics of the
  plumes generated by large-area fires. When the inviscid
  version of the code is run using the "fast" burning
  scenario and fine zoning (with a lower layer depth of
  0.1 km), high temperatures lead to the development of
  narrow, overshooting plumes and quasi-periodic solutions.
  When the combustion heating is "mixed" over a lower layer
  depth of 1.0 km in the corresponding coarse-zoned case,
  cooler temperatures lead to broader, less intense plumes
  and a quasi steady state solution.

54

- The effects of mixing may be incorporated in a fine-zoned calculation through the use of parameterized turbulence. We used a turbulence sub-model based on the turbulent kinetic energy equation, and calibrated the master turbulent length scale through a relation between the turbulent and natural length scales proposed by Yamada and Mellor [5]. The baseline turbulent case (702) produced a broad, quasi-steady state plume similar to that obtained from the coarse-zoned inviscid case.

- The turbulent version of the model was validated by simulating the plume from an experimental fire conducted at the Meteotron research facility in France on October 23, 1973. Although the aspect ratio of the Meteotron plume was greater than those of the firestorm plumes, a consistent line of physical reasoning led to the selection of a turbulent length scale which enabled us to accurately calculate the stabilization height of the plume. Since this experiment involved the penetration of a thermal plume into an overlying stable layer, the successful simulation of the Meteotron plume indicates that the DICE code is capable of correctly simulating the penetration of a firestorm plume into the stable layers of the stratosphere.

- The validation of the turbulent model by the Meteotron simulation, and the similarity between the results of the baseline turbulent case and the single-phase coarse-zoned inviscid case (601), indicate that the soot and ice/water clouds generated in the multiphase coarse-zoned Cases 603-606 are probably realistic. These cases show that the stabilization heights and radial extents of the particulate clouds generated by large-area fires in a dry, resting atmosphere are quite sensitive to the size and burning rate of the postulated fire.

- Latent heat released by condensing water vapor has a large effect on plume-rise, since this heating is usually concentrated at high altitudes near the core of the plume. When the ambient atmosphere is dry, latent heat released by water vapor formed from the burning fuel leads to the formation of secondary soot and ice/water clouds above the central regions of the primary particulate clouds. When the ambient atmosphere is given a moderate initial relative humidity, however, the effect of latent heat release is much more dramatic, with the plume from a 10-km "fast" burning fire exceeding an altitude of 30 km after 30 minutes.

- Swirl velocities in excess of 200 m/sec were obtained in the interior of a simulated 10-km radius fire, given an initial swirl velocity of 10 m/sec at the fire edge. These large velocities are consistent with the conservation of angular momentum, which holds approximately in the boundary layer of the model since surface stresses are absent and stresses from the overlying air are small. In this simulation, which made no allowance for the effects of swirl on turbulence, the main effects of swirl were to delay plume rise somewhat, and to lower the stabilization height of the plume by about 3 km.

- When the expected effects of swirl on turbulence were mimicked in a non-rotating version of the DICE code by artificially reducing the turbulent mixing length in the region above the boundary layer, the plume height was enhanced by only abou. 3 km, compared to a control case which used a constant mixing length. When the mixing length was reduced in the boundary layer as well, however, a much greater enhancement in plume rise was obtained. This confirms our conclusion that mixing in the inflow layer is the dominant effect of turbulence in

large-area fires, and indicates that if swirl is to dramatically enhance the stabilization height of the particulate clouds generated by large-area fires, it must do so by reducing the turbulence in the inflow layer.

Based on these conclusions, the following recommendations for further study are made:

- In order to accurately assess the potential of swirl to enhance plume-rise from a large-area fire, it will be necessary to perform a firestorm simulation which predicts the full set of turbulent fluxes, and hence accounts correctly for the effects of the swirl velocity field on turbulence. We therefore recommend that the swirl code developed by the Aeronautical Research Associates of Princeton, Inc. (ARAP), which already has this capability [9], be adapted to the firestorm problem and used to carry out such a study.

- The simulations presented in this report showed that persistent, high-velocity winds are generated in the inflow layer of a large-area fire, and it is likely that these winds will scour considerable quantities of debris from the surface, particularly in areas of heavy blast damage. Scoured material which is lofted in the plume may affect the distribution of ice/water particulates by serving as condensation nuclei, and may affect the dynamics of the plume through the associated latent heat release as well as mass loading and drag.

  The capability for predicting the input of debris from surface scouring, as well as its flow through the grid in discrete size groups which exchange heat and momentum with the air, has previously been implemented in the DICE code in connection with the study of nuclear burst phenomena. A new microphysics package has also recently been implemented

57

in DICE, which predicts one-parameter continuous size distributions for non-precipitating cloud water and ice hydrometeors as well as for rain, snow, and graupel/hail particulates in each computational cell at each time step. If sub-models for the agglomeration and scavenging of soot are added to these features, the DICE code will be capable of following the evolution of the soot/dust/ice/water cloud from a large-area fire in a fully interactive mode.

We therefore recommend that this enhanced multi-phase version of the DICE code be developed, and utilized in conjunction with a fine-zoned grid and parameterized turbulence, in order to provide more detailed and reliable estimates of the configuration and composition of the particulate clouds generated by large-area fires. By carrying out simulations for a variety of initial temperature and humidity profiles for periods of up to several hours after the start of the fire, considerable insight can be gained into the likely nature of post-attack environments, as well as the potential for mass fires to initiate the global climatic perturbations referred to as "nuclear winter."

SECTION 2

THE NUMERICAL MODEL

DICE (an acronym for Dirt Implicit Compressible-Fluid
Eulerian) is a multi-phase, axisymmetric numerical model based on
the compressible flow equations [3]. The grid spacing can vary
both horizontally and vertically, with each cell representing an
average over an annular region (see Fig. 1). Each cell contains
the pressure, density, and specific energy of the air, which are
related by the AFWL equation of state. Each cell also carries the
density and specific energy for up to nine additional groups, which
may be solid, liquid, or vapor (e.g., soot, ice/water particles,
and water vapor).

Thermal interactions occur in a computational cell because
there are (1) temperature differences between any of the soot-
water-air mixture species, and (2) because of material phase
changes. Liquid-vapor phase changes and the associated transfer of
latent heat are treated in a time-dependent fashion. For the
multiphase firestorm simulations discussed in this report all of
the ice/water particulates were assumed to have a diameter of
10 microns, and all particle groups were flowed with the same
velocity as the air.

DICE utilizes implicit finite differencing, which is
advantageous in many physical applications over the explicit finite
differencing technique more commonly used in wave propagation
analyses. In the implicit method, the integration time step is
inversely proportional to the maximum mass velocities, whereas in
the explicit method, this step is proportional to the reciprocal of
the maximum wave velocities. In those problems where wave
velocities are much larger than mass velocities, an implicit method
integrates over a given period of real time in a smaller number of
steps than is required in an explicit method.

59

The actual process of combustion is not modeled; instead, the heat released by the fire is added to the lowest layer of computational cells at a specified rate. The loss of heat due to thermal radiation at any location is proportional to $T^4 - T_{amb}^4$, with the constant of proportionality adjusted to make the total loss integrated over the domain equal to 30% of the rate of energy input from the fire.

SECTION 3

INVISCID FIRESTORM SIMULATIONS

3.1 OVERVIEW.

This section describes a series of numerical experiments
performed with an inviscid version of the code (see Table 1). The
results of these cases illustrate the effects of variations in the
burning rate, burning area, computational zoning, and multi-phase
physics on the predicted firestorm environments. The initial
temperature profile was taken from the U.S. Standard Atmosphere
(see Fig. 2), for which the tropopause height is 11 km. For Cases
301-606, the atmosphere was assumed to be dry, while for Case 608
the initial relative humidity was assumed to be 60% at the surface
and to decrease linearly with altitude to zero at 30 km. In Cases
301-601, massless tracer particles were released in the burning
area at regular intervals; these allow us to determine the region,
but not the concentration, of the lofted soot. In Cases 603-608,
5% of the mass burned is converted to soot and 50% to water vapor
(see Table 1), and the soot and water contents of the clouds are
calculated explicitly.

In a study of fatalities in World War II fires, Lommasson and
Keller [11] found that these fires fell into two broad classes (see
Fig. 28). Group fires had an average burning rate of approximately
62.5 kW/m^2, and were characterized by relatively low fatality rates
in the population at risk. Firestorms, which occurred less
frequently, had average burning rates of 250 kW/m^2, and were
characterized by much higher fatality rates in the population at
risk. In order to simulate these distinct types of fires, two
different time-varying burning rates were used (see Fig. 3). In
the "fast" ("slow") burning scenario, the burning rate rises
linearly from zero to a peak value of 250 kW/m^2 (62.5 kW/m^2) in
15 minutes (1 hour), maintains the peak rate for 30 minutes

61

$$\dot{q}_b = 0.25 \text{ MJ/m}^2/\text{sec}$$
$$= 610 \text{ BTU/mi}^2/\text{sec}$$

$$\dot{q}_b = 0.0625 \text{ MJ/m}^2/\text{sec}$$
$$= 153 \text{ BTU/mi}^2/\text{sec}$$

FIRESTORM
EVENTS

Heilbrann   Hamburg
Dresden
Darmstadt

GROUP
FIRES

Aomori
Barmen
Freiberg
Hiroshima   Fukui
Solingen   Friedrickshafen
Aachen   Ulm   Toyama   Chosi
Nagasaki   Fukuyama

Percent fatalities in Population at Risk

AVERAGE FIRE SEVERITY (Millions of BTU per sq. mile per second)
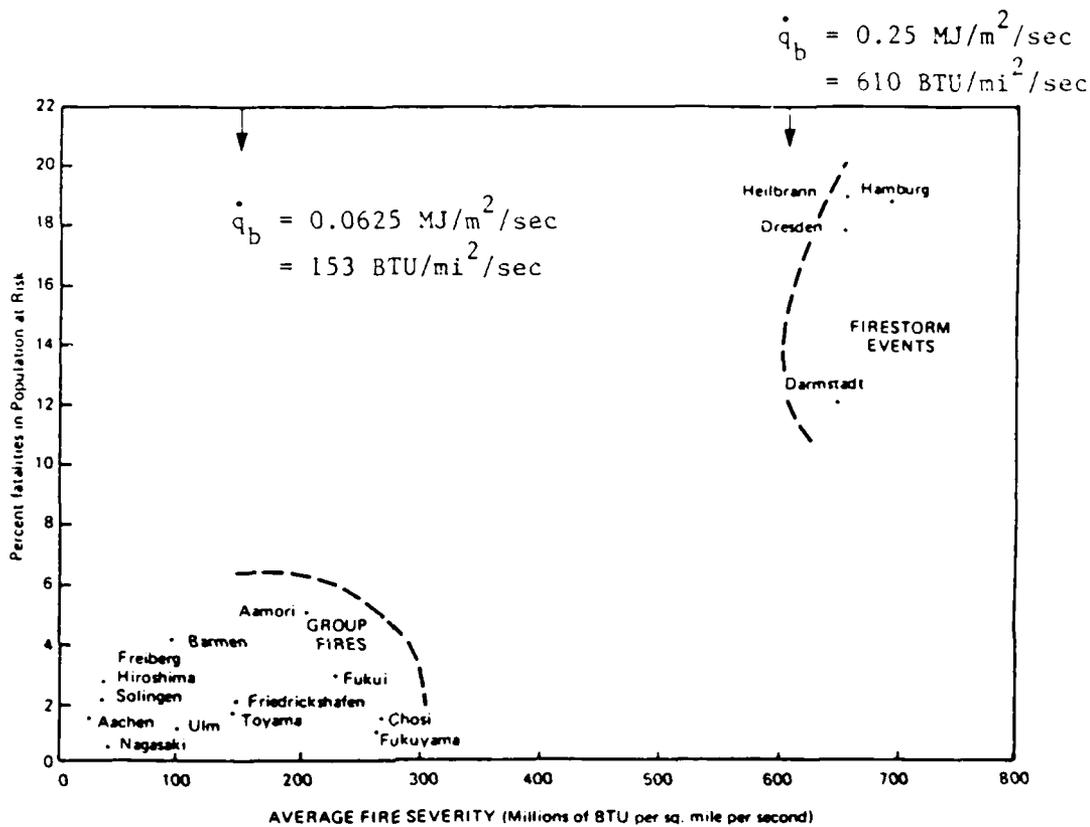
*Lommasson and Keller, A Macroscopic View of Fire Phenomenology and Mortality Predictions, Dikewood Corporation, DC-TN-1058-1, December 1966.

Figure 28. Fatalities in World War II fires.

(2 hours), and then decreases linearly back to zero in 15 minutes
(1 hour). Note that for both scenarios, the total heat input per
unit area integrated over the duration of the fire is the same.

The burn radius was taken to be 3, 10, or 30 km, with the
combustion energy added uniformly to the lowest layer of cells over
the entire burning area. Cases 301, 502, and 504 used a grid with
variable spacing and a lower layer thickness of 0.1 km, while in
the 600-series of cases, a uniform grid with 1 km spacing was used
(see Table 1). The radial and vertical boundaries of the grid were
placed at distances of 60 km and 40 km from the origin,
respectively, with continuum boundary conditions allowing for the
flow of air out of the computational domain or the advection of air
at ambient conditions into the domain.

3.2 FINE-ZONED CASES.

In Case 301, which used the "fast" burning scenario and a
lower layer thickness (where the combustion heating is added) of
0.1 km, temperatures in excess of 1200°K were generated (see
Fig. 29, which shows a time history of the temperature at three
locations within the boundary layer). The large buoyancy generated
by these temperatures led to the formation of an intense, jet-like
plume along the axis, which developed vertical velocities of over
300 m/sec by 21 minutes into the run (see Fig. 30). These high
velocities caused the plume to far overshoot its level of neutral
buoyancy, reaching altitudes in excess of 40 km, where it became
overdense and fell back downwards. The downward-moving jet
penetrated near to the surface, where it led to the formation of a
closed vortex (see Fig. 31) which eventually caused the upward jet
to weaken (see Fig. 32). The continued heating at the surface,
however, leads to the formation of another intense, upward directed
jet along the axis (see Fig. 33), and this cycle continues until
the heating from the fire decreases. The resultant quasi-periodic
nature of the solution is most evident in the temperature histories
(see Fig. 29), and can also be seen in the histories of the inflow

california research and technology, inc.
dice 3550 case f-301 firestorm (qbdot=0.25e+9, radfac=0.3)
temperature vs. time, stations 1-3
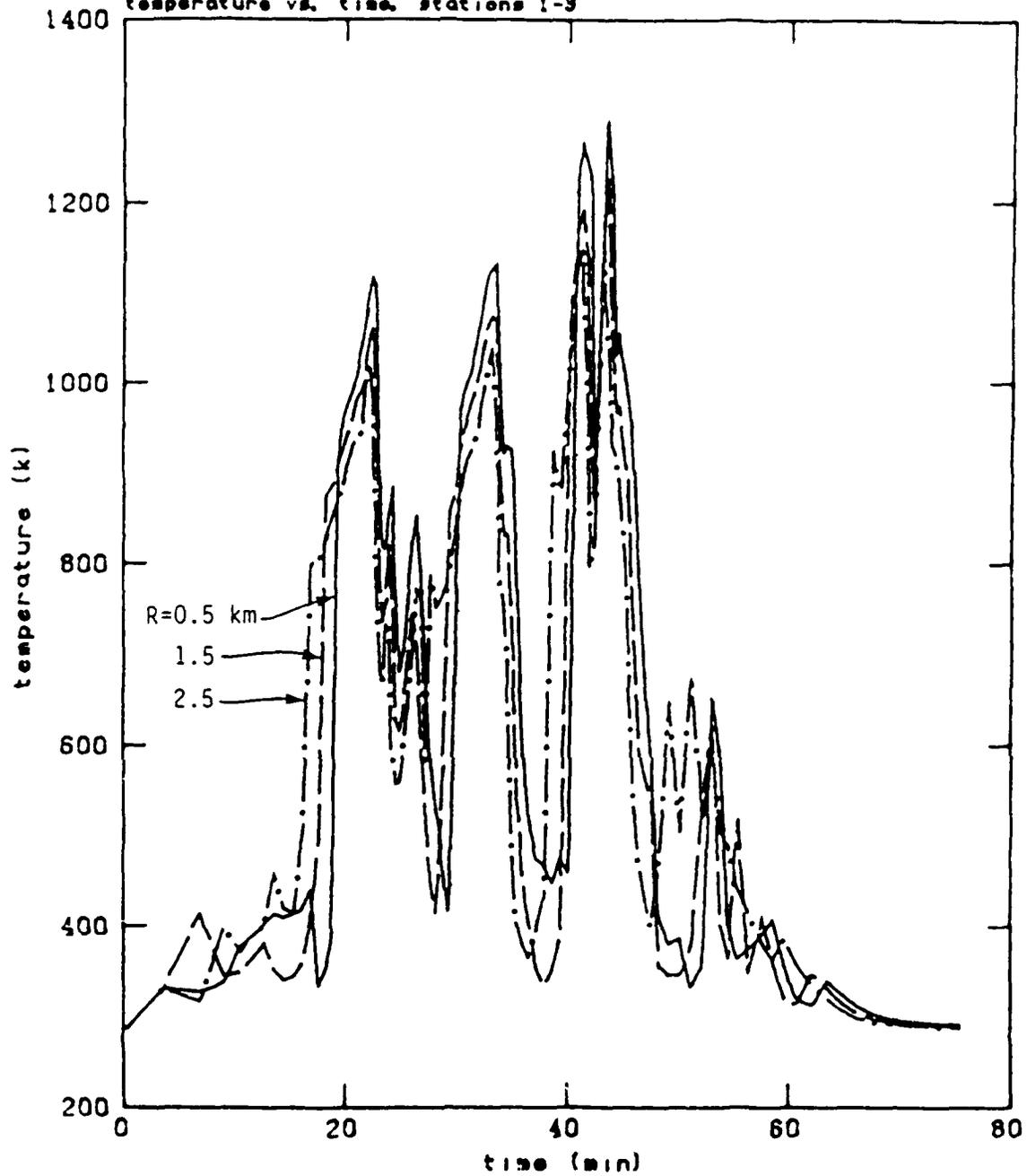
Figure 29. Time history of temperatures in the boundary
layer of Case 301.

64

california research and technology inc.
date 5550 case f-301 firestars (qbdot=0.25e+9 radfac=0.9)
velocity field cycle 5145
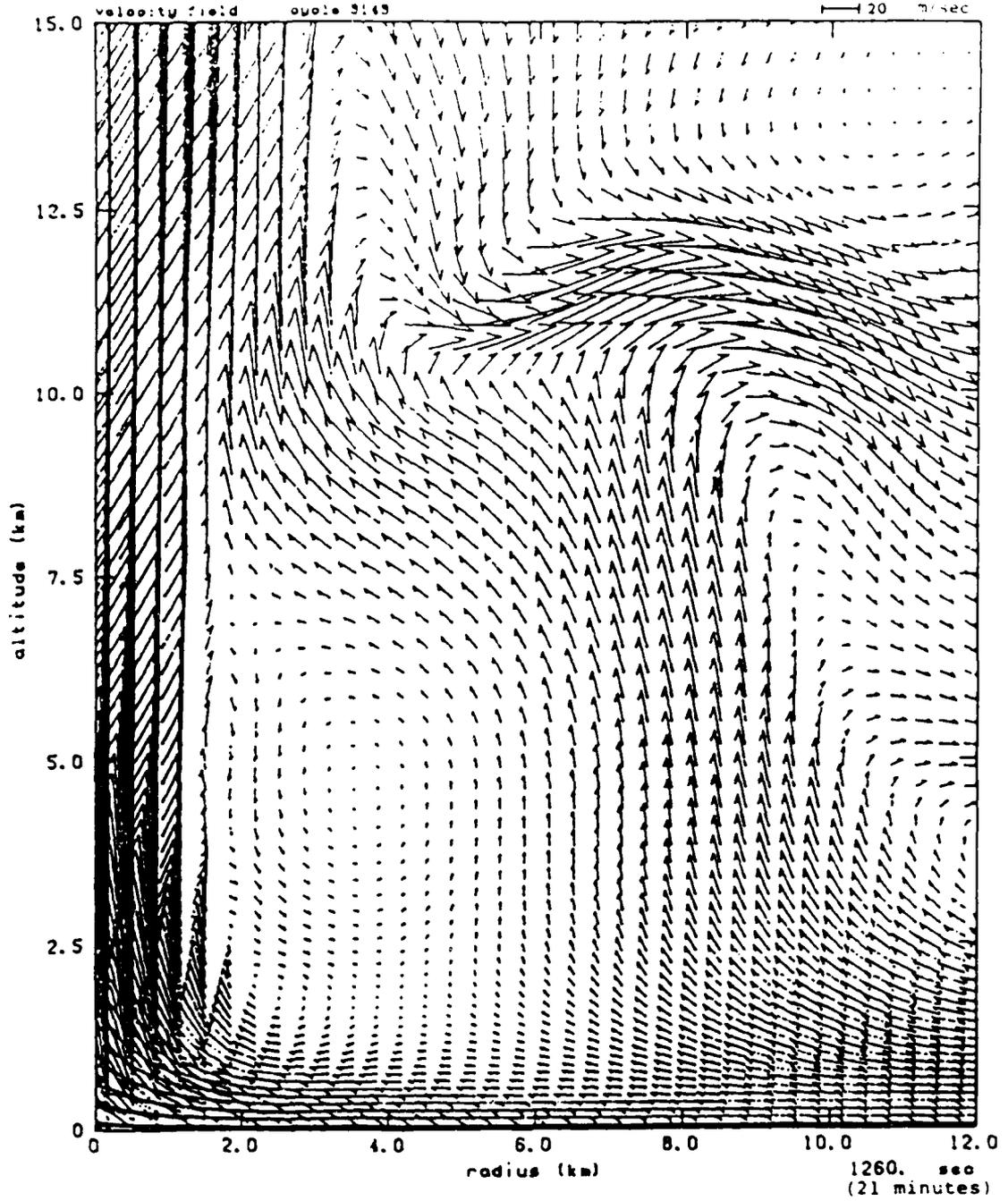
Figure 30. Velocity vector plot of Case 301 at 21 minutes.

65
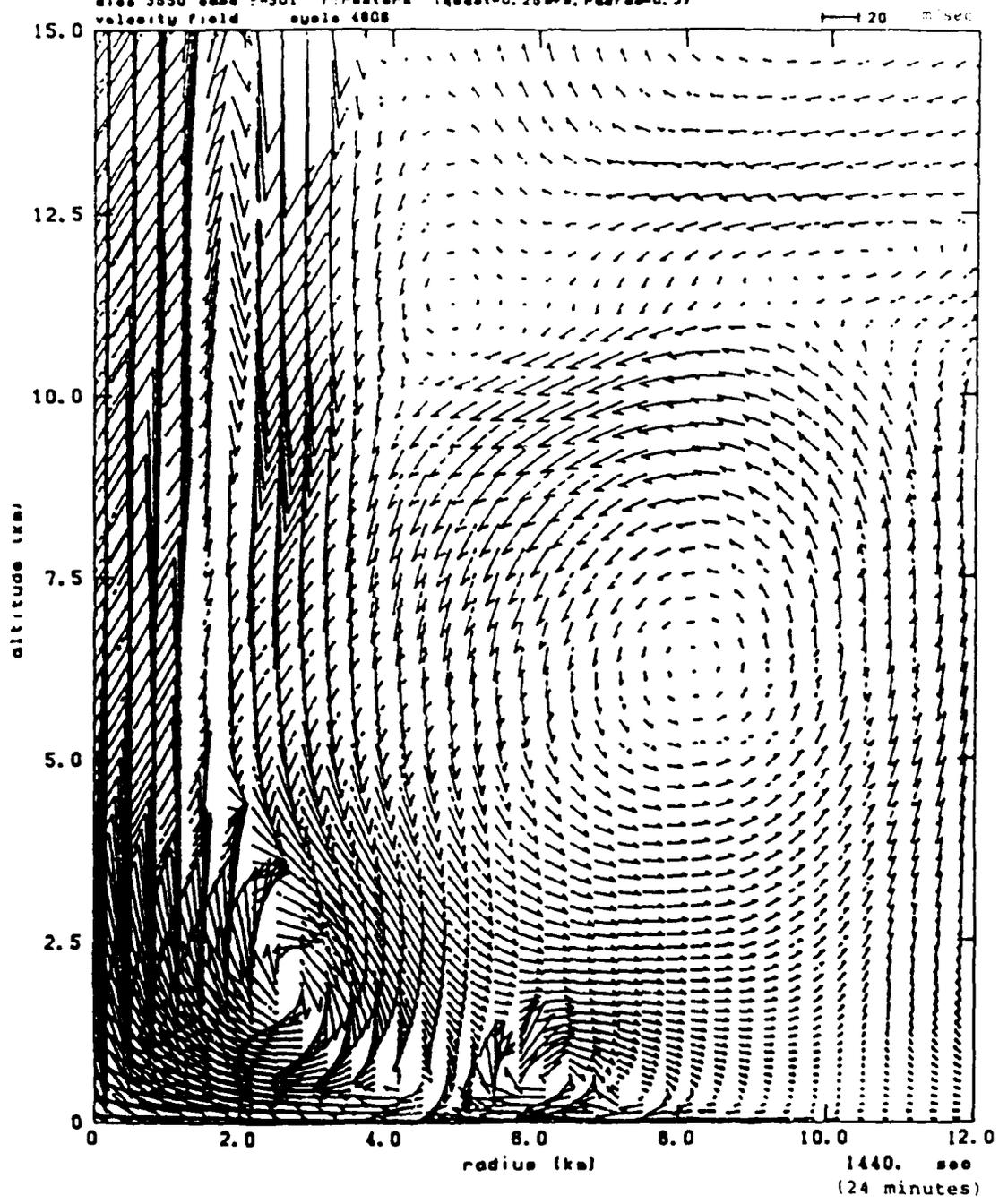
Figure 31. Velocity vector plot of Case 301 at 24 minutes.

66

california research and technology, inc.
disc 3550 case r-301   firestorm (sbdot=0.25e+8, redfac=0.3)
velocity field   cycle 8431
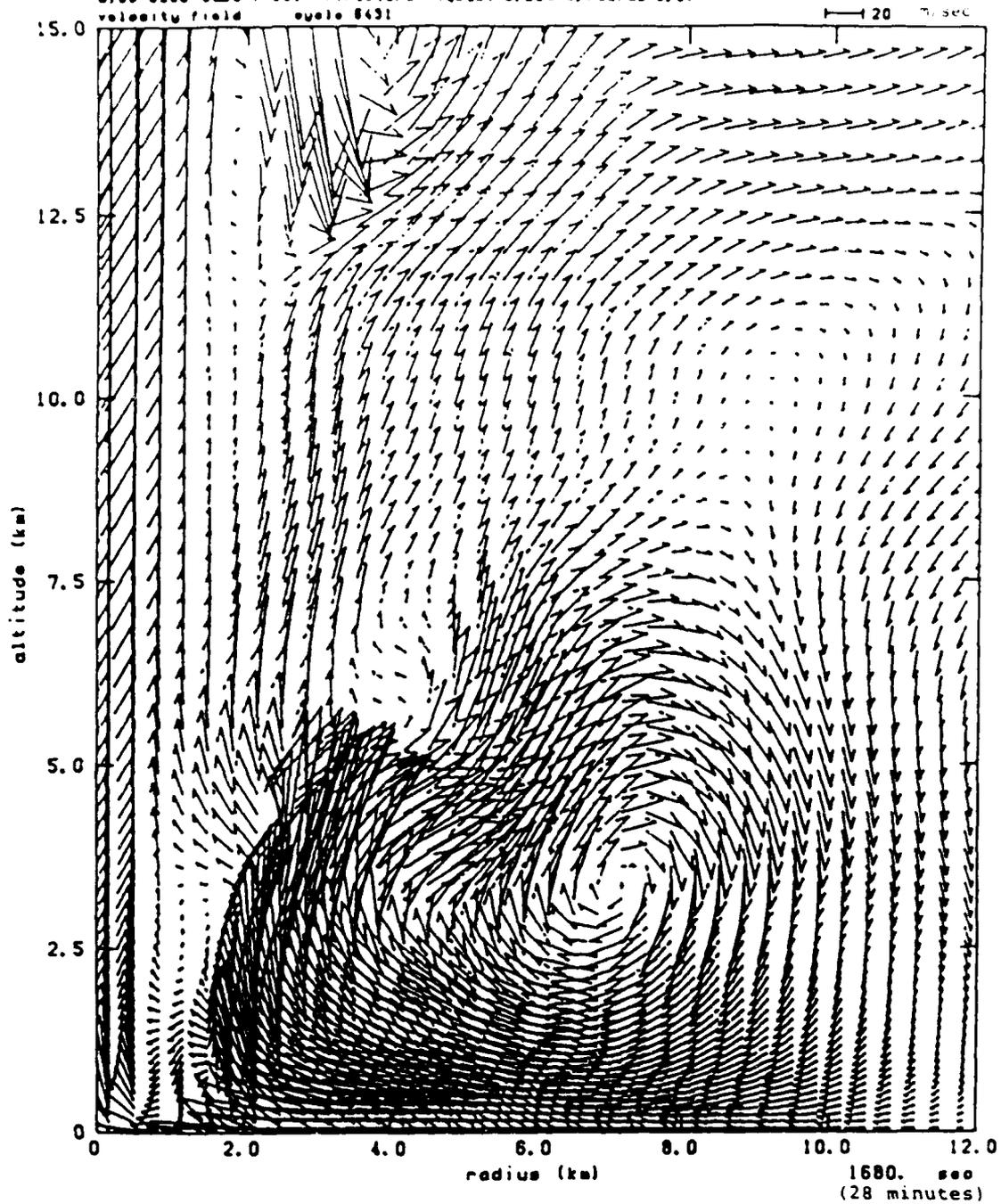
Figure 32.   Velocity vector plot of Case 301 at 28 minutes.

67

california research and technology, inc.
disc 3550 case f-301 firestorm (qbdot=0.25e+9, radfac=0.5)
velocity field   cycle 8998
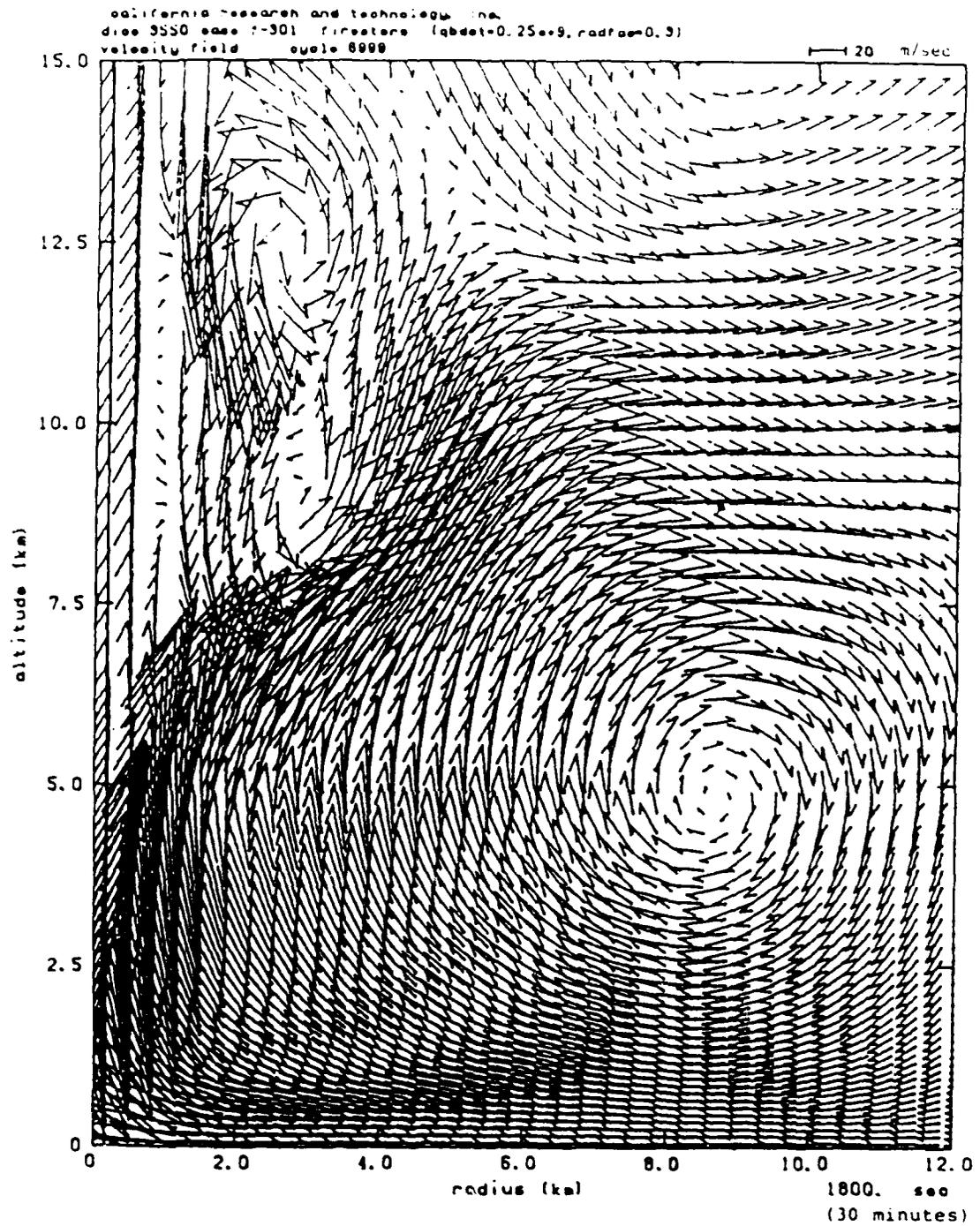
Figure 33.   Velocity vector plot of Case 301 at 30 minutes.

velocity at several locations in the boundary layer (see Fig. 5a).
The oscillatory behavior of the plume leads to the formation of two
distinct regions of lofted soot, as indicated by the positions
reached at one hour by massless tracers released every five minutes
from within the burning area (see Fig. 6a). One region near the
axis at an altitude of about 30 km is associated with the
overshooting phase of the plume, and the other, extending radially
outwards to a distance of 30 km near the altitude of the
tropopause, shows the location of the outflow area.

Case 502 used the same parameters as Case 301, except that the
grid spacing in the radial direction was twice as large. In spite
of this difference, the flow field for Case 502 exhibits upward and
downward jets and closed vortices similar to those obtained in Case
301, as shown by velocity vector plots of the two cases at 25
minutes (see Figs. 34a-b). Like Case 301, Case 502 exhibited a
quasi-periodicity of about ten minutes, as can be most readily seen
in the maximum temperature history for that case (see Fig. 4).
These temperatures were slightly less than the maximum temperatures
for Case 301 (compare with Fig. 29), since Case 301 had finer
radial zoning near the axis and was therefore better able to
resolve the hottest regions of the plume. Consequently the soot
tracer clouds for Case 502, while showing two regions of maximum
concentration as they did for Case 301, stabilized at slightly
lower altitudes (compare Figs. 6a-b).

Case 504 was identical to Case 502, except that the "slow"
burning scenario was used. The factor of 4 reduction in the
burning rate caused peak inward velocities at various ranges near
the ground to be reduced by about a factor of 2. Figs. 5b-c
compare radial velocity histories near the ground at ranges between
8.5 and 20 km. At the 8.5 km range, peak inward winds of about
40 m/sec (90 mph) are reduced to 20 m/sec for the high and low
burning rate cases, respectively. Time histories of the maximum
inward wind speeds, which are reached near the axis of the fire,
are shown for Cases 502 and 504 in Fig. 5d. Peak velocities reach

69
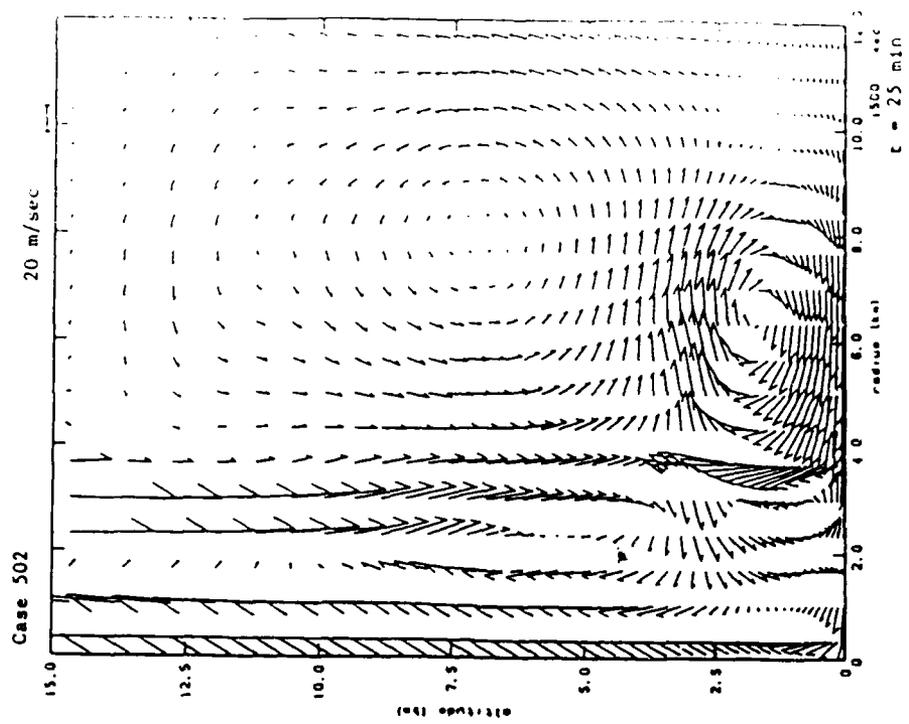
Figure 34b. Velocity vector plot of Case 502 at 25 minutes.
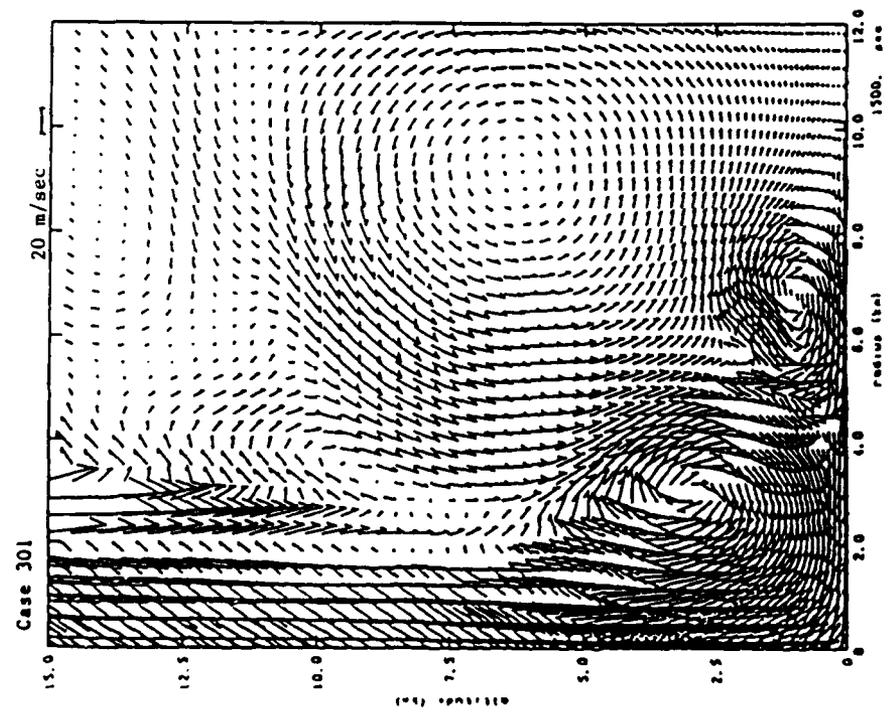
Figure 34a. Velocity vector plot of Case 301 at 25 minutes.

70

100 m/sec (220 mph) in the firestorm case, versus 50 m/sec (110 mph) for the group fire simulation. Buoyancy forces are the primary cause for the large wind speeds. One measure of this force is the maximum temperature in the burning region. The maximum temperature histories versus time for these two cases may be seen in Fig. 4. Maximum temperatures reach about $1000°K$ compared to $500°K$ in Cases 502 and 504, respectively.

The factor of 4 reduction in burning rate causes the maximum stabilization altitudes for lofted soot particles to be reduced by almost a factor of 2. Figs. 6b-c show a comparison of the positions of lofted soot tracers when the cloud has expanded about 30 km in radius; this radial expansion takes two hours in the reduced burning rate case compared to one hour in the higher rate case. There are two distinct regions of lofted particles in both cases. The higher region, near the axis, stabilized at a maximum altitude of about 25 km (Case 502) compared to 15 km (Case 504). The lower region of lofted particles forms a radially expanding volume with a mean altitude of about 10 km versus 5 km in the high versus low burning rate cases, respectively.

3.3 COARSE-ZONED CASES.

The remaining cases to be discussed in this section (the 600-series in Table 1) used a uniform grid with cell dimensions equal to 1 km. Since the combustion heating is added in the lowest layer of cells, the energy input from the fire in these cases is effectively "mixed" over the lowest 1 km of the computational domain, thereby crudely simulating the effects of turbulence in the inflow layer.

Case 601 is identical to Case 502, except for the change in zoning. Maximum temperatures for this case are much cooler than for 502, and reach a steady state by 30 minutes (see Fig. 4). The plume for case 601 also reaches a steady state by 30 minutes (compare Figs. 7a-b), and exhibits neither the intense, narrow jets

nor the closed vortices shown by Cases 301 and 502. The maximum altitude reached by 601's plume (18 km) is also lower than the maximum reached by Case 502 (40 km, not shown). Since the plume for Case 601 shows little tendency to overshoot, the associated tracer cloud (Fig. 6d) is concentrated near the tropopause, and does not show a second maximum at higher levels as in Cases 301 and 502, which had finer zoning and therefore hotter driving temperatures.

In Cases 603-608, 5% of the mass burned is converted to soot, 50% is converted to water vapor, and concentrations of soot, water vapor, liquid water, and ice are predicted by the model. Although phase changes of water are included, precipitation is not; most of the water vapor condenses into liquid, and eventually freezes into suspended ice particles as the cloud rises and cools adiabatically.

Case 603 differs from Case 601 only in the inclusion of soot and water species in the calculation. The soot cloud predicted for Case 603 at one hour (see Fig. 8) shows a maximum concentration in the lower stratosphere, as does the tracer cloud for Case 601 (see Fig. 6d). The configuration of the ice/water cloud predicted at one hour for Case 603 resembles that of the soot cloud (see Fig. 8), with a "shield" of particulates extending outwards above the tropopause to a radial distance of about 40 km after one hour. Concentration levels for the ice/water cloud are about an order of magnitude greater than those for the soot cloud, since ten times as much fuel mass is converted into water vapor as is converted into soot (see Table 1).

Both of the particulate clouds for Case 603 show considerable vertical dispersion, compared to the relatively thin outflow layer shown by the tracer cloud for Case 601 (see Fig. 6d); the ice/water cloud is confined to altitudes above 6 km, however, since water vapor below this altitude has not yet undergone sufficient cooling to condense. Both clouds show maximum concentration near the axis, indicating that most of the condensation of water vapor occurs in

72

this region. Although the latent heat released by the condensing water vapor amounts to only 5% of the total combustion energy released by the fire, the concentration of this heating in a relatively small area in the core of the plume causes it to overshoot slightly, compared to the plume for Case 601; this in turn leads to the formation of secondary maxima in both of the particulate clouds at altitudes above 20 km near the axis.

Case 604 is the same as Case 603 except that the "slow" burning scenario is used. Fig. 10 shows that in this case also, the release of latent heat by condensing water vapor near the axis leads to a double-lobed soot cloud (note that the lower ice cloud is missing, since water vapor which detrains below 5 km has not yet undergone sufficient cooling to condense). As for Case 504 the slower burning rate leads to lower plume temperatures, and the reduced buoyancy which results causes the plume to stabilize at a lower height. The upper concentration maximum descends from 22 km in Case 603 to 12 km in Case 604, and the lower concentration maximum descends from 12 km to 5 km, as the burning rate is reduced by a factor of 4.

Case 605 is also identical to Case 603, except that the burning radius for 605 was increased from 10 to 30 km; thus although both cases have the same energy release rate per unit area, the total energy release for Case 605 is almost an order of magnitude greater than 603's. For the first 30 minutes the main body of 605's plume does not penetrate above 18 km (see Fig. 12a), and the soot and ice/water clouds at that time, while containing more total mass than the clouds for Case 603 (since more fuel has been burned), are also confined below that altitude (see Fig. 12b). By 45 minutes into the run, however, as the inflow from the larger heating area reaches the axis, an intense plume penetrates above 40 km altitude (see Fig. 12a).

Case 606 is the same as Case 603 except that the burn radius is reduced from 10 km to 3 km. In this case, as in the "slow"

burning scenario (Case 604), most of the soot is confined to the troposphere, although some portions of the soot cloud penetrate into the stratosphere near the axis (see Fig. 11). The ice/water cloud is also largely confined to the troposphere, although the altitude of maximum concentration is somewhat higher than that of the soot cloud, since water vapor in the lower troposphere has not been cooled enough to condense. The lateral spreading rate of the particulate clouds are also greatly reduced; the ice/water cloud, in particular, reaches a radial extent of only 6 km after one hour, compared with 30 km in Case 603, which had a burn radius of 10 km (see Fig. 8).

Case 608 is the same as Case 603 except that the ambient atmosphere is moist, with the initial relative humidity varying linearly from 60% at the surface to zero at an altitude of 30 km. In Case 603, latent heat released by water vapor which formed during combustion of the fuel led to a moderate increase in plume height (26 km compared to 18 km for Case 601). When ambient moisture from a moderately humid atmosphere is added, however, the effects of latent heat release are much greater, with the plume for Case 608 passing an altitude of 30 km by 30 minutes into the run (see Fig. 9).

3.4 DISCUSSION.

Cases 606, 603, and 605, all of which used the "fast" burning scenario, illustrate the effects of increasing the burn radius from 3 to 10 to 30 km. In Case 606, for which the burning area was similar to that which characterized the largest firestorms occurring in the Second World War, most of the soot is confined to the troposphere, with the cloud top reaching 14 km. When the burning radius is increased to 10 km (considered the nominal burn radius for a 1-MT airburst), the height of the soot cloud is raised considerably, with the maximum concentration now occurring above the tropopause (see Fig. 8), and the cloud top reaching 26 km.

74

Increasing the burn radius to 30 km results in another large increase in the plume height (see Fig. 12a).

The "fast" burning scenario is intended to simulate the burning rate from World War II firestorms, which occurred in old, high-density city centers. Use of the "slow" burning scenario, which may be more representative of modern, low-density cities, results in a considerable lowering of the estimated cloud height for a 10 km radius fire (compare Case 603 with 604, and 502 with 504). These cases show that predicted cloud stabilization heights, and in particular the degree of penetration of soot into the stratosphere, are dependent on the radius and burn rate of the postulated fire. Case 608 also showed that the plume height may be quite sensitive to the humidity of the ambient atmosphere at the time of the fire.

For the cases which used the "fast" burning scenario and a dry atmosphere, two types of solution were obtained, depending on the amount of mixing which is allowed to occur in the boundary layer. When the combustion heating is confined to a layer 0.1 km thick, high temperatures result, leading to overshooting plumes and a quasi-periodic solution; when the combustion heating is "mixed" over a lower layer depth of 1.0 km, however, cooler temperatures and less energetic plumes lead to solutions which approached a steady-state during the constant heating phase. Although in general we do not expect periodic solutions from non-periodic heat sources, the fires which we are simulating are of unprecedented size (with a typical width more than twice the e-folding depth of the atmosphere), and the oscillatory behavior which we obtained may have a physical basis. Mixing evidently plays a key role in the dynamics of the plumes, however, and in order to resolve this question, a more systematic treatment of its effects in the model is needed. To this end, a simplified turbulence model has been developed and incorporated into the code.

SECTION 4

THE EFFECTS OF PARAMETERIZED TURBULENCE

4.1 FORMULATION OF THE MODEL.

Turbulent motions, which involve a wide range of length scales and are inherently three-dimensional, are not calculated explicitly in our model. Instead, the turbulence is "averaged out" by applying an averaging operation to the original governing equations. For example, the governing mass continuity and momentum equations for a perfect incompressible fluid are

$$\frac{\partial U_j}{\partial x_j} = 0$$

$$\frac{\partial U_j}{\partial t} + U_k \frac{\partial U_j}{\partial x_k} = -\frac{\partial}{\partial x_j}\left(\frac{p}{\rho_o}\right) + F_j \tag{7}$$

where U_j is the j-th component of the velocity vector, p is pressure, ρ the density, and F_j the net body force acting on the fluid. Divide the variables into a mean part (denoted by an overbar) and a deviation from the mean:

$$U_j = \overline{U_j} + U_j'$$

$$p = \overline{p} + p' \tag{8}$$

Substitute these into Eqn. (1) and average to get the mean governing equations:

$$\frac{\partial \overline{U_j}}{\partial x_j} = 0; \quad \frac{\partial \overline{U_j}}{\partial t} + \overline{U_k} \frac{\partial \overline{U_j}}{\partial x_k} = -\frac{\partial}{\partial x_j}\left(\frac{\overline{p}}{\rho_o}\right) - \frac{\partial}{\partial x_k} \overline{U_k' U_j'} + \overline{F_j} \tag{9}$$

76

Note the additional term in Eqn. (9). This represents the
turbulent momentum transport, and adds three unknowns to the four
we already have. Since we still have only four equations (one
continuity and three momentum), the set is not closed. To close
the set, we must somehow specify the turbulent fluxes. This is
the turbulence closure problem.

Many turbulence closure models have been developed. Some
assume that turbulent transport is like molecular diffusion.
Others use equations such as the turbulent kinetic energy
equation in their models, and take the buoyant generation of
turbulent kinetic energy into account. How do we choose a
turbulence model that is appropriate for the flow of interest?
Our philosophy is to use the simplest model that includes the
processes that create or destroy turbulent kinetic energy in the
flow of interest.

We will use the Boussinesq equations in Cartesian
coordinates. The averaged continuity, momentum, and
thermodynamic equations are

$$\frac{\partial \overline{U_j}}{\partial x_j} = 0$$

$$\frac{\partial \overline{U_j}}{\partial t} + \overline{U_k} \ \frac{\partial \overline{U_j}}{\partial x_k} = -\frac{\partial}{\partial x_j}\left(\frac{\overline{p}}{\rho_o}\right) - \frac{\partial}{\partial x_k} \ \overline{U_k'U_j'} + g_i \ \frac{\overline{\theta}}{\theta_o} \qquad (10)$$

$$\frac{\partial \overline{\theta}}{\partial t} + \overline{U_k} \ \frac{\partial \overline{\theta}}{\partial x_k} = -\frac{\partial}{\partial x_k} \ \overline{U_k'\theta'}$$

Here $\theta = T(p_o/p)^{0.277}$ is the potential temperature, where T is
the temperature. P_o is a constant reference pressure, θ_o is
a constant reference temperature, and $\overline{U_k'\theta'}$ is the turbulent
flux of potential temperature. We will specify the unknown
turbulent covariances in terms of the mean fields as follows:

$$\overline{U_i'U_j'} \;=\; \frac{q^2}{3}\,\delta_{ij} \;-\; q\ell_1\left(\frac{\partial\overline{U_i}}{\partial x_j} + \frac{\partial\overline{U_j}}{\partial x_i}\right)\,,$$

(11)

$$\overline{U_i'\theta'} \;=\; -\,q\ell_2\,\frac{\partial\overline{\theta}}{\partial x_i}\,,$$

where q is the r.m.s. turbulent velocity (a measure of the turbulent kinetic energy), and ℓ_1 and ℓ_2 are turbulent length scales. These models are strictly valid only in the limit of isotropic, nearly homogeneous turbulence.

To close these equations (treating $\overline{U}_i$ and $\overline{\theta}$ as known) we need an equation for q^2. This is the turbulent kinetic energy equation:

$$\frac{dq^2}{dt} = -\frac{\partial}{\partial x_j}\,\overline{U_i'U_i'U_j'} - 2\,\overline{U_i'U_j'}\left(\frac{\partial\overline{U_i}}{\partial x_j} + \frac{\partial\overline{U_j}}{\partial x_i}\right) + 2\,\frac{q}{\theta_o}\,\overline{U_i'\theta_i'} - 2\epsilon \quad (12)$$

The first term on the right represents the turbulent transport, the second the shear production, the third the buoyant production, and the last is molecular dissipation. We assume that production and dissipation balance:

$$0 = S.P. + B.P. - D, \tag{13}$$

use the above models for the fluxes, and model dissipation by

$$\epsilon = q^3/\Lambda_1. \tag{14}$$

The result is

$$q^2 = \Lambda_1\,\ell_1\left[S_{ij}S_{ij} - \frac{\ell_2}{\ell_1}\,\frac{g_i}{\theta_o}\,\frac{\partial\overline{\theta}}{\partial x_i}\right] \tag{15}$$

78

where
$$S_{ij} \equiv \frac{\partial \overline{U_i}}{\partial X_j} + \frac{\partial \overline{U_j}}{\partial X_i}$$
(16)

Let $\ell_1 = A_1 \ell$, $\ell_2 = A_2$, and $\Lambda_1 = B_1 \ell$, where ℓ is a master turbulent length scale, and A_1, A_2, and B_1 are constants known from measurements.

We still must specify the master turbulent length scale. To do this, we first identify a natural length scale in the flow. Then we must determine the relationship between the natural and turbulent length scales. If we use measurements from actual turbulent flows to determine this relationship, we must then decide whether this relationship is likely to hold in the flow we wish to simulate.

A plume has three regions: the inflow layer, the plume column, and the outflow layer. Each has a natural length scale. The inflow layer's depth is a natural length scale, as is the width of the plume column and the depth of the outflow layer. What are the relationships between these natural length scales and the turbulent length scales? The inflow layer is a boundary layer, so we can use Blackadar's [4] formula:

$$\ell = \ell_\infty \frac{\kappa z}{\kappa z + \ell_\infty}$$
(17)

where κ is von Karmen's constant, z is the height above the surface, and ℓ_∞ is related to the depth of the boundary layer. Yamada and Mellor [5] related ℓ_∞ directly to the turbulence profile:

$$\ell_\infty = 2\alpha \frac{\int_0^\infty qz \; dz}{\int_0^\infty q dz}$$
(18)

79

where $\alpha = 0.1$. We could use the turbulence model-derived values of q, the r.m.s. turbulent velocity, to estimate l_∞. This could be done at each radial location every time-step while the simulation proceeds. We didn't do this. Instead, we simply specified l_∞ for each case.

Far from a boundary, the turbulent length scale is related directly to the width of the turbulent region, and we could use the formula above to relate l_∞ to the turbulence profile across the plume column or outflow layer at each time step. Since the aspect ratio of the firestorm plume is only of order unity, however (see Fig. 7), it will have a large volume to surface area ratio. We expect the effects of turbulent entrainment to be small in the region of the plume column, therefore, and so for simplicity, Eqn. (17) was used to specify the turbulent mixing length once and for all throughout the computational domain.

4.2   CASES 702 AND 705.

These cases were similar to Case 502, in that they used the "fast" burning scenario and the same grid; the turbulence model was included, however, with the master turbulent length scale, l_∞, set equal to 100 meters for Case 702 and 25 meters for Case 705 (see Table 2).

Fig. 14 shows the time evolution of the velocity fields. At 15 minutes, the inflow layers are nearly fully developed and contain peak winds of more than 50 m/s, but the plumes are just starting to develop. During the next five minutes, the plumes shoot upwards at 50 m/s (Case 702) and 80 m/s (Case 705) and reach 21 km (Case 702) and 30 km (Case 705). By 30 minutes, the plumes are nearly steady, and reach maximum heights of 24 km (Case 702) and more than 30 km (Case 705).

After ascending in the plumes, the air descends and oscillates about its non-buoyancy level slightly before stabilizing in the outflow layer. This layer extends from about 12 to 15 km altitude in Case 702 (ℓ_∞ = 100 m) and from about 13 to 18 km altitude in Case 705 (ℓ_∞ = 25 m), as shown in Fig. 14d. We also released tracer particles at the surface within the burning region at five minute intervals. Their locations should indicate the top of the stabilization or outflow layer of the plume, since they will follow the surface air, which (we will see) is the warmest and therefore most buoyant. The tracer particle locations at 45 minutes are shown in Fig. 15; they are labeled sequentially according to their time-of-release. The tracer particles indicate that the outflow layer top is about 15 km in 702 and from 15 to 19 km in Case 705.

Fig. 35(a) compares the temperature departure from the initial conditions at 30 minutes for Cases 702 and 705; Fig. 35(b) is the same but shows only the lowest and innermost 10 km. Since the temperature departure is proportional to the buoyancy force, differences in the temperature fields are related to the differences in the plume dynamics. The plume in Case 705 (ℓ_∞ = 25 m) reaches higher than does Case 702's plume (ℓ_∞ = 100 m). Fig. 35(a) shows that at all altitudes below 21 km, Case 705's plume contains warmer air at the axis than does Case 702's plume, which is consistent with its greater height. Figs. 35(b) and 13 show that the inflow layer became about 100°K warmer in Case 705 than in Case 702. This difference is due to greater turbulent mixing in Case 702's inflow layer.

One might ask whether the inflow is more rapid in Case 702 than in Case 705, which would allow less time for the air to heat up. Fig. 36 shows that this isn't the case; the maximum inflow speed is about 50 m/s in Case 702 and 60 m/s in Case 705.

For comparison, temperature departure fields at 30 minutes for the inviscid Cases 502 (Δz_o = 100 m) and 601 (Δz_o = 1000 m)
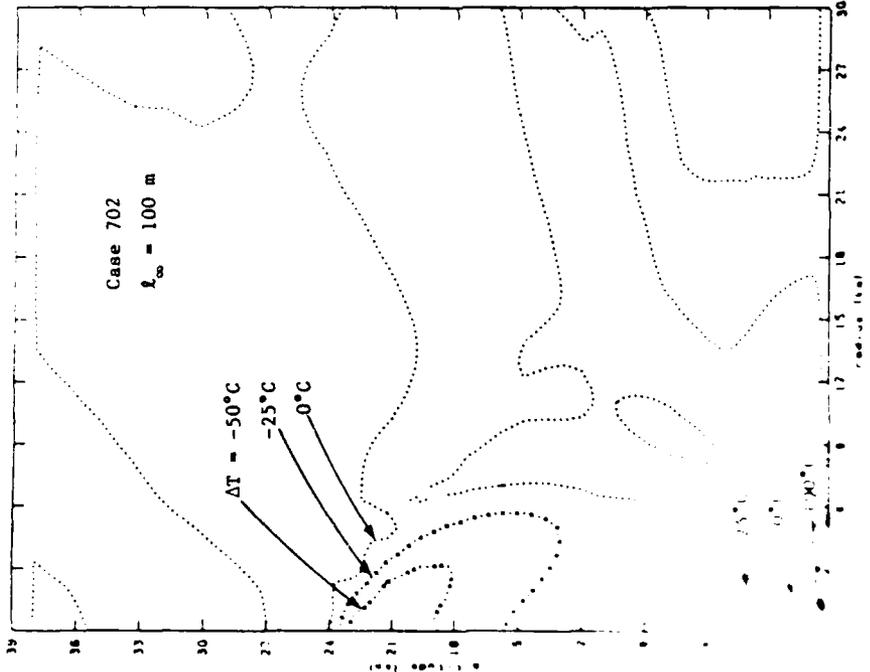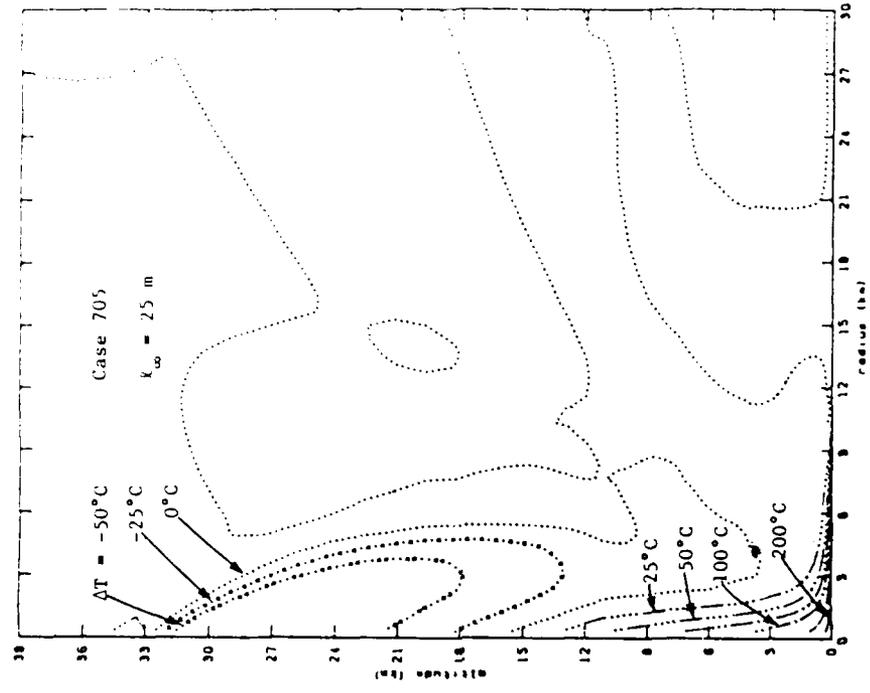
81

Case 705

$\ell_\infty = 25$ m

$\Delta T = -50°C$
$-25°C$
$0°C$

$25°C$
$50°C$
$100°C$
$200°C$

Case 702

$\ell_\infty = 100$ m

$\Delta T = -50°C$
$-25°C$
$0°C$

Temperature departure at 30 minutes for Cases 702 and 705.

AD-A188 375   NUMERICAL SIMULATION OF NEAR-SURFACE ENVIRONMENTS AND   2/2
     PARTICULATE CLOUDS   (U) CALIFORNIA RESEARCH AND
     TECHNOLOGY INC CHATSWORTH   S L MARCUS ET AL   24 AUG 87
UNCLASSIFIED   CRT-3880F DNA-TR-87-1 DNA001-83-C-0017   F/G 19/11   NL
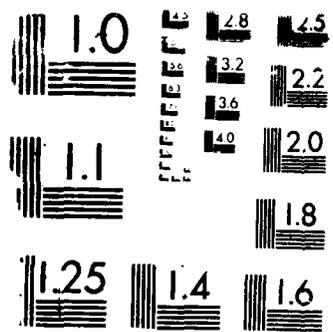
MICROCOPY RESOLUTION TEST CHART
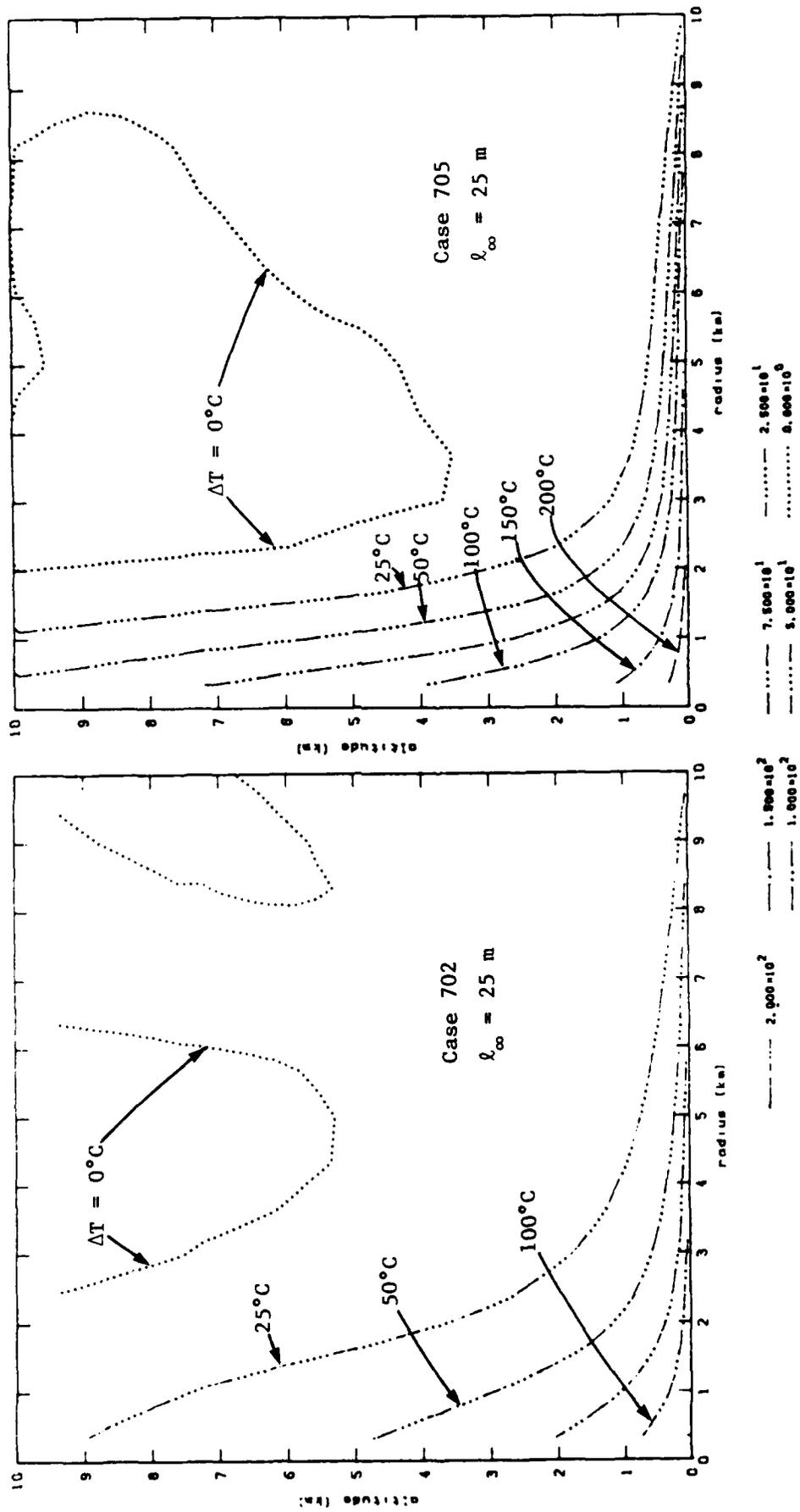
Figure 35b. Temperature departure at 30 minutes for Cases 702 and 705 (close view).
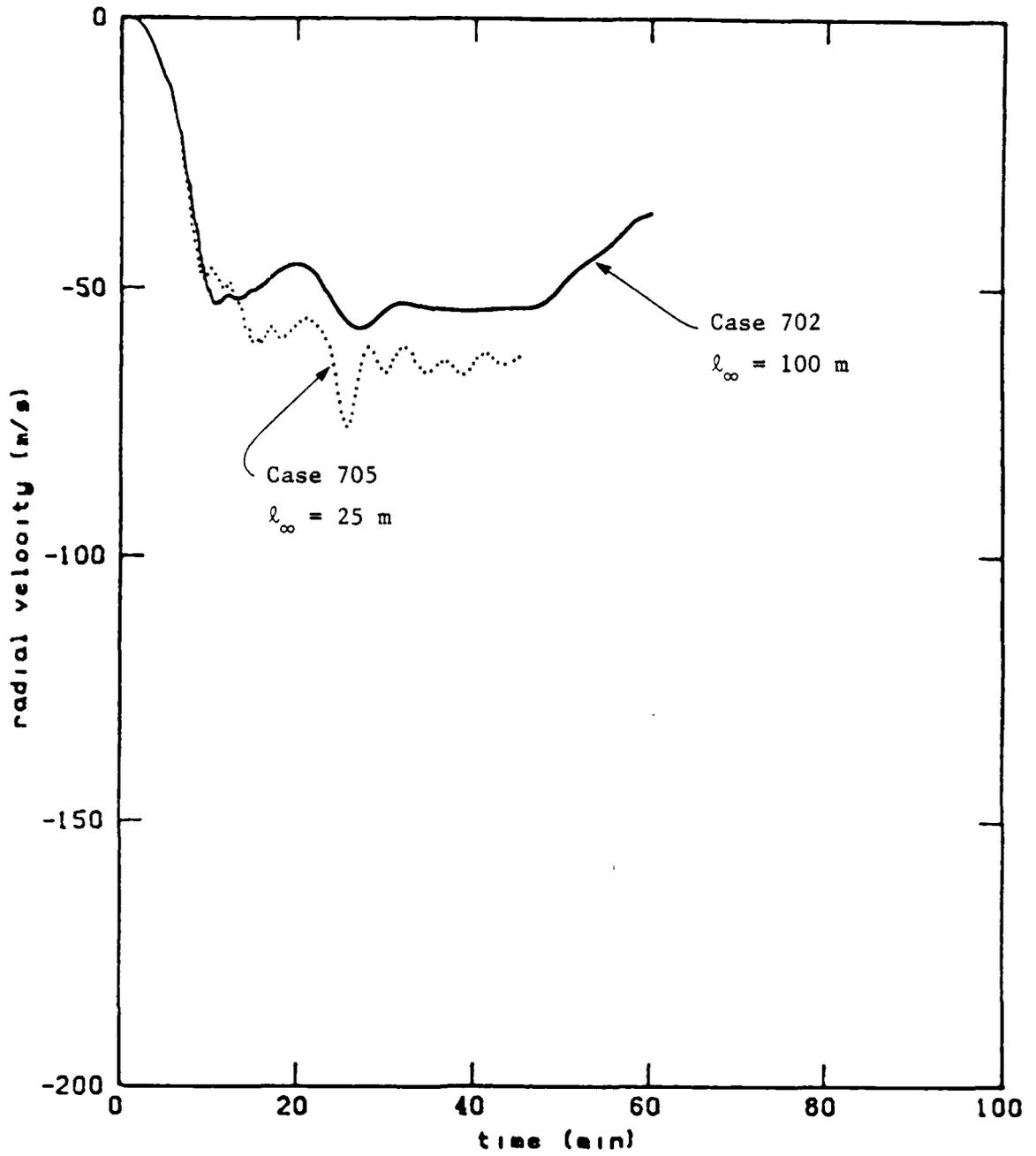
Figure 36. Maximum inflow velocity for Cases 702 and 705.

84

are shown in Fig. 37. The most striking difference between the temperature departure fields for these two cases may be seen in the inflow layer, where over-temperatures reach 400°K in Case 502, but only 50°K in Case 601. The temperature departure fields for the turbulent Cases 702 and 705 (see Fig. 35b) are intermediate between those for 601 and 502. This means that larger grid cells in the lowest layer increase the mixing in the inflow layer. This occurs because distributing the burning through the lowest layer of large cells is equivalent to distributing the burning through several thinner cell layers.

From a comparison of Cases 702 and 705, it is evident that the plume dynamics, and in particular the stabilization height, depend on the asymptotic turbulent length scale (l_∞) which is specified. How do we decide which length scale is best?

Fig. 16 shows how l_∞, as defined in Eqn. 18, depends on the depth (Δ) of the boundary layer for three different profiles of q. For a uniform distribution of q with height, l_∞ is a tenth of the depth of the boundary layer, while for a Gaussian distribution of q, l_∞ is 0.14 times the half-width of the profile. Thus, we expect that the most realistic simulation will be the one in which the prescribed l_∞ is 1/10 to 1/7 of the turbulent boundary layer depth.

We estimated the turbulent boundary layer depth to be the height of the 25°K temperature departure isotherm at 5 km radius at 30 minutes. We picked this height because this is (approximately) equal to the cell depth in Case 601. Since 601 has no turbulent mixing between cells, the cell depth is the same as the mixed or "turbulent" layer depth when the flow is purely horizontal between 5 and 10 km. This is the case for 601; see Fig. 7.

The estimated turbulent boundary layer depths are shown in Fig. 16 under the column heading Δ. They range from 300 m in

85
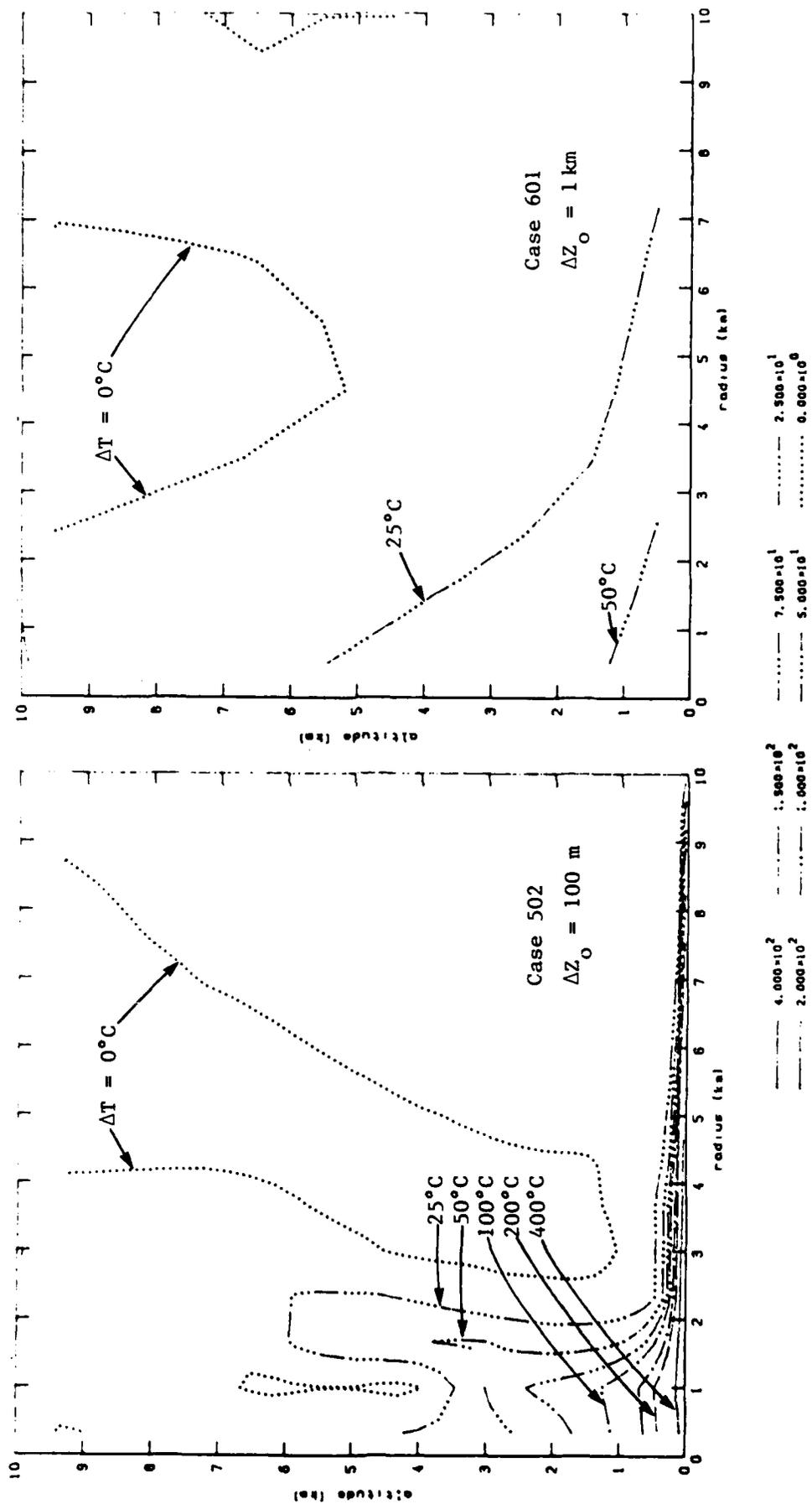
Figure 37. Temperature departure at 30 minutes for Cases 502 and 601.

Case 502 to 1100 m in Case 601. Also listed are ℓ_∞/Δ. This is 1/8 for Case 702 and 1/24 for 705. ℓ_∞/Δ would be have to be smaller than 1/24 for Case 502 and larger than 1/8 for Case 601 to produce the "observed" boundary layer depths.

4.3 DISCUSSION.

Since Case 702 had a value of ℓ_∞/Δ which lies between 1/10 and 1/7, it would appear to be the most realistic of the simulations discussed so far. The table in Fig. 16 shows that the boundary layer depth for this Case (800 m) was closer to that for Case 601 (1100 m) than to Case 502 (300 m), and the plume for Case 702, which approached a steady-state at moderate altitude, also resembles Case 601's plume (compare Figs. 14cd and 7ab). This shows that the effects of parameterized turbulence in a finely-zoned grid are similar to the enhanced mixing which results from the use of a coarse grid, and indicates that of the inviscid cases, the 600-series was probably the more realistic.

The results of Case 702 indicate that most of the contaminants from a 10-km radius fire, with a peak burning rate of 250 kW/m^2, would be expected to detrain at levels well within the stratosphere (see Fig. 15). How much credibility can be attached to results such as these? In order to be confident that the dynamics of the thermal plumes are being accurately represented, the numerical models used should be verified with experimental data. Experiments on the firestorm scale are impractical, of course, but verification with smaller-scale test fires may partially satisfy this requirement. One such study using the DICE code is discussed in the following section.

SECTION 5

THE METEOTRON EXPERIMENT

5.1 OVERVIEW.

We used our model to simulate a 600-Megawatt test fire conducted at the Meteotron facility of the Centre de Recherches Atmospheriques, France, on October 23, 1973. The experimental plume at the Meteotron facility was produced by the array of oil burners depicted in Fig. 17. Our model did not attempt to resolve individual flames, but assumed a steady, uniform heat input of 150 kW/m^2 into the lowest layer of computational cells, over a circular area of radius 36 m. The computational domain measured 1 km radially by 2 km vertically, with continuum boundary conditions to allow for the flow of air out of or into the domain.

5.2 INITIAL CONDITIONS.

The ambient atmospheric temperature profile measured at the time of the burn is shown in Fig. 18. The lapse rate between the surface and 650 m was about equal to the dry adiabatic lapse rate of -1°C/100 m, indicating a layer of neutral stability. At 650 m there was a sharp inversion, with temperatures continuing to increase up to a height of 1250 m, indicating a layer of high static stability.

A contour plot of the initial potential temperature field is shown in Fig. 38a. In this representation, the layer of neutral stability appears as a region of constant potential temperature; the overlying stable layer, characterized by a rapid increase of potential temperature with height, appears as a region of closely packed isentropes (lines of constant potential temperature). An isentropic plot of the U.S. Standard Atmosphere is shown for

88
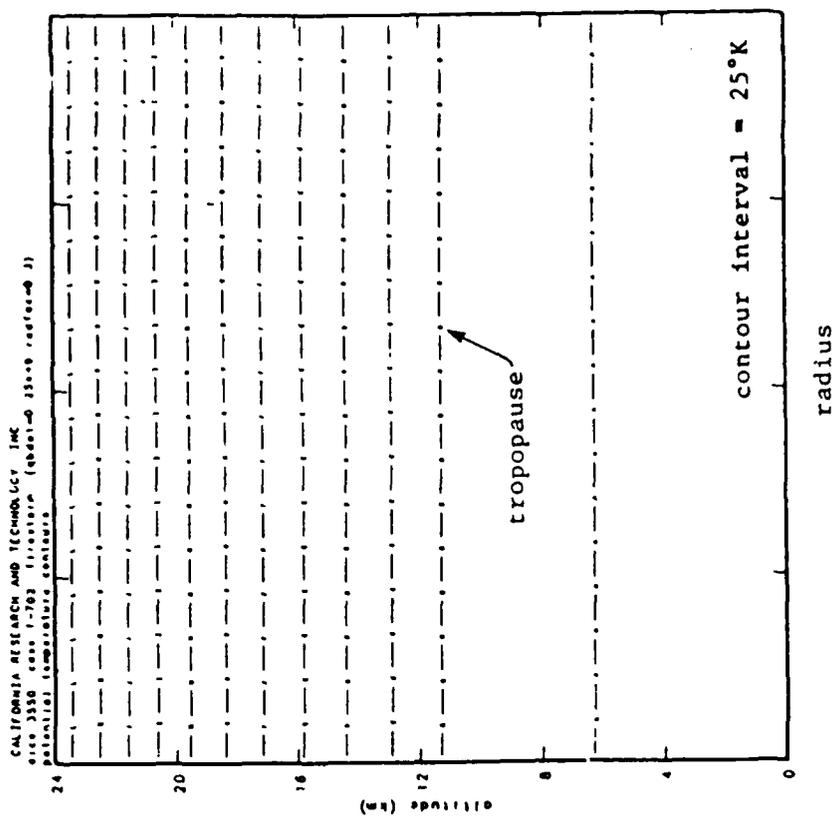
Figure 38b. Potential temperature field for the U.S. standard atmosphere.
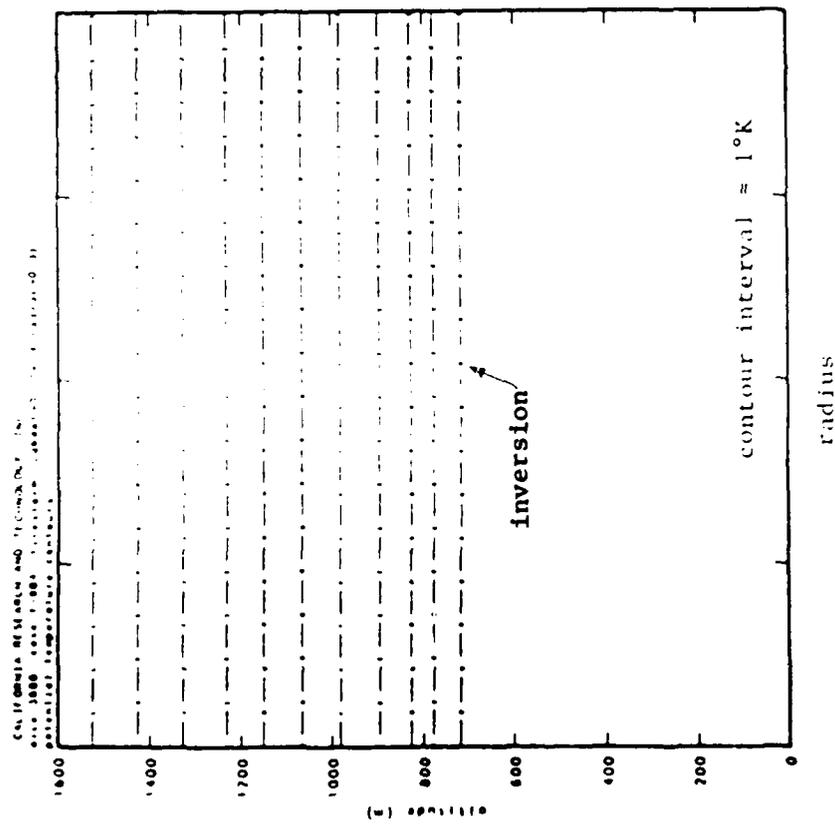
Figure 38a. Initial potential temperature field for the Meteotron experiment.

89

comparison in Fig. 38b (note the different scaling). In this figure the troposphere appears as a region of low static stability (weak potential temperature gradient), while the stratosphere appears as a region of high static stability (strong potential temperature gradient). These figures show that the structure of the lower atmosphere for the October 23 Meteotron burn resembled a scaled-down version of the troposphere-stratosphere system.

For the large-area fires we have been discussing the radius of the burning area is greater than the e-folding depth of the atmosphere, and the aspect ratio (height to width) of the resulting plumes is of order unity. The radius of the Meteotron fire, however, is much smaller than atmospheric length scales, and consequently we expect the aspect ratio of the resulting plume to be much larger than for the firestorm cases. In this situation turbulent entrainment into the region of the plume column has a greater effect on the buoyancy than entrainment in the inflow layer. We, therefore, took the natural length scale for the Meteotron plume to be 72 m, the width of the burning region, and the turbulent length scale ℓ_∞ was taken to be 8 m, a value which lies between 1/10 and 1/7 of the natural length scale.

5.3 RESULTS.

During the course of the October 23 experiment, the burners were run for ten minutes, with a "plume steady state resulting after five minutes; no further increase of the top plume was visible" [6]. For comparison, the development of the model plume can be most quickly visualized in Fig. 19, which shows the heights reached by tracers released at one minute intervals from the computational cell nearest to the center of the fire. From this figure it is evident that the model plume reached its maximum altitude between five and six minutes into the run, in agreement with the experiment. Between six and seven minutes

90

there was little further evolution of the model plume, and the fields computed at seven minutes were taken to represent the plume steady state.

The top plume altitude for the experiment was reported to be 1260 meters, while the maximum altitude of the plume axis was given as 1050 meters [6]; the difference between these two heights is due to the inclination of the axis of the experimental plume to the vertical, and may be regarded as a rough measure of "experimental error." The two reported heights have been plotted with solid horizontal lines in Fig. 19, where it can be seen that the model plume top height was well within the experimental range.

In both the experiment and the model simulation, the plume penetrated the inversion and rose a considerable distance into the overlying stable layer. This process is depicted in Figs. 39a-39f, which show predicted contours of the model potential temperature field at one minute intervals, starting from the initial condition depicted in Fig. 38a (note that the highest contour plotted in these figures is 293°K). During the first two minutes the plume is confined to the lower neutral layer, although disturbances from gravity-acoustic waves have propagated into the overlying stable layer (Figs. 39a-b). By three minutes into the run, the plume has reached the base of the inversion; below this level, entrainment of cooler environmental air causes the potential temperature of the plume to decrease with height (Fig. 39c). As the plume penetrates into the overlying stable layer (Figs. 39d-e), the ambient atmosphere is displaced by a large region of uniform potential temperature, indicating that entrainment of environmental air towards the axis is small in this region. The air in the plume therefore cools adiabatically as it rises into the stable layer, leading to temperatures near the axis as much as 3.5°C below ambient values at an altitude of 1100 meters (Fig. 39f). Temperatures in the overshoot region (above 750 m) were not reported in [6], so

91
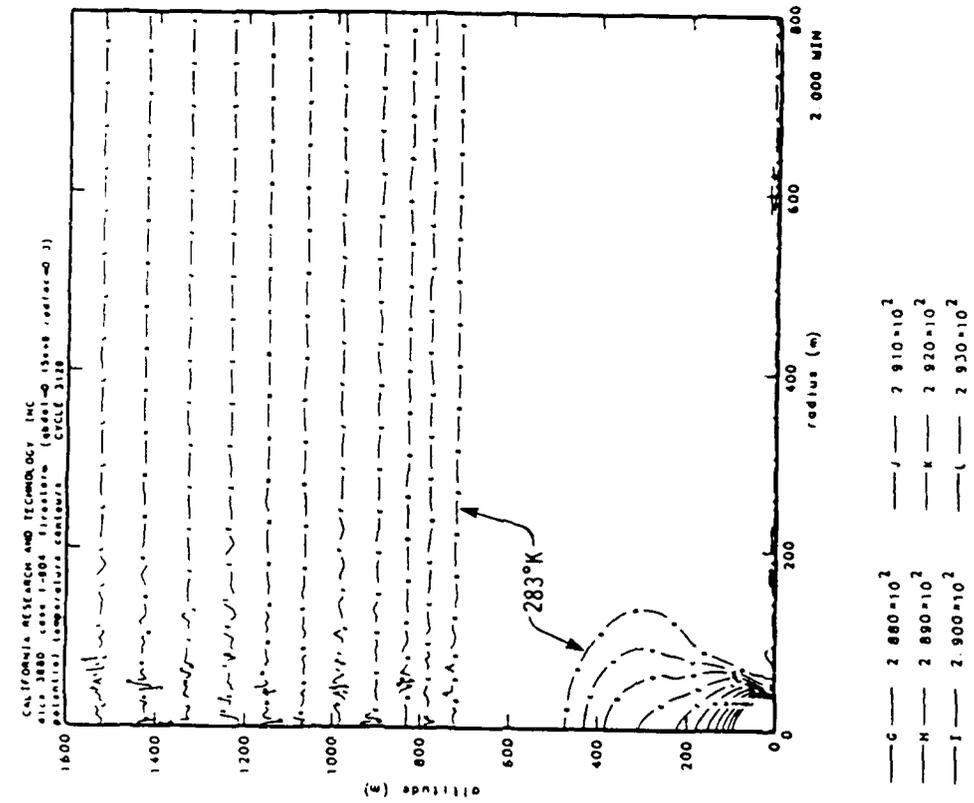
Figure 39a. Model potential temperature field at 1 minute into the Meteotron simulation run. Contour interval is 1°K.
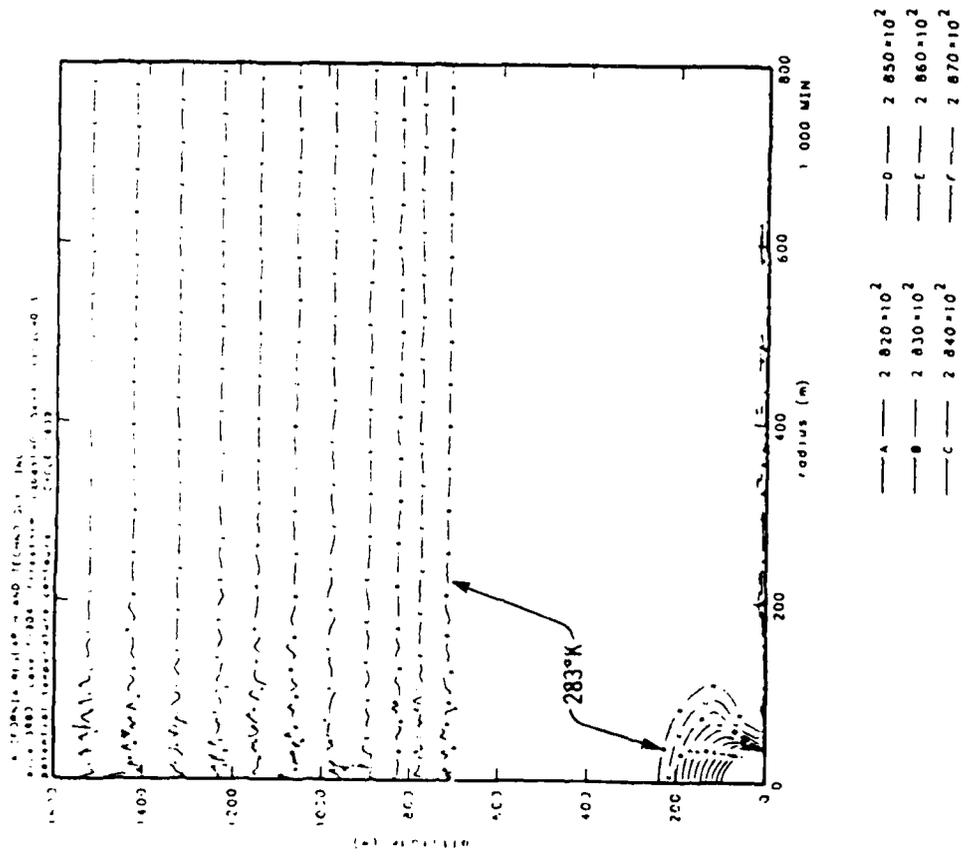
Figure 39b. Model potential temperature field at 2 minutes into the Meteotron simulation run. Contour interval at 1°K.

92
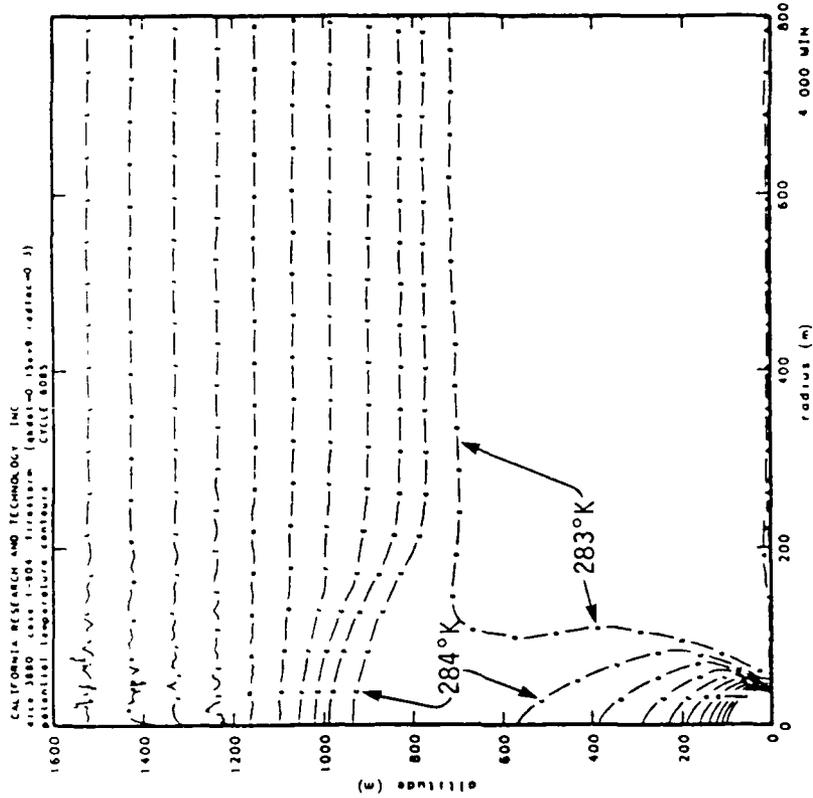
Figure 39c. Model potential temperature field at 3 minutes into the Meteotron simulation run. Contour interval is 1°K.
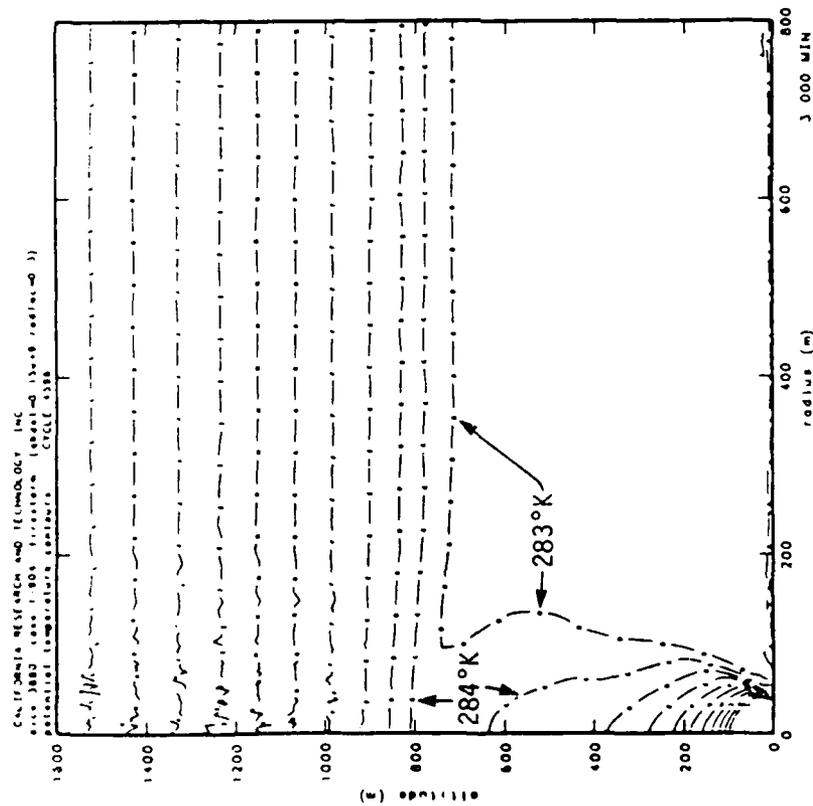
Figure 39d. Model potential temperature field at 4 minutes into the Meteotron simulation run. Contour interval is 1°K.

93

Figure 39f. Model potential temperature field at 6 minutes into the Meteotron simulation run. Contour interval is 1°K.

Figure 39e. Model potential temperature field at 5 minutes into the Meteotron simulation run. Contour interval is 1°K.

this feature cannot be verified directly. During airplane traversals of a plume generated by a 1000 MW burn at the Meteotron facility on July 8, 1978, however, temperatures as much as 2°C below ambient were detected in the updraft region [12], lending plausibility to the under-temperatures predicted by the model.

Since the plume was cooler than the ambient atmosphere above an altitude of 750 m, its penetration into the upper part of the stable layer is due to inertia, rather than to buoyancy. Fig. 40a, for example, shows a plot of the velocity field at 5 minutes, when the plume first attains its maximum altitude. At this time positive vertical velocities extend up to an altitude of 1200 m, and negative vertical velocities are virtually absent. By the time steady state is achieved at seven minutes into the run, however, (see Figure 40b) an extensive area of negative vertical velocity has developed as the overshooting plume falls back towards the level of neutral buoyancy. Although downdrafts near the upper level of the plume were not reported in [6], airplane traversals of several experimental plumes conducted at the Meteotron facility during the summer of 1978 did detect downdrafts of several meters/sec [12], lending plausibility to the results depicted in Fig. 40b.

Fig. 20 shows streamlines of the steady-state mass flux field generated by the run. The flow is directed parallel to the steamlines, with the azimuthally integrated mass-flux between any two neighboring streamlines equal to 10^4 kg/sec; note that below the inversion, horizontal inflow (entrainment) causes the vertical mass flux of the plume to increase with height. Observations of the visible boundary of the experimental smoke plume are plotted in the figure with black circles. While turbulent diffusion within the plume causes the smoke to spread laterally, horizontal inflow at the edges of the plume confines the smoke to the area of upward motion [6]. Fig. 20 shows that good agreement between the edge of the observed smoke plume and the boundary of the simulated inflow area has been obtained,
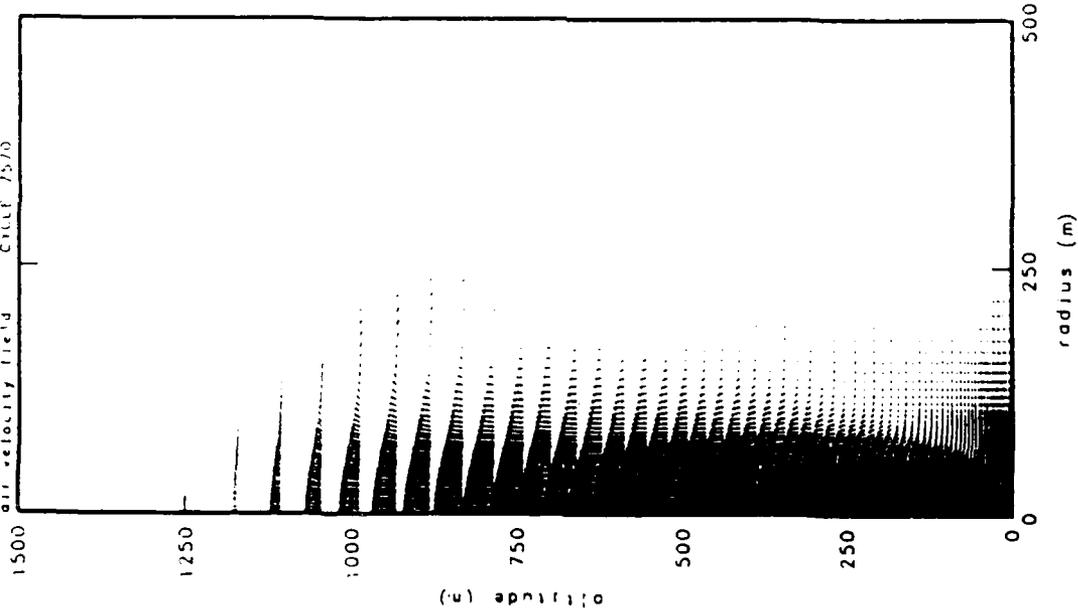
Figure 40a. Velocity vectors
at 5 minutes for
the Meteotron run.
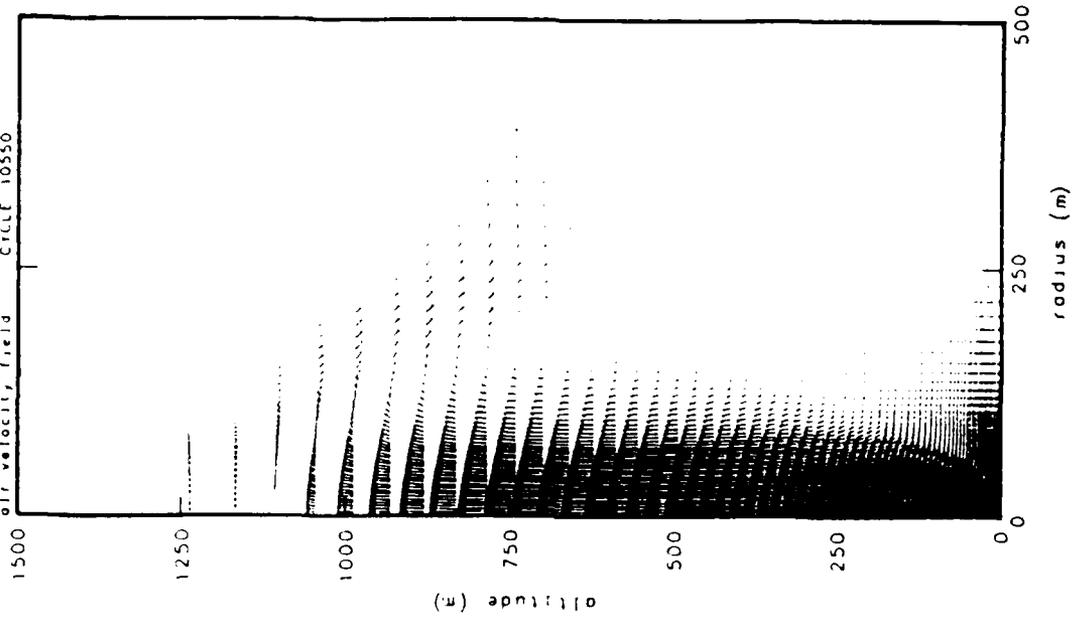
Figure 40b. Velocity vectors
at 7 minutes for
the Meteotron run.

96

indicating that the width of the plume has been correctly predicted by the model.

Temperatures within the plume were measured with a combination of kite radiosonde and Barnes radiometer. The average over-temperature (i.e., excess of plume temperature over the ambient temperature at that level) for eleven Meteotron experiments was plotted by Benech [6] as the solid line in Fig. 21. For comparison, model over-temperatures were computed at a distance from the axis equal to one-half the observed plume radius at the level, and are plotted as black squares in Fig. 21. In view of the uncertainties involved in selecting a single "representative" plume temperature at each level, satisfactory agreement between the observed and computed over-temperature has been obtained.

5.4 DISCUSSION.

From the above comparisons with observed data, it appears that our simulation has succeeded in capturing the essential dynamics of the October 23 Meteotron burn. Since the aspect ratio of the Meteotron plume was considerably larger than the aspect ratios of the firestorm plumes which we simulated (compare Figs. 14 and 40), physical quantities (e.g., mixing lengths) cannot be scaled directly from the test-fire to firestorm cases. In spite of the difference in aspect ratios, however, a consistent line of physical reasoning led to the selection of an asymptotic turbulent length scale which enabled us to accurately calculate the stabilization height of the Meteotron plume (see Fig. 19). Since this event involved the penetration of a thermal plume into an overlying stable layer, the successful simulation of the Meteotron plume encourages us to believe that the DICE code is capable of correctly simulating the penetration of a firestorm plume into the stable layers of the stratosphere.

SECTION 6

THE EFFECTS OF SWIRL

6.1 OVERVIEW.

Anecdotal evidence has suggested that the most intense firestorms created during World War II were accompanied by strong, large-scale rotation, and some investigators have claimed that rotation is an integral part of the firestorm phenomenon, much as it is for hurricanes [7]. While hurricane flow fields extend for hundreds of kilometers and draw on planetary vorticity to generate their rotation, firestorm flow fields extend for only 10's of kilometers, and must rely on ambient vorticity in the local flow field (e.g., a shear in the horizontal wind speed) to generate large rotational velocities. In general, rotational flow (swirl) may affect the dynamics of thermal plumes either by changing the mean fields (e.g., radial pressure gradients), or by changing the level of turbulence (which controls the entrainment of ambient air into the plume).

6.2 EFFECTS OF SWIRL ON THE MEAN FLOW.

In order to investigate the effects of swirl on the dynamics of thermal plumes, the DICE code has been extended to include a tangential velocity component. While the velocity field is now "three-dimensional," axial symmetry has been preserved, and all quantities are still functions of time, radius, and height only. Case 841 was run with the extended version of the code, using the the same parameters and turbulence sub-model as Case 702 (see Table 2). The initial surface swirl velocity distribution for this case was given by

$$w = 2\hat{w} \, \frac{\hat{x}}{1+\hat{x}^3} \, , \qquad (19)$$

where $\hat{x} = x / 10$ km, and $\hat{w}$ was taken to be 10 m/sec. The profile of the initial swirl velocity at the surface is shown in Fig. 22; in the free atmosphere, the initial swirl velocity decreases linearly with height from its surface value to zero near the tropopause.

Figs. 23a-d show vector plots of the non-swirl velocity component and contour plots of the swirl speed for various times in the run. At 15 minutes the inflow layer is not yet fully developed, and maximum swirl velocities have only reached 20 m/sec. At 20 minutes the inflow layer has almost reached the axis, and peak swirl speeds near the axis have increased to 80 m/sec. By 30 minutes into the run air from the region of maximum initial swirl velocity penetrates to the axis, and the "spin-up" of these velocities has generated swirl speeds in excess of 200 m/sec. While the maximum swirl velocities near the surface are located along the axis, a vortex has formed above 10 km, with maximum swirl speeds located about 1 km from the axis.

A time history of the maximum swirl velocity in the grid (see Fig. 41) shows that the "spin up" proceeds quite rapidly, once air from the edges of the fire (where the initial swirl velocity is the largest) reaches the center of the burning region at about 20 minutes into the run. At later times, as air from regions beyond the peak initial swirl angular momentum reaches the axis, the maximum swirl velocity decreases, reaching 160 m/sec by 45 minutes into the run (see Fig. 23d); by this time also the maximum swirl speeds in the vortex above 10 km have collapsed back towards the axis.

Since this run did not include the effects of surface stress, air which is advected towards the origin in the inflow layer will tend to conserve its initial angular momentum about the axis of the fire. A ring of air moving inwards from

99
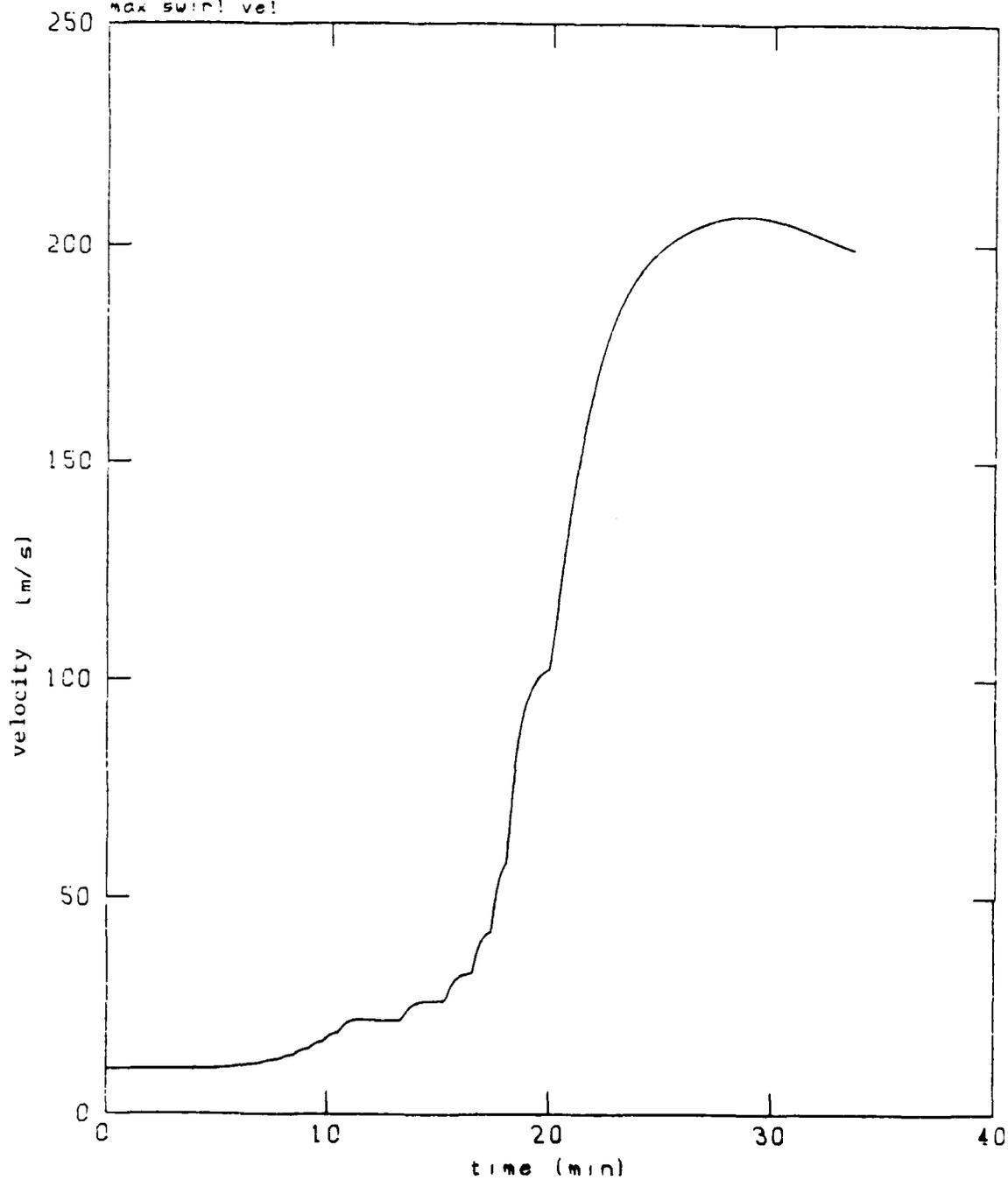
Figure 41.   Time history of the maximum swirl velocity for Case 841.

100

10 km to .33 km (the radial distance of the innermost velocity
grid-point), for example, will experience an increase in swirl
velocity from a value of 10 m/sec to about 300 m/sec if no
stresses are acting on it. Stresses exerted on the air in the
inflow layer by air above it, however, limited the peak swirl
speeds achieved in this run to about 200 m/sec. Of course
smaller peak swirl speeds would be obtained if surface stresses
had been included in the model, or if a smaller initial swirl
velocity had been prescribed. It should be noted that even for a
resting initial atmosphere, the Coriolis effect would be expected
to generate swirl velocities about an order of magnitude less
than those obtained in this run (for mid-latitude sites).

Theoretical considerations lead us to believe that "in a
nonrotating convective cell, the vertical velocity would
overshoot its equilibrium altitude...in contrast, the swirling
updraft will have an adverse pressure gradient...which not only
blocks the overshoot, but almost certainly forces a downdraft
along the axis" ([9], p. 138). For our baseline non-rotating
case (702), the plume shows considerable overshoot by 20 minutes
(see Fig. 14b); for the rotating case (841), a plot of the non-
swirl velocity component at 20 minutes (see Fig. 23b) shows that
the rise of the plume has been substantially blocked, and that an
area of negative vertical velocity has indeed formed along the
axis. Although the swirling plume does penetrate into the
stratosphere at later times (see Figs. 23c-d), the plume heights
remain about 3 km lower than the corresponding heights for Case
702 (compare with Figs. 14c-d). Due to the reduced overshoot,
the tracer cloud for case 841 (see Fig. 42) does not show the
secondary region of lofted soot which was obtained in case 702 at
higher altitudes near the axis (see Fig. 15).

The results of Case 841 show that large rotational
velocities may develop in the interior of a 10-km radius fire,
given an initial ambient swirl of 10 m/sec at the fire edge, and
that the effect of the swirl is to delay plume rise and lower the

101
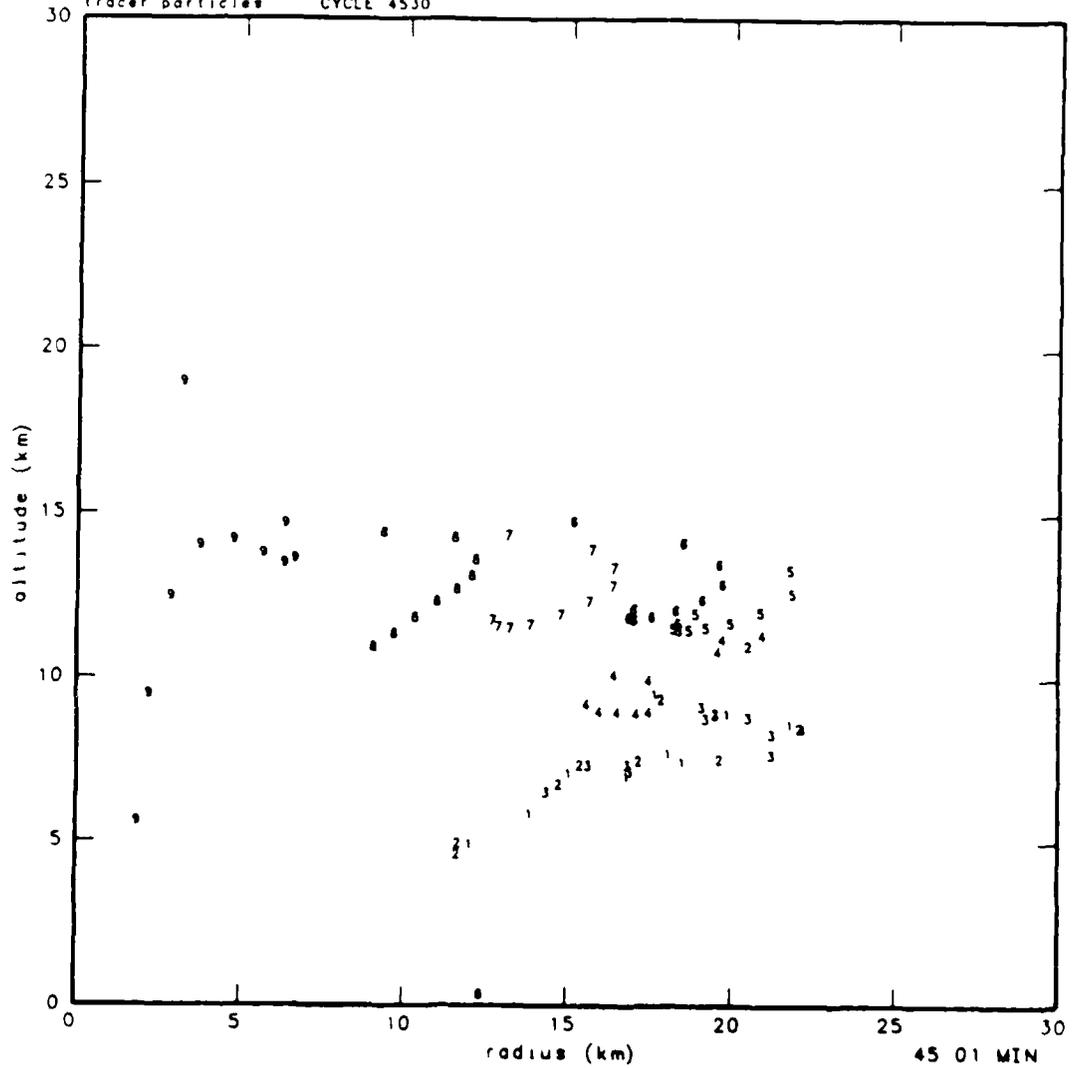
Figure 42. Tracer particles at 45 minutes for Case 841. (Note that the initially released group is labeled Group 1).

stabilization height somewhat. Interaction between the swirl velocity field and the turbulence was not considered in this case, however, and it is possible that the swirl may act to suppress turbulence, much as a stable density stratification does. As was shown by the comparison b tween Cases 702 and 705 in Section 4, this would tend to intensify the plume.

6.3 EFFECTS OF SWIRL ON TURBULENCE.

A given distribution of swirl velocity may act as a source or sink of turbulent kinetic energy (TKE). When only swirl velocity is present, a local balance between production and dissipation terms, similar to that used in the turbulence sub-model described in Section 4, may be solved to give a diagnostic relation for the TKE in terms of the mean swirl velocity distribution [10]. This relation turns out to have a form similar to that which would be given by a simple mixing length argument; the resulting turbulent stresses, however, also depend on the curvature Richardson number

$$R_c = \frac{2w}{\frac{\partial}{\partial r}\left(wr\right)} \tag{20}$$

through the stability function

$$S_c = \left[1-K \frac{R_c}{(1-R_c)^2}\right]^{3/2}. \tag{21}$$

Here w is the swirl velocity, r the radial distance, and K a fixed constant.

A plot of the stability function $S_c(R_c)$, taken from [10], is shown in Fig. 24. For values of Sc greater than 1, the curvature effect amplifies the turbulence, while for values of S_c less than 1, the curvature has a damping effect. For values of R_c between

103

0.185 and 5.416, S_c becomes negative; in this case destruction of TKE by the mean swirl velocity field exceeds production, and no turbulence exists.

When the generation of TKE by non-swirl winds and buoyancy is taken into account, the destruction of TKE by the swirl velocity field may still exert a damping effect on the turbulence or extinguish it completely, depending on the relative magnitudes of the source and sink terms in the TKE budget equation. Unfortunately this equation is too complicated in the general case to be solved diagnostically for the TKE, as was done for the case with only non-swirl terms (Section 4), or for the case with only swirl terms [10]. To adequately treat the case where swirl and non-swirl terms are active simultaneously, it becomes necessary to include separate predictive equations in the model for all components of the turbulent stress tensor, as well as for the turbulent heat fluxes.

While no such scheme has yet been implemented in the DICE code, a model developed by the Aeronautical Research Associates of Princeton, Inc. (ARAP) currently has this capability. In a recent study of tornado dynamics [9], two versions of the ARAP code were used; one which had a simplified turbulence model similar to that used in DICE Cases 702 and 705 (which does not include the effects of curvature on turbulence), and one which used the fully predictive model described above (which implicitly includes the effects of curvature on turbulence). Non-dimensional plots of the turbulent eddy viscosity field produced by the runs with the simplified and full turbulence models are shown in Figs. 25a and 25b, respectively. Near the surface the turbulence profiles are similar, but at higher altitudes the full turbulence model produces much less eddy viscosity, indicating that rotational flow can have a damping effect on turbulence above the boundary layer.

104

Since the ARAP study dealt with swirling plumes, the results are of interest to the rotating firestorm case, although the tornado problem includes no buoyant generation of TKE in the boundary layer. Some preliminary calculations done at CRT, in fact, indicate that buoyant production of TKE in the boundary layer of a firestorm would proceed at a considerably higher rate than its destruction by a plausible swirl velocity distribution. Together with the result obtained in the ARAP study, this suggests that the suppression of turbulence by swirling flow in the boundary layer of a firestorm would probably be small.

In comparing Cases 702 (ℓ_∞ = 100 m) and 705 (ℓ_∞ = 25 m) in Section 4, we saw that reducing the turbulence by decreasing the mixing length from 100 m to 25 m throughout the computational domain resulted in a large increase in the plume stabilization height. While it appears unlikely that swirl would decrease the turbulence in the boundary layer, the ARAP results suggest that swirl could significantly reduce the level of turbulence in the region above the boundary layer. In order to estimate the likely effects of swirl on the plume, then, we ran Case 846 with the same parameters as Case 702 (see Table 2), keeping the mixing length fixed at 100 m between the surface and 0.5 km altitude, but letting it decrease linearly to 25 m at 1 km altitude (see Fig. 26).

Figs. 27a-b show the resulting velocity fields at 20 and 30 minutes. Comparing with the corresponding plots for Case 702 (see Figs. 14b-c), we see that cutting back the mixing length from 100 m to 25 m above the boundary layer causes an enhancement in the plume's height of about 3 km. A much larger enhancement, however, is gained by reducing the mixing length to 25 m throughout the computational domain, as was shown by the comparison between Cases 702 and 705. This result is not unexpected, in view of the conclusion reached in Section 4 that entrainment within the boundary layer determines the core

105

temperature, and ultimately the stabilization height, of the plumes from large-area fires.

6.4 DISCUSSION.

Case 841, described in Section 6-2, showed that high swirl velocities can develop near the core of a large-area fire, given a moderate initial ambient swirl velocity field. We saw that the large swirl velocities which developed were due to the approximate conservation of angular momentum in the inflow layer, which can be expected to hold as long as the flow field maintains axial symmetry. By comparing with a similar non-swirl case, we also saw that the effects of swirl on the mean flow dynamics were to delay plume rise somewhat, and to lower the plume height by about 3 km.

The question of how swirl will affect the turbulence in a large-area fire is much more difficult, and at present we can only make reasonable estimates of this effect. By assuming that swirl decreases the turbulence in the region above the boundary layer, we obtained a moderate enhancement in the plume height. Suppression of turbulence in the inflow layer cannot be ruled out, however, particularly in view of the large rotational velocities which develop near the axis. The definitive resolution of this question awaits the extension of the DICE code to predict the full set of turbulent fluxes, or the application of a model which already has that capability, such as the ARAP code, to the firestorm problem.

LIST OF REFERENCES

1. SIPRI (Stockholm International Peace Research Institute), Incendiary Weapons, MIT, Cambridge, MA 1975.

2. S. Glasstone and P. J. Dolan (Eds.), The Effects of Nuclear Weapons, U.S. Department of Defense and U.S. Department of Energy, 1977.

3. Rosenblatt, M. and Eggum, G.E., DICE - A Two-Dimensional Implicit Code for Treating Compressible Flow in a Fluid-Particle Mixture, DNA2976F, March 1973.

4. Blackadar, A.K., "The Vertical Distribution of Wind and Turbulent Exchange in a Neutral Atmosphere," J. Geophys. Res. 67:3095-3102, 1962.

5. Yamada, T., and Mellor, G.L., "A Simulation of the Wangara Atmospheric Boundary Layer Data," J. Atmos. Sci. 32:2309-2329, 1975.

6. Benech, B., "Experimental Study of an Artificial Convective Plume Initiated from the Ground," Journal of Applied Meteorology 15:127-137, 1976.

7. Carrier, G., Fendell, F.E., and Feldman, P.S., "Firestorms," J. Heat Transf. 107:19-27, 1985.

8. Weihs, D., and Small, R.D., Swirl Induced by Large Area Fires, DNA001-85-C-0089, 1985.

9. Lewellan, W.S., and Sheng, Y.P., "Modeling Tornado Dynamics," Final Report, Aeronautical Research Associates of Princeton, Inc., January 12, 1976 - May 31, 1980, NUREG/CR-1585.

10. Mellor, G.L., "A Comparative Study of Curved Flow and Density-Stratified Flow," J. Atmos. Sci. 32:1278-1282, 1975.

11. Federal Emergency Management Agency, FEMA Attack Environment Manual, Chapter 3, What the Planner Needs to Know About Fire Ignition and Spread (amended title), CPG 2-1A3, 1982.

12. Benech, B., Dessens, J., Charpentier, C., Sauvageot, H., Druilhet, A., Ribon, M., Dinh, P.V., and Mery, P., "Thermodynamic and Microphysical Impact of a 1000 MW Heat-Released Source into the Atmospheric Environment," Third WMO Scientific Conference On Weather Modification 1:111-118, Geneva, Switzerland, 1980.

108

DISTRIBUTION LIST

DEPARTMENT OF DEFENSE

DEFENSE INTELLIGENCE AGENCY
    ATTN: DB-6E2 C WIEHLE
    ATTN: RTS-2B
    ATTN: WDB-4CR

DEFENSE NUCLEAR AGENCY
    ATTN: OPNS
    ATTN: RAAE
2 CYS ATTN: TDTR
4 CYS ATTN: TITL

DEFENSE TECHNICAL INFORMATION CENTER
12 CYS ATTN: DD

FIELD COMMAND DEFENSE NUCLEAR AGENCY
    ATTN: FCTXE
    ATTN: FTTD W SUMMA

JOINT STRAT TGT PLANNING STAFF
    ATTN: JKCS

DEPARTMENT OF ENERGY

LAWRENCE LIVERMORE NATIONAL LAB
    ATTN: L-442, J BACKOVSKY
    ATTN: N ALVAREZ
    ATTN: R PERRETT

LOS ALAMOS NATIONAL LABORATORY
    ATTN: DR. D CAGLIOSTRO

OTHER GOVERNMENT

DEPARTMENT OF COMMERCE
    ATTN: H BAUM
    ATTN: R LEVINE

DIRECTOR, FFASR
    ATTN: C CHANDLER

FEDERAL EMERGENCY MANAGEMENT AGENCY
    ATTN: H TOVEY
    ATTN: OFC OF RSCH/NP H TOVEY

DEPARTMENT OF DEFENSE CONTRACTORS

CALIFORNIA RESEARCH & TECHNOLOGY, INC
2 CYS ATTN: M ROSENBLATT
2 CYS ATTN: S K KRUEGER
2 CYS ATTN: S L MARCUS

CARPENTER RESEARCH CORP
    ATTN: H J CARPENTER

CHARLES SCAWTHORN
    ATTN: C SCAWTHORN

FACTORY MUTUAL RESEARCH CORP
    ATTN: R FRIEDMAN

IIT RESEARCH INSTITUTE
    ATTN: H NAPADENSKY

INSTITUTE FOR DEFENSE ANALYSES
    ATTN: L SCHMIDT

KAMAN SCIENCES CORP
    ATTN: E CONRAD

KAMAN TEMPO
    ATTN: DASIAC

KAMAN TEMPO
    ATTN: DASIAC

MISSION RESEARCH CORP
    ATTN: J BALL

MODELING SYSTEM, INC
    ATTN: G BERLIN

NOTRE DAME DU LAC, UNIV OF
    ATTN: T J MASON

PACIFIC-SIERRA RESEARCH CORP
    ATTN: H BRODE, CHAIRMAN SAGE
    ATTN: R SMALL

R & D ASSOCIATES
    ATTN: D HOLLIDAY
    ATTN: F GILMORE
    ATTN: R TURCO

RAND CORP
    ATTN: P DAVIS

RAND CORP
    ATTN: B BENNETT

SCIENCE APPLICATIONS INTL CORP
    ATTN: M DRAKE
    ATTN: M MCKAY

SCIENCE APPLICATIONS INTL CORP
    ATTN: J COCKAYNE

SCIENTIFIC SERVICES, INC
    ATTN: C WILTON

SRI INTERNATIONAL
    ATTN: G ABRAHAMSON

STAN MARTIN ASSOCIATES
       ATTN: S MARTIN

SWETL, INC
       ATTN: T PALMER

TRW INC
       ATTN: F FENDELL

END

DATE

FILMD

3-88

DTIC